REPORT DOCUMENTATION PAGE

AFRL-SR-BL-TR-98-

Public reporting burden for this collection of information is estimated to average 1 hour per response, includ
sources, gathering and maintaining the data needed, and completing and reviewing this collection of informa
aspect of this collection of information, including suggestions for reducing this burden to Washington Headqu
Reports, 1215 Jefferson Davis Highway, Suite 1204, Arlington, VA 22202-4302, and to the Office of Manage
Washington, DC 20503

1. AGENCY USE ONLY (Leave blank)	2. REPORT DATE 4 Jan 1998	3. REPORT TYPE AND DATES COVERED Final 1 Oct 1995 -- 30 Sept 1997

4. TITLE AND SUBTITLE
Investigation of Lg Attenuation and Blockage in Models of the Eurasian Crust

5. FUNDING NUMBERS
PR 2309
G F49620-94-1-0059
TA AS

6. AUTHOR(S)
Vernon F. Cormier
Thomas S. Anderson

7. PERFORMING ORGANIZATION NAME(S) AND ADDRESS(ES)

University of Connecticut
Geology and Geophysics
354 Mansfield Rd, Room 207
Storrs, CT 06269-2045

8. PERFORMING ORGANIZATION REPORT NUMBER

9. SPONSORING / MONITORING AGENCY NAME(S) AND ADDRESS(ES)

AFOSR/NM
110 Duncan Ave., Suite B115
Bolling AFB, DC 20332-8050

10. SPONSORING / MONITORING AGENCY REPORT NUMBER

11. SUPPLEMENTARY NOTES
To be submitted as two papers for publication in the Bulletin of the Seismological Society of America

12a. DISTRIBUTION / AVAILABILITY STATEMENT
Unlimited

DISTRIBUTION STATEMENT A

Approved for public release;
Distribution Unlimited

12b. DISTRIBUTION CODE

13. ABSTRACT *(Maximum 200 Words)*
The efficiency of Lg propagation is predicted using known three-dimensional variations in large scale crustal structure with Lg modeled as a sum of SmS rays. The complexity of Lg coda is predicted assuming single scattering. Amplitude variations observed at Eurasian arrays agree with the predictions for the effects of known variations in crustal thickness and basin thickness. For shallow sources, scattering by heterogeneity close to the source and receiver control Lg complexity. Experiments with anisotropic distributions of heterogeneity are effective in simulating the coda of regional phases in regions characterized by a dominant trend of deformation.

19980218 038

14. SUBJECT TERMS CTBT, seismic propagation, Lg, scattering	15. NUMBER OF PAGES 113
	16. PRICE CODE

17. SECURITY CLASSIFICATION OF REPORT Uncl.	18. SECURITY CLASSIFICATION OF THIS PAGE Uncl.	19. SECURITY CLASSIFICATION OF ABSTRACT Uncl.	20. LIMITATION OF ABSTRACT UL

NSN 7540-01-280-5500

Standard Form 298 (Rev. 2-89)
Prescribed by ANSI Std 739-18

DTIC QUALITY INSPECTED 3

INVESTIGATION OF LG ATTENUATION AND BLOCKAGE IN MODELS OF THE EURASIAN CRUST

Vernon F. Cormier
Thomas S. Anderson

Department of Geology and Geophysics
University of Connecticut
Storrs, CT 06269-2045

January 4, 1998

Report No. 4
Final
October 1, 1995-September 30, 1997

Table of Contents

Summary

Effects of large and small scale structure on the propagation of Lg and regional seismic phases are investigated in the vicinity of Eurasian seismic arrays KNET, CNET, and ILPA. The effects of small scale structure are predicted using models of Moho and basement topography with Lg modeled as a series of multiple SmS waves, critically reflected by the Moho. Predictions of large variations in Lg amplitude associated with the variations in crustal thickness surrounding the Hindu Kush and Pamir mountains agree with observations at KNET. At CNET and ILPA, thick basins are shown to have large effects on shallow crustal sources, blocking either a portion or all of the Lg coda for paths crossing these basins. The effects of small scale structure on the propagation of regional seismic phases are investigated using a Born approximation with locked mode summation, with scatterers treated as equivalent sources, reradiating the incident wavefield. For shallow sources, it is shown that scattering by heterogeneity close to the source and receiver control Lg complexity, equalizing high frequency energy on all components of motion regardless of source type. Experiments with data from the Pinion Flats array suggest that anisotropic distributions of heterogeneity are effective in simulating the coda of regional phases in regions characterized by a dominant trend of deformation.

1 Introduction

Whether represented by critically reflected rays at the Moho (Gutenberg, 1955; Bostock and Kennett, 1990) or by locked modes (Oliver and Ewing, 1957; Knopoff, Scwab and Kausel, 1973; Kennett, 1983; Snieder, 1986; Wang and Hermann, 1988; Mitchell, 1995), the energy in the Lg phase is the usually the most energetic regional seismic phase trapped in the crustal waveguide, and hence the most useful for nuclear monitoring. The modal representation, while useful in 1-D models, becomes impractical when applied to 2-D and 3-D models due to the computational expense of calculating mode coupling coefficients. More recently, the ray approach and finite difference methods are used in the study of Lg wave propagation. The computational expense of a numerical solution to the wave equation for much more than 100 wavelengths of propagation, however, has limited finite difference modeling to primarily 2-D structure and low frequency bands.

Ray based techniques of forward modeling are sufficiently fast to allow predictions of efficiency of the propagation of Lg and are well suited for examining the attenuation due to the scattering and blockage of Lg in the perturbed 3-D crustal wave guide. Accurate application of the ray method is limited by the ratio λ/s, where λ is the wavelength and s is the scale length of the medium. Errors in the prediction of body wave amplitudes by ray theory are typically bounded by several percent when the non-dimensional ratio λ/s is less than several 0.1's. The smallest scale length s of a medium is either the minimum of the radius of curvature of a discontinuity or the minimum of the quotient of velocity (or density) divided by the magnitude of the velocity gradient (or density gradient). Fortunately, the scale lengths of structure known from seismic profiling and regional surveys of topography, gravity and magnetic fields are such that the ratio λ/s is sufficiently small in at least a portion of the frequency band important to regional monitoring to permit the accurate use of ray theory if one assumes that the smaller, unresolved, scale lengths of

1

structure do not strongly affect the propagation. This point of view is taken in the first section of work summarized in this report titled **Effects of Large Scale Heterogeneity**, where ray theory is used to qualitatively predict paths of Lg blockage by large scale (small values of λ/s) variations in crustal and sedimentary basin thickness. Examples of qualitative predictions of Lg propagation efficiency are compared with data observed at the KNET, CNET, and ILPA arrays.

As the ratio λ/s becomes much larger than 1, paradoxically, ray theory may again be used accurately if scattering by small scale heterogeneities is approximated by the Rayleigh-Born approximation. If the velocity and density perturbations are not too high, a heterogeneous medium may be parameterized by a sum of point scatterers and the effects from each scatterer summed. Since the ray representation of Lg is already given as a sum of rays, the requirement of an additional sum over ray paths to and from scatterers becomes difficult in both computation and bookkeeping. A similar type of problem exists in the conventional application of the mode representation of Lg with the Born approximation, where, in theory, every mode may scatter into every other mode. Although many of these mode interactions can be shown to be insignificant in energy, the approach of calculating mode-coupling coefficients, while useful in understanding the processes of scattering, results in an inefficient algorithm for waveform synthesis at high frequency. In the second section of this report titled **Effects of Small Scale Heterogeneity**, an alternative algorithm for the mode-Born approximation is applied to small scale heterogeneity, which allows it to be efficiently applied in a much higher frequency band. In this algorithm, mode coupling coefficients are not computed. The complete wavefield is calculated at each point scatterer and reradiated by the equivalent source representation of the scatterer. To understand the distribution of scatterers responsible for equalizing Lg energy on three-components of motion, computational experiments are made with various depth and lateral distributions of scatterers in three-dimensions.

2 Effects of Large Scale Structure

2.1 Forward modeling method

The travel times and amplitudes of multiple SmS rays that comprise Lg coda are computed by integrating kinematic and dynamic ray tracing equations (Cerveny and Hron, 1980; Cerveny, 1985). The Moho and the boundary between a sedimentary layer and hard-rock layer (basin topography) are modeled as Epstein transition zones (hyperbolic tangents). With the Moho and basin boundaries so modeled, all SmS rays become turning rays in the steep gradient region of the Moho transition zone, eliminating the need for computing many reflection coefficients and complex descriptions of rays interacting with three discontinuities (surface, basin/sediment interface, and Moho). The effects of lateral variations in crustal thickness and basin thickness on Lg efficiency are predicted by plotting SmS ray turning and bounce points or cross sections of the crustal waveguide showing ray paths. Ray bounce points may be connected for rays shot at constant vertical and varying azimuthal take-off angles to reveal how the Lg wavefront propagates at distances greater than 500 km. Not connecting the points enables closer range structure effects to be observed. The existence of databases of Moho and basin topography sampled on grids of 10 km or smaller spacing, allows this approach to applied to predict Lg propagation efficiency observed at several arrays in Eurasia. Results are reported for sources within 1000 km of the KNET, CNET and ILPA arrays (figure 1). A brief geological background of these regions provides a context in which to study the regional wave propagation.

2.2 Tectonic settings

2.2.1 Garm (KNET)

The Garm region (figure 2), in which KNET is located, is one of the most seismically active intra-continental regions in the world and is characterized by intense surface deformation. Earthquake focal mechanism studies indicate that the Garm region is dominated by nearly horizontal compression. The direction of principal compression varies from approximately north-west in the western region to nearly north-south in the North-East region (Lukk and Shevchenko, 1986, 1990; Ramos, 1992). Most of the seismicity is associated with the active deformation of the sedimentary rocks in the Peter the First Range. The seismicity may be associated with several fault zones, the most prominent is a near vertical feature beneath the axial part of the range (Ramos, 1992). Hypocenters within the Peter the First Range suggest a southeast dipping zone of seismicity that can be traced updip to the Petrovsky thrust fault. Under this upper crustal seismicity at a depth of 12 to 17 km is an aseismic zone that may be related to low strength evaporites at the base of the sedimentary section. The aseismic zone is then underlain by an anomalously deep crustal seismicity at a depth of 17 to 30 km. This deeper seismicity is thought to be associated with a southeast dipping zone about 10 km in thickness, of intracontinental subduction whose surface expression is the Vakhsh thrust fault, at the frontal edge of the Peter the First Range.

Crustal structure in the Pamir-Tien Shan region has been determined by inverting for a 1-D layered velocity model using data from two networks located near the Soviet earthquake prediction laboratory at Garm, Tadjikistan (Hamburger et al., 1993). The P velocities of two upper crustal layers are indistinguishable from a model with a single layer over a half

space. Hambureger et al.'s models are comprised of a 8 km thick upper crustal layer of 5.2 km/s over a 5.9 km/s half space, and a 5.2 km/s layer over a 6.3 km/s halfspace. These results contradict previous velocity models that had anomalously low velocity zones in the mid-crust.

2.2.2 Tibet Plateau

Figure 3 summarizes the broader tectonic setting of KNET. Lg has been observed across most of Asia, but Lg has not been observed for paths crossing through the Tibetan Plateau (Ruzaikin et al., 1977). This has been attributed to several factors, the change in crustal thickness and/or structural discontinuities at the boundaries of the plateau or to an unusual velocity structure (absence of a granitic layer) and to intrinsic attenuation within the plateau (Ruzaikin et al., 1977; Aki, 1980; Gregerson, 1984; Frankel et al., 1990; Mitchell, 1995). Crustal thickness in the Tibetan Plateau is greater than the surrounding tectonic regions of the Indian Shield to the south and the Tarim Basin to the north (Molnar, 1988). This significantly deforms the crustal waveguide. Complicated structures of the Himalayan boundary thrust and the northern Kunlun fault may also cause significant scattering of Lg energy.

The Tibetan Plateau is bounded by the Kunlun Mountains in the north and the Himalayas to the south. It has an average elevation of 5 km and an areal extent of nearly 700,000 square kilometers. The uplift of the plateau is the result of the collision of the Indian plate with Eurasia that began in the Middle Eocene approximately 45 my (Molnar and Tapponier, 1975). Relative motion of the plates continues at a rate of 5 cm/yr. The Tibetan Plateau is highly fractured due to the suture zones bounding the many terranes that make up the plateau and the abundant normal and strike-slip faults in the uppermost 20 km along which the crust is actively deforming (Randall et al., 1995). Most earthquakes that occur within

the plateau are located in the top 5-10 km of the crust (Molnar and Chen, 1983; Zhao and Helmberger, 1991). Geophysical observations of shallow seismicity are consistent with anomalously high heat production beneath the northern portion of the plateau. The earthquake cutoff temperature is estimated to be between 250 and 450 C (Chen and Molnar, 1983). Volcanic flows of both granitic and basaltic composition are observed at the surface throughout the northern section of the plateau (Dewey et al., 1988). This indicates a mantle source of volcanism causing crustal heating as it propagates to the surface. Crustal heating is likely to significantly increase attenuation (decrease Q) (Frankel et al., 1990). High crustal temperatures are not clearly understood and may be due to the concentration of radiogenic crustal material resulting from the crustal shortening during the plateau formation (Zhao and Helmberger, 1991) or due to a high heat flux from the upper mantle (Molnar, 1988).

2.2.3 Caucasus and Iran (CNET and ILPA)

The Caucasus region, in which CNET (figures 4a-c) is located, is a mixture of tectonic units created by the collision of the Arabian and Eurasian plates that initiated approximately 25 million years ago. The interaction of these large plates determines the meridional direction of maximum compression stresses in the Caucasus and kinematics of movements in the system of large and small faults, e.g., North Anatolian, East Anatolian, Zagros, Pambak-Sevan, etc. The Caucasus orogeny is similar to, but younger than the Himalayan orogeny, with the orientation of the colliding Arabian plate the same as the north-east verging Indian plate). The Lesser Caucasus (41.5 latitude) consists of a north-verging system of folds that have their origin in the continental collision. The Greater Caucasus (42.5 latitude) was formed from south-verging system of folds, related to the northward thrust of the Arabian plate. These different tectonic units are separated by the Transcaucasian Massif (Adamia et al., 1991). The active tectonic setting is a compressive

6

one with evident slip fronts and folded structures. Folds are locally interrupted by continuous structural lineations that suggest a strike-slip movement. The most significant lineament is parallel to the orogenic belt.

The Greater Caucasus has three large morphostructural units: the Kura basin, the Greater Caucasus, and the foothills. The deformations of the Greater Caucasus involve the whole crust and, most likely, the upper mantle, all the way to the Lesser Caucasus. The general trend of large morphostructures from west to north-west is oblique to the direction of the prevailing compression. The Greater Caucasus region is highly faulted and deformed due to mountain building. The meridional faults faults of the Trans-Caucasian extension are extensional faults, the near-latitudinal Caucasian faults are compression upthrow shear thrust faults and upthrow shifts, and the diagonal faults extended north-west are shear structures, i.e., strike-slip displacements (Rogozhin et al., 1993).

The Lg phase propagates well throughout most of the region except for events coming from the northern Black Sea and the Caspian Sea regions and events in the Hormuz region of Iran (at the eastern end of the Persian Gulf opposite Oman) (Sweeney, 1996). The Black Sea-Caspian Sea Lg blockage is speculated to be related to a change in crustal thickness beneath the Black Sea and the Caspian Sea or to basin effects, or a combination of both. Sediments are as thick as 20 km beneath the Caspian sea. Blockage of Lg from the Hormuz region is not understood, as Lg is not blocked from other similar parts of the Zagros range to the northwest. The Kazerun line is a N-S trending line consisting of the Borazjan, Kazerun, and High Zagros faults and divides the Zagros range (a fold-thrust belt lying to the southwest of the Main Zagros Reverse Fault) into two different regions. In the southeast there is a thick (1 km) late Precambrian evaporite unit that has been mobilized into extensive salt diapirs and nappes; to the northwest, the salt unit is much less prominent and

mobilized salt is much rarer. The mobile salt is thought to be a possible cause of scattering of Lg in this region. In the extreme southeastern corner of Iran there is oceanic subduction and local magma formation, with an inboard volcanic arc delineated by a string of Quaternary volcanic centers. Quaternary volcanism is also associated with the central Iranian plateau southwest of the city of Meshad.

2.3 Instrumentation and data

2.3.1 KNET

The Kyrgyz Seismic Network consists of 10 stations and is located near the capital of Kygyzstan, Bishkek (figure 5). Tectonically, it is located approximately 150 km north of the Garm region and the western flank of the Himalayan plateau. Each station is comprised of three component Streckeisen STS-2 seismometers with Reftek RT72A-02 dataloggers with 100 sps and 20 sps datastreams for three high gain and three low gain channels. The KNET stations are all located in hard rock, but stations CHM, TKM, KBK, and EKS2 have shallow sediments located within 100 meters of their vaults.

2.3.2 CNET

In August 1990, a Lamont-IRIS team deployed a seismic network in the Caucasus. The original intent was to span the seismically active Caucasus, but the array size was reduced due to political turmoil in the region. The scope was limited to a small aperture array in the region near Kislovodsk, on the northern slopes of the Greater Caucasus and on the southern Russian Platform (figure 4).

2.3.3 ILPA

The set of continuous waveform data from the Iranian Long-Period Array, (ILPA , figure 6) used in this study was compiled by Jerry Sweeney (1996). The ILPA array was operational during the late 70's. The "Long Period" array contained both short period and long period instruments. The array sensor sites, remotely located with respect to the recording station, are approximately 60 kilometers southwest of Tehran, Iran. Stations 2 through 7 are arranged in a hexagon configuration with Station 1 located in the center of the array. The sites are all located in rocky areas where very little overburden exists, and on high points with respect to the surrounding area.

2.4 Results of ray experiments

2.4.1 KNET

Predictions of Lg propagation efficiency computed by ray theory are compared with the waveforms of specific events chosen to illustrate the effects of varying Moho topography. Of particular interest are the effects of Moho topography on Lg paths that cross extreme lateral gradients in crustal thickness associated with the Pamir Range and the Himalayan Plateau as well as Lg paths that cross the relatively flat Tien Shan region to the east of KNET.

A one dimensional velocity model (JSPC, 1993) for the region is used along with the database of Moho topography by Fielding et al. (1992) to provide a three dimensional model for the dynamic ray tracing. The variations in Lg coda from regional seismograms recorded by the KNET array in the Republic of Kyrgyzstan are compared with predicted variations in the paths of multiple SmS waves comprising the Lg phase. Ray trajectories,

SmS turning points and surface bounce points (Bostock and Kennett, 1990), plotted in map view, are used in the interpretation and prediction of structural effects on Lg.

Events were selected based on the following criteria: shallow depth, a good signal to noise ratio, range from stations between 300 and 1200 km, and source-receiver paths that cut through regions where the Moho depth varies greatly. The data are processed using the Seismic Analysis Code (Lawrence Livermore National Laboratory, 1990). The data are band passed (0.5-5 Hz) using a Butterworth filter with four poles and then plotted in a record section for each event. Approximately 40 events met the selection criteria. Out of that data, three events were chosen (figure 7a,b) that represented sources from each of the three tectonic regions near KNET. Event 1 is located in the Pamir region, Event 2 is in the Himalayan Plateau, and event 3 is located in the Tien Shan region to the east.

Event 1. 6 May 92. This event was chosen for the ray paths that pass through a region north of the Pamir Mountains where the depth of the Moho increases to 70 km and is characterized by steep gradients. The array stations had a back azimuth range of 198.02 to 209.86 degrees and ranged in distance from 527.9 to 611.3 km. The effects of the steep Moho gradient are seen in the Lg amplitude and duration, which differ greatly across the array (figure 8). Stations TKM (baz 209.86; dist. 527 km) and CHM (baz 204.86; dist 592 km) have very little Lg, while station AAK (baz 204.47; dist 546 km) has noticeable Lg and EKS2 (baz 198.02; dist 527 km) has significant Lg. Ray tracing predicts strong variations for rays passing this region. The map view of SmS ray bounce points (figure 9) for this source receiver pair shows that the wave front is distorted by the second bounce and a two dimensional caustic develops that transects the array. This correlates well with the differences seen in Lg from one side of the array to the other. Two-dimensional vertical cross sections of ray paths projected onto vertical planes through back azimuths for this

event (figure 10) show significant effects of the rapid lateral variation in crustal thickness The ray trajectories, which differ only slightly in azimuth, differ dramatically in focusing and defocusing at distances as close as 150 km. The rays diverge after the first bounce and the range of coherency of the Lg wavefront is much less than 150 km.

Event 2. 27 June 92. Stations in the array had a back azimuthal range of 139.17 to 146.57 degrees and ranged in distance from 987 to 1047 km. The epicenter for this event is in the thickened crust (70 km) associated with the Hindu Kush region. The record section (figure 11) shows strong variations across the array in Lg coda shape, duration and amplitude ratio to Pg, which is expected for paths that cross regions of strong Moho topography. The Lg coda at station EKS2 has a different shape and a lower Lg/Pg ratio than the rest of the array. The ray tracing for this event shows most of the array lying in a region of defocusing (figure 12), while the western most station (EKS2) lies on a two dimensional caustic or region of apparent focusing. This may account for the fuller Lg coda seen at station EKS2. The cross section of ray paths through the crust for this event (figure 13) illustrates the effects of focusing and defocusing of rays along this path.

Event 3. 25 Mar 92. This event traverses a region of Moho east of the array that is relatively flat and is approximately 47 km deep. The record sections (figure 14a) show similarities in both Lg coda length, shape and amplitude ratio to Pg. The similarities in Lg coda are consistent with the expected effect of the flat Moho between the source and the array. Ray tracing shows that the rays passing through this region are not greatly affected by the slight changes in Moho topography. The ray tracing results are shown in map view of SmS bounce points (figure 15) and two dimensional cross sections of ray paths (figure 16). The bounce points show a relatively coherent wavefront reaching the array. This is also illustrated in the cross section of ray paths. The cross section of ray paths for this

event show the even spacing of rays that one expects for rays bouncing between nearly parallel surfaces. The Lg rays in this case remain coherent out to a range of 600 km.

The ray synthetics (figures 6b, 11b, 14b) are calculated for events 1-3. The ray synthetics show large variation for azimuths that differ by as little as one degree in regions of steep Moho gradients. The synthetics for events 1 and 2 differ in content and amplitude as a result of ray tracing through Moho topography associated with the Hindu Kush and Pamir mountain ranges. The synthetics simulating event 3 have similar amplitudes and arrivals across the array as a result of ray tracing through relatively flat Moho topography associated with the region east of the array. Although there is little hope with a simple homogeneous crust of reproducing the coda complexity seen in the data, the time spacing and amplitudes of individual SmS rays are useful in assessing affects on the complete Lg coda.

Reflectivity (Fuchs and Muller, 1971) synthetics are used to model event #3 from the Tien Shan region to the east, where there is little variation in crustal thickness. A velocity model is assumed from the JSPC technical note, with Moho depth taken from mean values along this path in the Fielding database. Using this structural model, the Lg to Pg amplitudes do not match well. A simple trial and error inversion is performed by comparing the synthetics varying Q values to fit the waveforms from event#3 (figure 17). . The results from a preliminary crustal model and Q values similar to those in New England (Pulli, 1984) show little resemblance to the event #3 and suggest that the event may be mislocated. Synthetics assuming a location 100 km closer to the array provide a better match to the observed waveform, suggesting that mislocation can be a severe impediment to interpretation of propagation from some of the events in this region.

2.4.2 CNET

While specific paths may have particular interest, a broader assessment of regional

propagation can be obtained by shooting the rays outward from a station. In this way it is

possible to make propagation predictions over the entire 360 degree azimuthal range from

an array, including paths from regions in which natural seismicity is absent. The

justification for doing this lies in the reciprocity theorem for the elastic Green's function.

Figure 18 shows the triggered events within 10 degrees of CNET for 1992. Regional data

observed at CNET has an azimuthal dependency. Events located to the east of CNET are

observed to exhibit strong Lg excitation. Figure 19a shows a typical event with strong Lg

from the region to the east. Events to the southwest of CNET are observed to have

relatively weak or unidentifiable Lg, this has also been noted in a study of Lg/P ratios by

Abers (1995). Figure 19b shows a typical event from the south-southwest that exhibits

weak or absent Lg. Crustal and basin thickness variations in the vicinity of CNET and

ILPA taken from the Fielding data set are illustrated in figure 20. CNET lies near a strong

gradient in Moho thickness associated with the Caucasus and other strong gradients

associated with the Black Sea to the southwest.

The ray study in this region is centered on station KIV in CNET. Predictions of Lg

efficiency are sought by modeling the region using variations in crustal thickness as well as

variations in basin thickness. Rays are shot at dip angles of 60, 70 and 80 degrees.

Sources are located at both shallow (1 km) and mid crustal (15 km) depths. A map view of

bounce points for the model that has only crustal thickness variations is plotted in figures

21a,c-23a,c. The Fielding data set for basin thickness was then implemented in the velocity

model and the same tests were run. A map view of bounce points for rays in the CNET

model with both crustal and basin thickness variations is plotted in figures 21b,d-23b,d.

The large scale effects of the three-dimensional varying surfaces of the Moho and basins on Lg efficiency are strongly correlated with steep gradients in those surfaces. In regions of steep Moho gradients only (no basins), rays are bent and blocked significantly, and the trends in Lg efficiency are fairly easy to follow with the eye. Strong defocusing is predicted to the west and southwest of CNET, where events showing weak or unidentifiable Lg are located. Adding basins to the ray modeling greatly amplifies the effects from the Moho and decreases the coherency of the Lg wavefronts. Some of rays responsible for segments of Lg coda may be trapped in the basins (figures 21b,d-23b,d), where there may be local amplification. For shallow events of 1 km depth (21b-23b), basins play a major role in scattering and blocking the rays, as the rays start out trapped in the basins and may get blocked at the basin crust boundary. For the deeper events of 15 km, Lg rays in the model having only Moho variations seem to propagate more coherently than the those from the shallow crust. Deeper events in the model with both basin and Moho produce rays that may propagate 100 km before getting trapped in the basins. For many azimuths, the Lg does not get trapped in the basins at all.

For the CNET array, the effects due to the thinning of the crust under the Black Sea is accentuated by thick sediments and rays are strongly scattered and blocked. This is seen in the map view plots of both ray paths and of SmS bounce points (figures 21-23). The ray path plots illustrate the three dimensional nature of the scattering, where some rays undergo severe bending over small distances of 100 to 200 km.

2.4.3 ILPA

The observations for Lg used in this study are those of Sweeney (1996). Sweeney, reviewed the 200 plus events in the data set, performing seismic phase picking and data

14

quality analysis. Phases were identified as present only if the phase was distinct and unambiguous. Phases identified as Lg were timed on the vertical channels. Sweeney's plot of the Lg/P ratios are shown in figure 6. In the figure, events for which a phase is present are plotted using a filled dot; where the indicated phase is not present, the event location is plotted using a doughnut. The propagation path in each case is from the event to the location of the array. The locations of important faults and the locations of Quaternary volcanic centers (triangles) are noted as well.

Rays used in the ILPA were calculated as in the CNET array. A source was located at a single station and rays were shot for depths of 1 and 15 km, as well as for take off angles of 60 ,70, and 80 degrees. A map view of bounce points for rays in the ILPA model with both crustal and basin thickness variations as well as variations in source depth and take off angle is plotted in figures 24-26.

The Moho (without basins) effect is moderate with blockage and scattering to the north and north-west: (figure24a,c-26a,c). Propagation past 500 km is generally highly incoherent. Near ILPA the Moho is relatively flat and it is the basins that do the most scattering of Lg. A main feature that blocks rays to the north of the array for both the shallow and deep sources is the deep basin that is beneath the Caspian Sea. This ray blockage is seen from 38E to 42N to 55E to 38N (figures 24-26) and agrees well with the low Lg to P ratios seen by Sweeney (1996) (figure 24) and with prior studies of Wallace et al, (1992) who observed inefficient Lg propagation across northern Iran and the southern Caspian region, and with Kadinsky-Cade et al. (1981) who found that for travel paths across the southern Caspian region, the Lg phase is scattered or blocked. Maps of bounce points from models with basins differ greatly between a shallow and mid-crustal source. This is due to the shallow sediments to the south and east of the array and may provide a means of depth discrimination in the area. The northwest trend in trapped bounce points seen south of the

15

array from the models with basins included (figures 24b,d-26b,d) may be associated with the plate boundary and the Zagros fault. This correlates well with the low Lg/Pg ratios seen in Sweeney's plot south of the ILPA array.

2.5 Summary of ray experiments on Lg propagation

2.5.1 Crustal thickness variations

The most important effects of large scale structure, including strong Lg attenuation and blockage, can be estimated from deterministic crustal models based on regional refraction and deep seismic reflection surveys, surficial topography, and gravity. Crustal and basin thickness variations have been incorporated into ray tracing models for the purposes of modeling regional Lg wave propagation. Ray tracing predicts the strong regional variations seen in Lg efficiency due to strong Moho gradients seen in data collected at the Kyrgyz array. The plots of the SmS bounce points for the events in this study suggest that a large transition in Lg amplitudes occurs for paths traversing regions of strong Moho gradient associated with the Hindu Kush and Pamir mountains. An effect of crustal thickness variation is a modification of SmS ray paths that results in either a compression or stretching of Lg coda. In regions of uniform crustal thickness, however, reflectivity CRFL synthetics yield reasonably good fits to observed data. For example, in the Tien Shan region east of the KNET array, the Moho topography is reasonably flat, and one-dimensional modeling yields new estimates for seismic Q that are slightly lower than the previous values for the region.

2.5.2 Effects of basins

Incorporation of sedimentary basins in ray modeling of Lg at CNET and ILPA shows that thick basins may have large effects of shallow crustal sources, blocking a either a portion or all of the Lg phase along paths crossing these basins. The basin effects are strongly sensitive to source depth, nearly vanishing for sources in the deep crust. In some regions, the depth sensitivity of the basin effect may provide the basis for the construction of an event discrimination by source depth from Lg amplitudes.
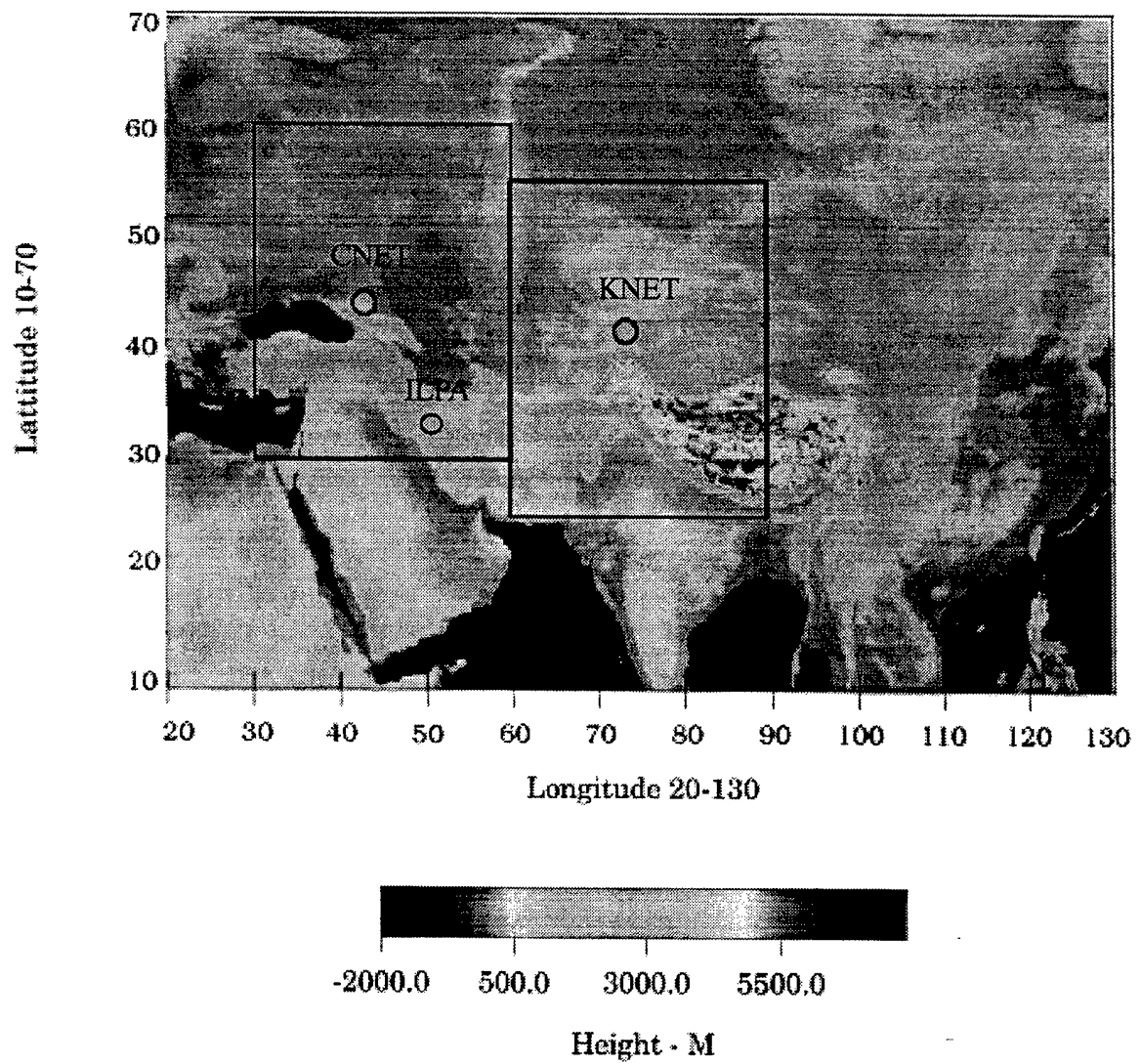
Figure 1: This topographical map of Eurasia illustrates the location of the three seismic arrays in the regions studied (ETOPO5, 1988).
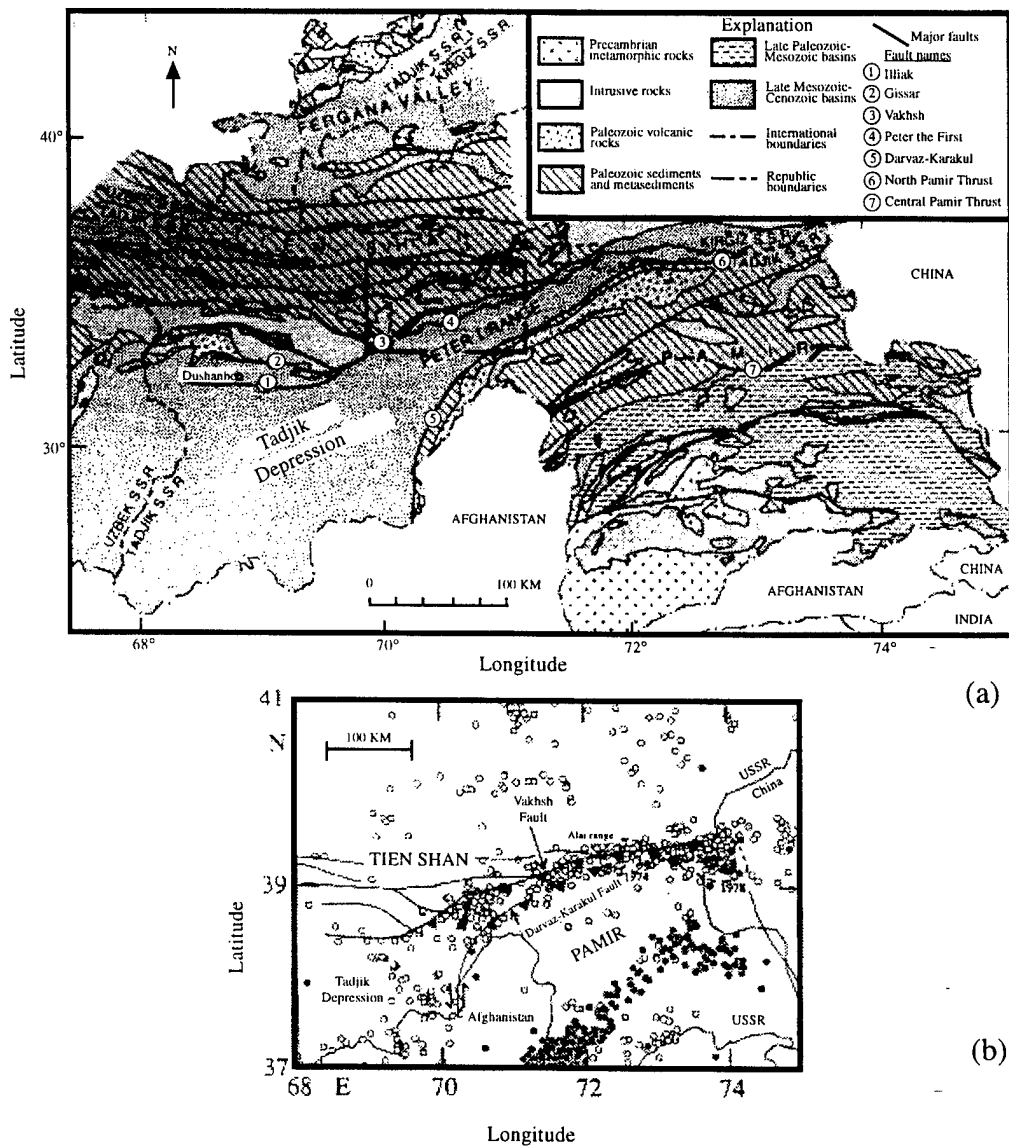
Figure 2: a) Regional geology and b) seismicity and major faults of the Garm region. *(M. Hamburger, Geophys. J. Int., 1993)*

Kazakhstan

Talas-Fergana fault

Fergana Basin

S.Ghissar

Tien Shan

6

Vakhsh

13mm/yr

Tadjik Basin

Pamir

40°

Herat fault

Tarim Basin

Hindu Kush

20mm/yr

Afghanistan

30mm/yr

Tibet

Chaman fault

32mm/yr

Karakoram fault

30°

Himalaya 18mm

India

50mm/yr

Latitude

70°   80°   90°

Longitude

6mm/yr   Shortening rate   /   Slip vectors

30mm/yr   Strike-slip rate   Zones of active shortening

10mm/yr   Extension rate   Direction of rotation

Figure 3: Map of the Himalaya and central Asia, based on Searle's (1996) interpretation
of Avouac and Tapponnier (1993) showing zones of presently active crustal shortening
and estimated kinematic rates of shortening, extension, and strike-slip fault motion.
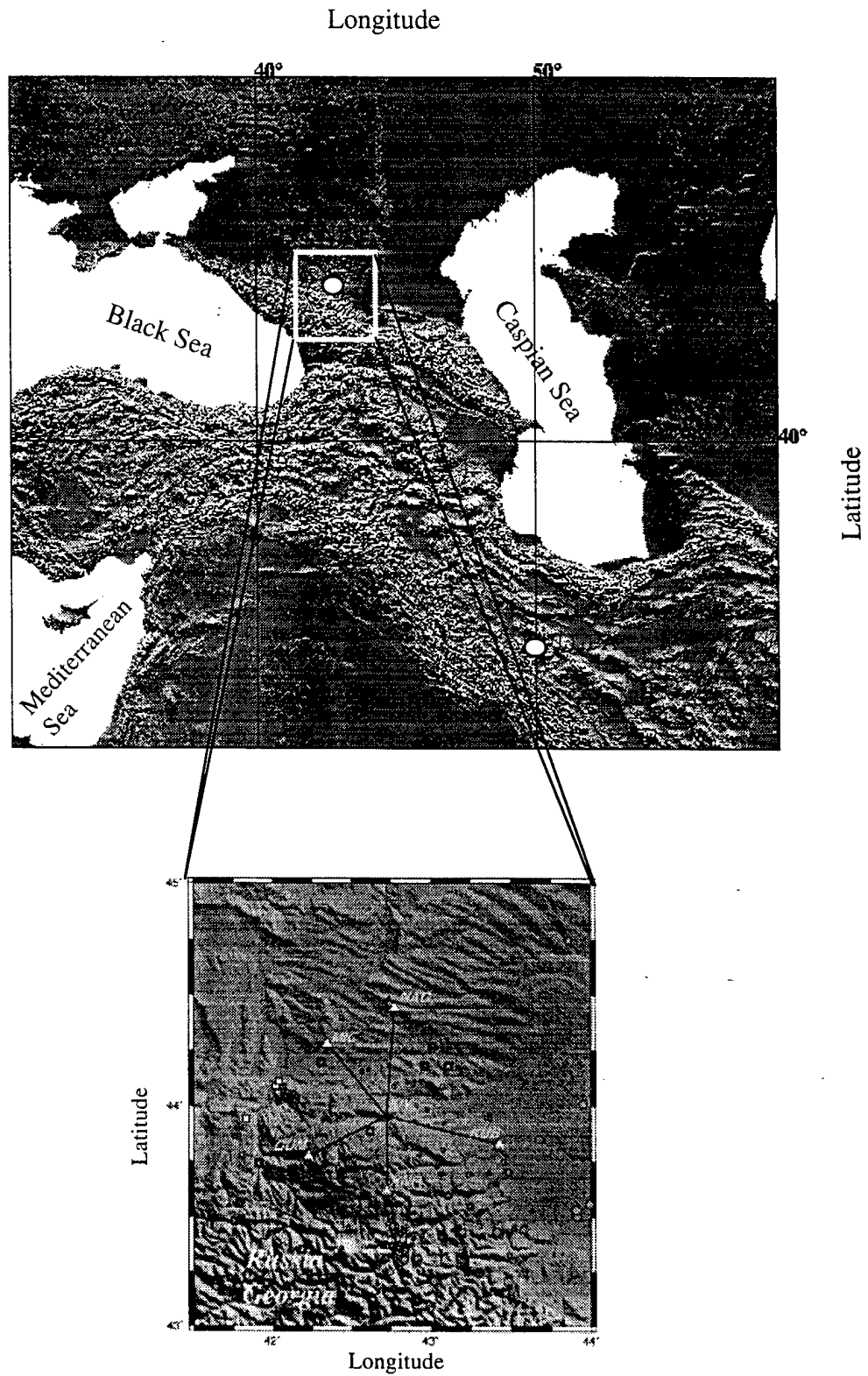
Figure 4a: Topography in the vicinity of the CNET and ILPA arrays, with an exploded

view (JSPC 1992) of the Caucasus array.
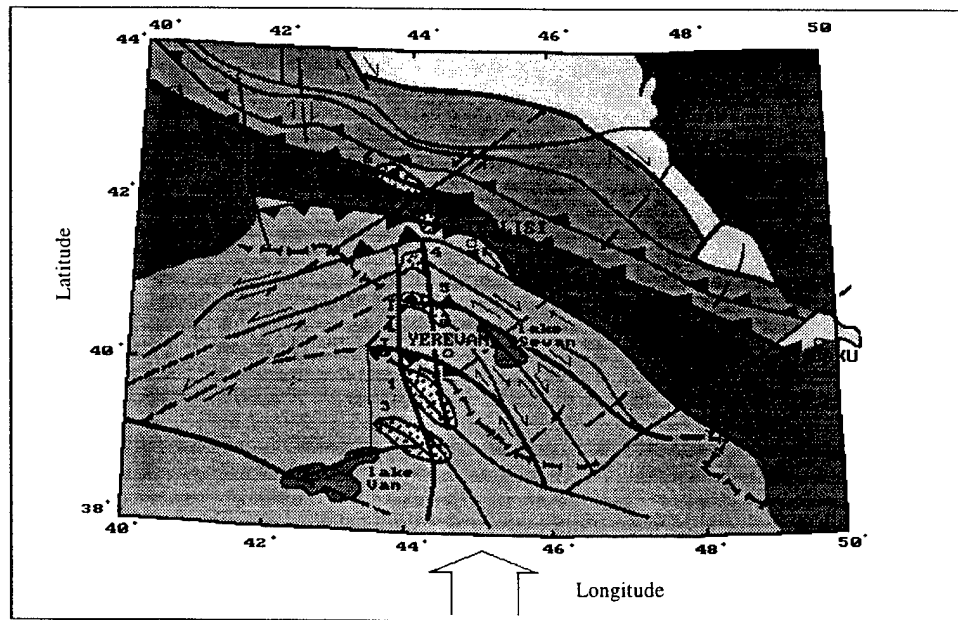
Figure 4b: CNET/Caucasus faults and tectonics.(Rhogozhin and Phillip, 1991)
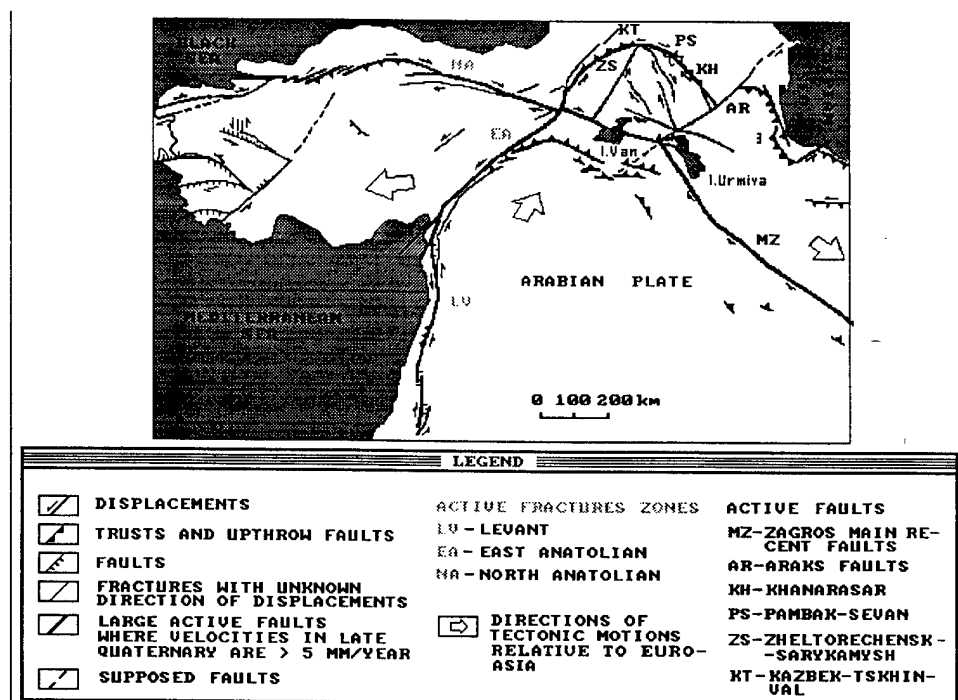
Figure 4c: Tectonic setting and major active faults near CNET and ILPA arrays (Spitak

Earthquake database for 1997)

Station Code	Station Name	Latitude (deg)	Longitude (deg)	Elevation (km)
AAK	Ala-Archa	42.6333	74.4944	1.6800
AML	Almalyashu	42.1311	73.6941	3.4000
BGK2	Belogorka	42.6451	74.2274	1.6400
CHM	Chumysh	42.9986	74.7513	0.6550
EKS2	Erkin-Sai	42.6615	73.7772	1.3600
KBK	Karagaibulak	42.6564	74.9478	1.7600
KZA	Kyzart	42.0778	75.2496	3.5200
TKM	Tokmak	42.8601	75.3184	0.9600
UCH	Uchtor	42.2275	74.5134	3.8500
USP	Uspenovka	43.2669	74.4997	0.7400

Table 1. Kyrgyz stations and locations (JSPC, 1993).
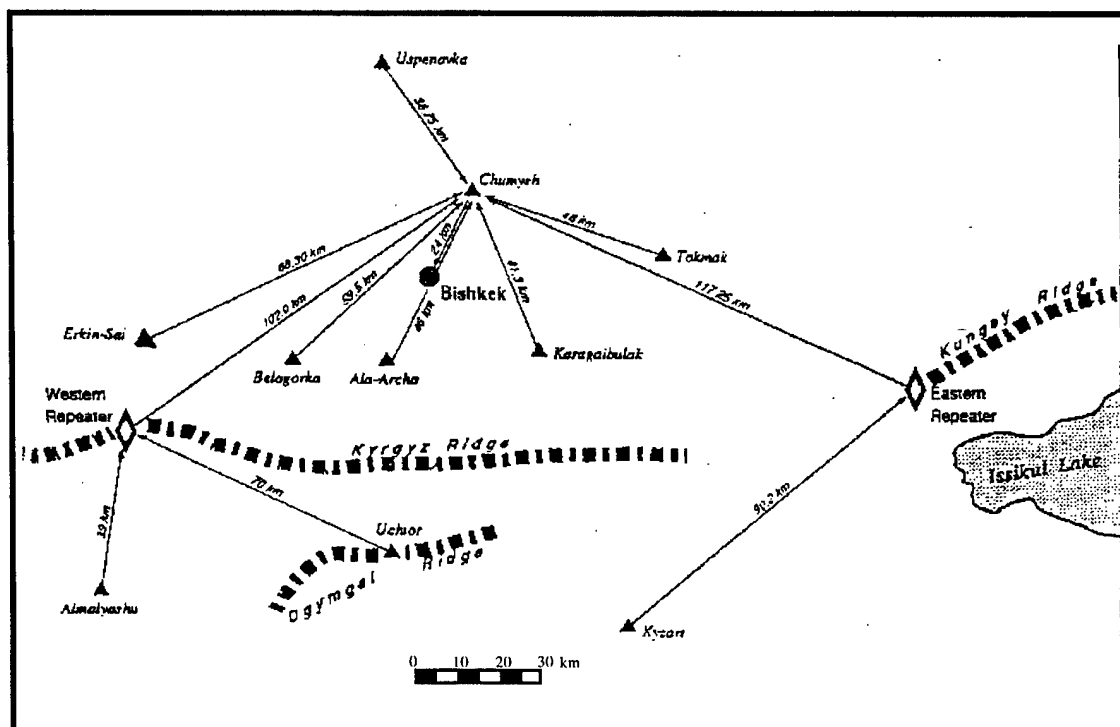
Figure 5: Kyrgyz seismic telemety network (JSPC, 1992).

△	location of Quaternary volcanic center
●	location of event with L $_g$ phase present at ILPA
○	location of event with L $_g$ phase not present at ILPA

MZRF Main Zagros reverse fault   B Borazjan fault   K Kazerun fault
HZF High Zagros fault   (faults after Fig. 1 of Berberian, 1995)
MDF Makran deformation front (oceanic subduction, after Byrne et al., 1992)
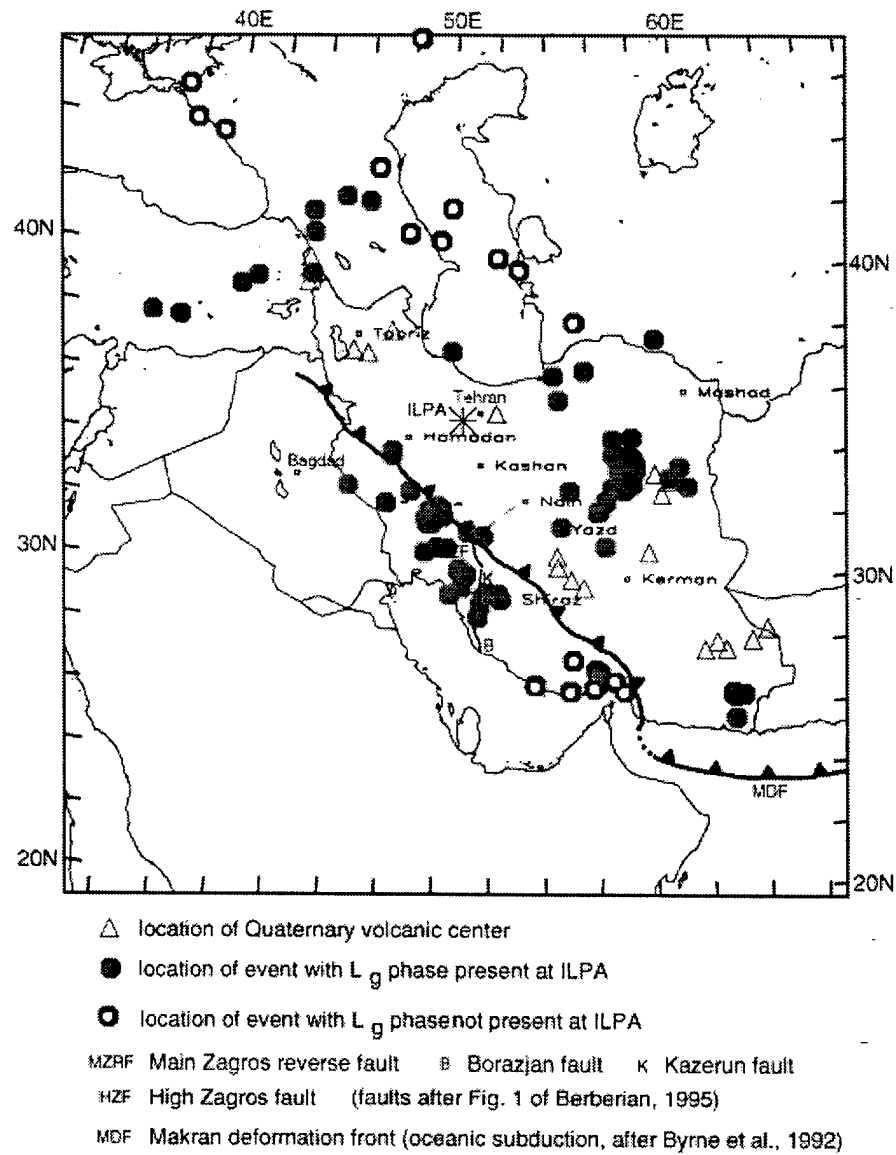
Figure 6: Interpretation of ILPA data (1978-1979): Lg phase propogation and location of ILPA and Lg blockage. Note the Zagros fault system. *(J. Sweeney, 1996)*

Figure 7b: Contour map of Moho topography (crustal thickness)(Fielding, 1992) with 3 events in this study.

Figure 7a: Kyrgyz array and events on contour of Moho topography (crustal thickness) based on Fielding (1992).

Figure 8b: Preliminary ray synthetic of event 1 to stations AAK, CHM, and TKM. The synthetics for the different stations show the effects of the Moho topography associated with the Pamir Range.

Figure 8a: Record section plot of event#1 in figure 7a, 6 May 92. Data were band passed filtered 1-5 Hz. The signals vary greatly across the array, station TKM has little or no Lg.
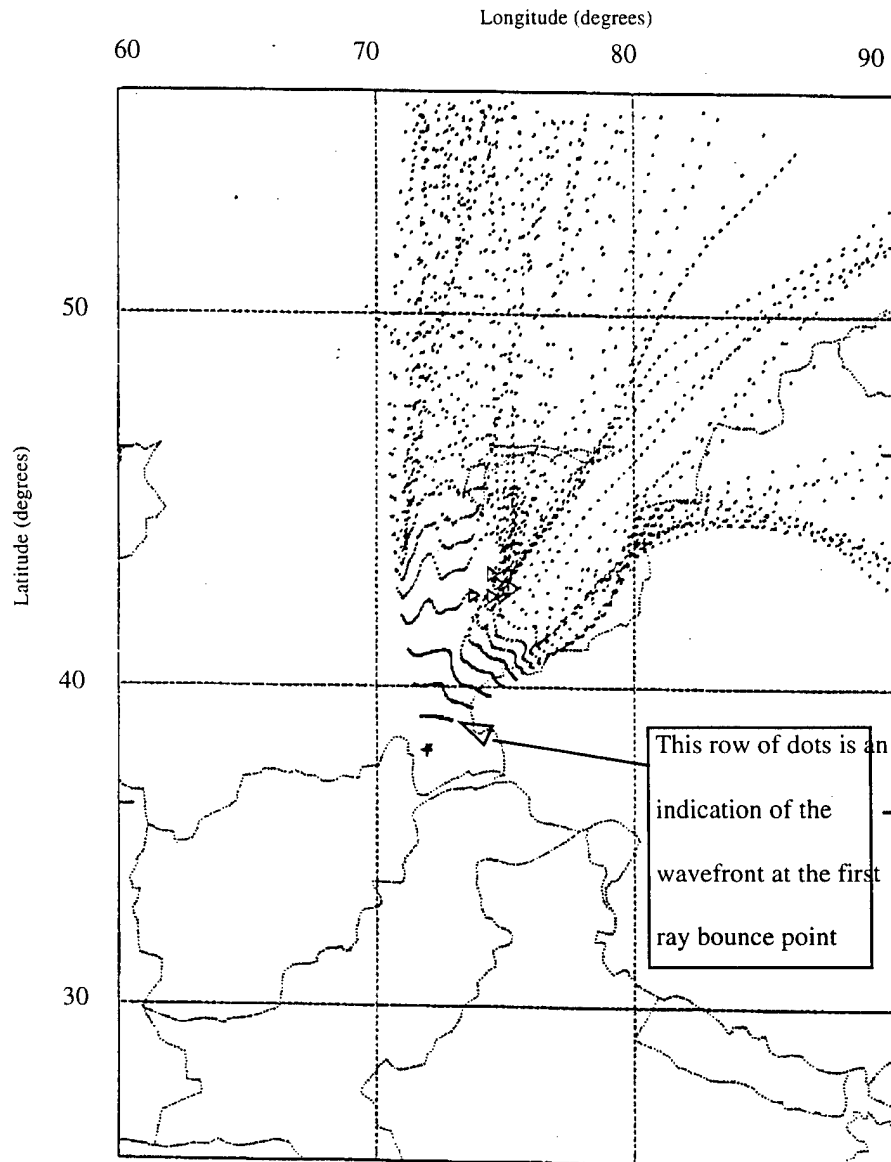
Figure 9: Map view of ray bounce points from dynamic ray tracing for event #1. The wavefront is strongly affected by the steep Moho topography. A two dimensional caustic appears to be forming down the middle of the array.
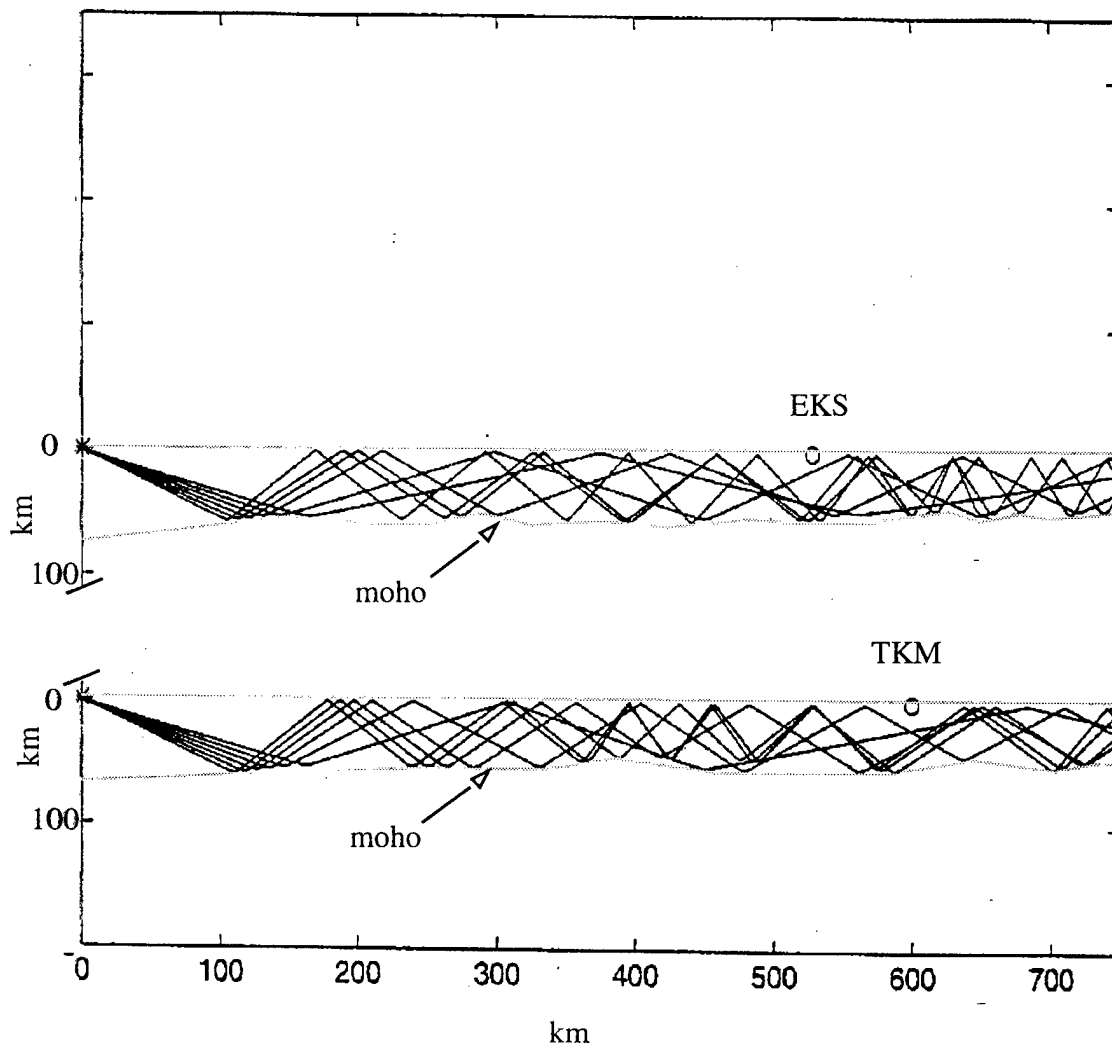
Figure 10: Rays for event #1 at take off angles 63-71 degrees for paths to stations TKM and EKS2. Both paths show development of unique focusing and defocusing of rays due to the gradients in the Moho topography (Fielding, 1992).
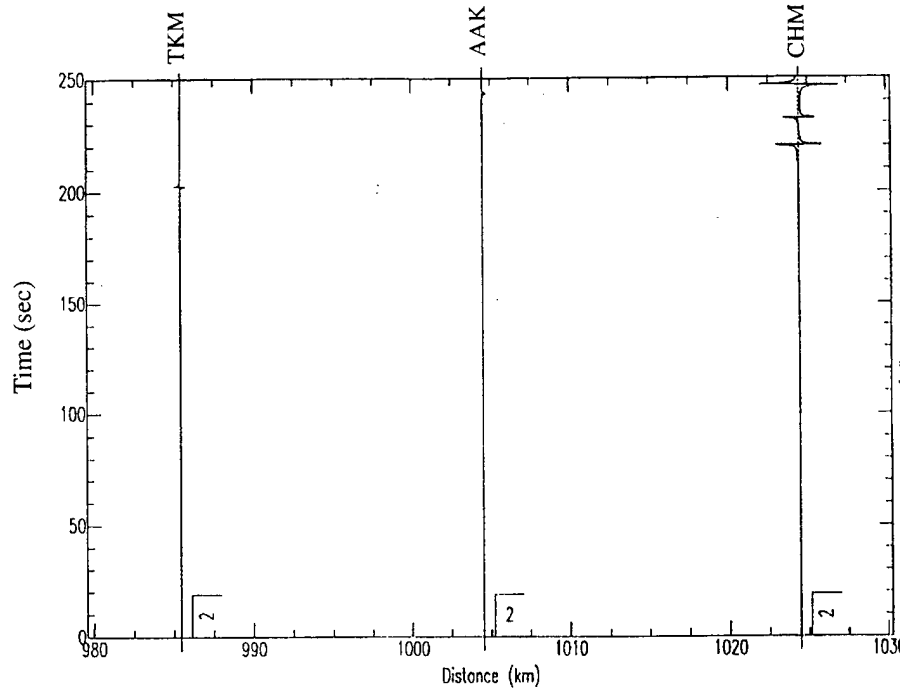
Figure 11b: Ray synthetic of event 2 to stations AAK, CHM, and TKM. The synthetics for the different stations show the effects of the Moho topography associated with the Hindu Kush.
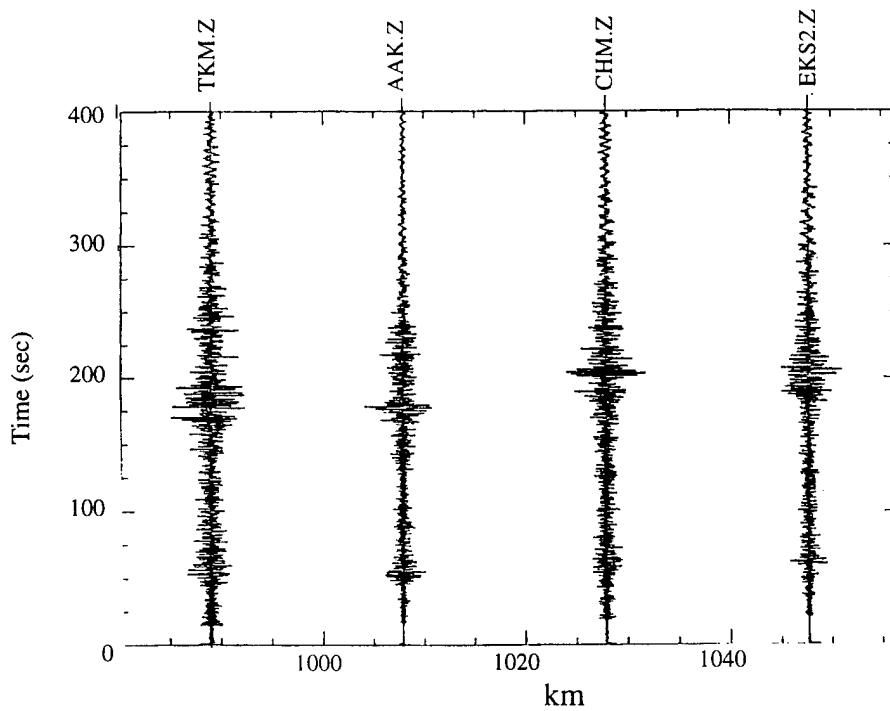
Figure 11a: Record section of plot event #2 in figure 7a, 27 June 92. Data was bandpassed filtered 1-5 Hz. The Lg coda varies across the array.
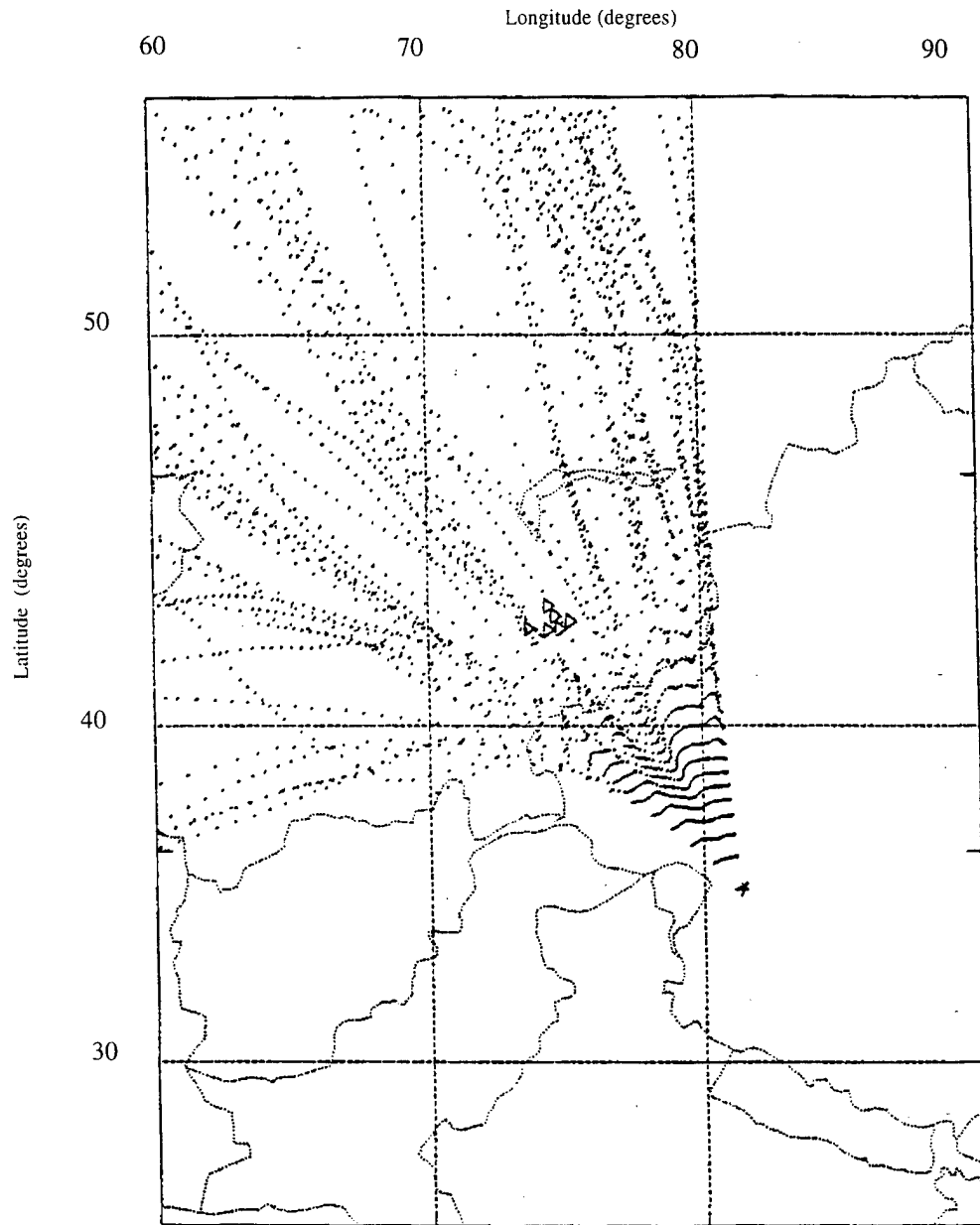
Figure 12: Map view of ray bounce points from dynamic ray tracing for event #2. The wave front bends sharply due to steep gradients in the Moho topography.
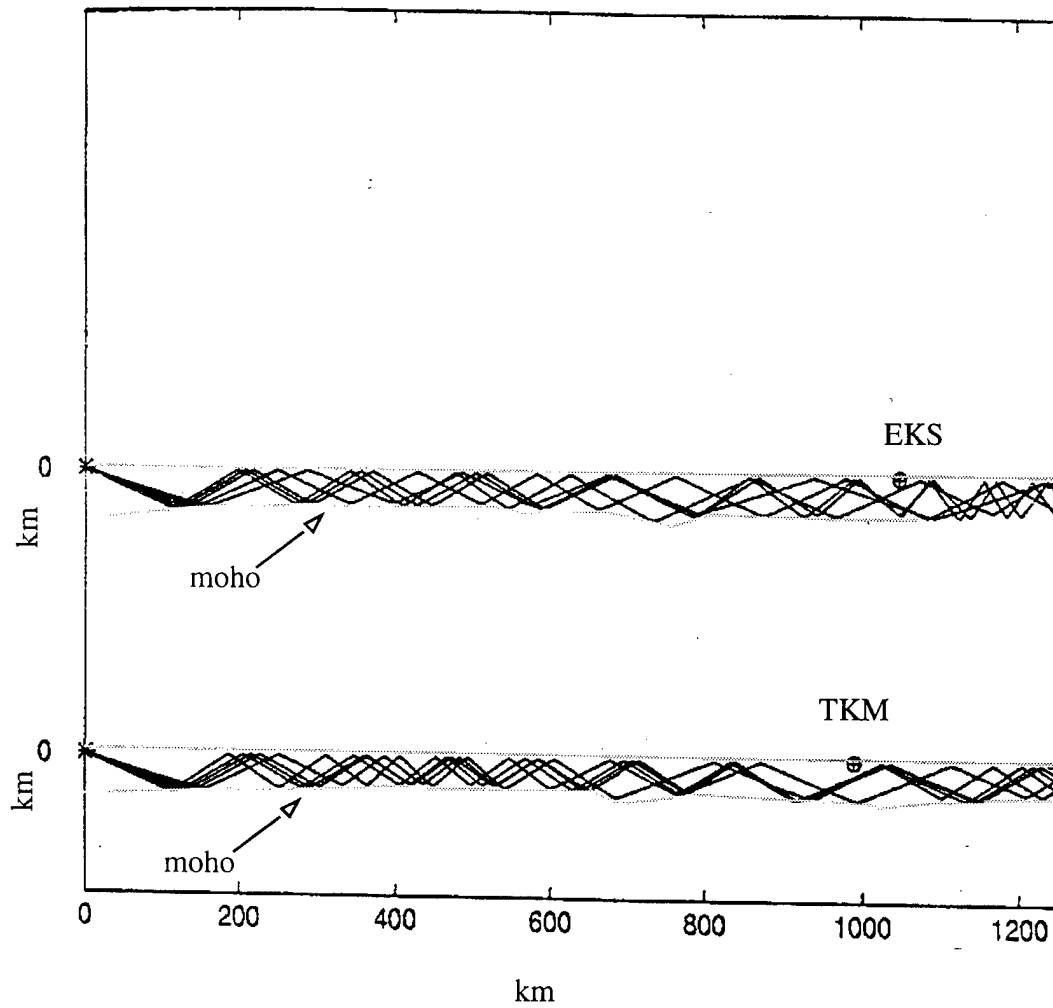
Figure 13: Rays for event #2 at take off angles 63-71 degrees for paths to stations TKM and EKS2. Both paths show development of unique focusing and defocusing of rays due to the gradients in the Moho topography.
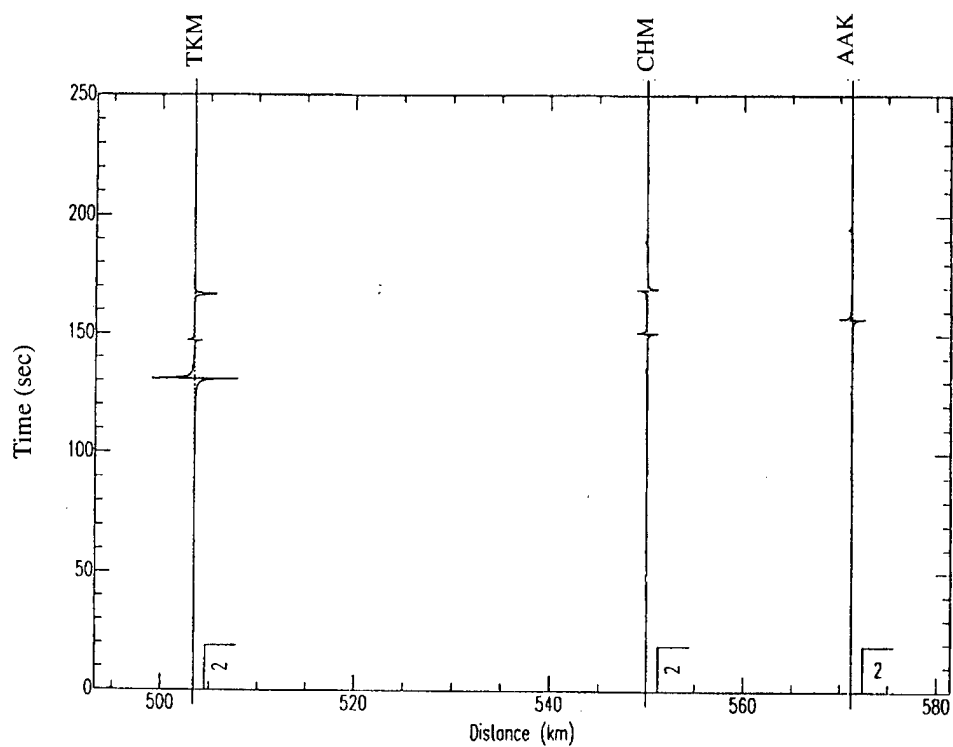
Figure 14b: Ray synthetic of event 3 to stations AAK, CHM, and TKM. The synthetics at AAK and CHM have some of the same arrivals due to the flat Moho east of the array.
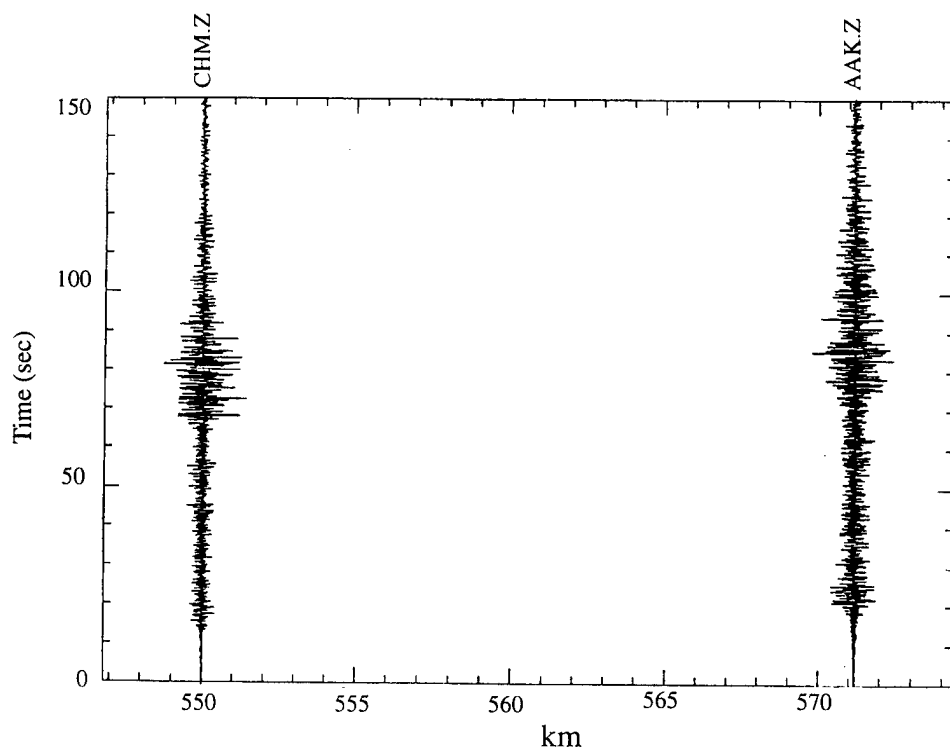
Figure 14a: Record section plot of event #3 in figure 7a, 25 March 92. Data was bandpassed filtered 1-5 Hz.
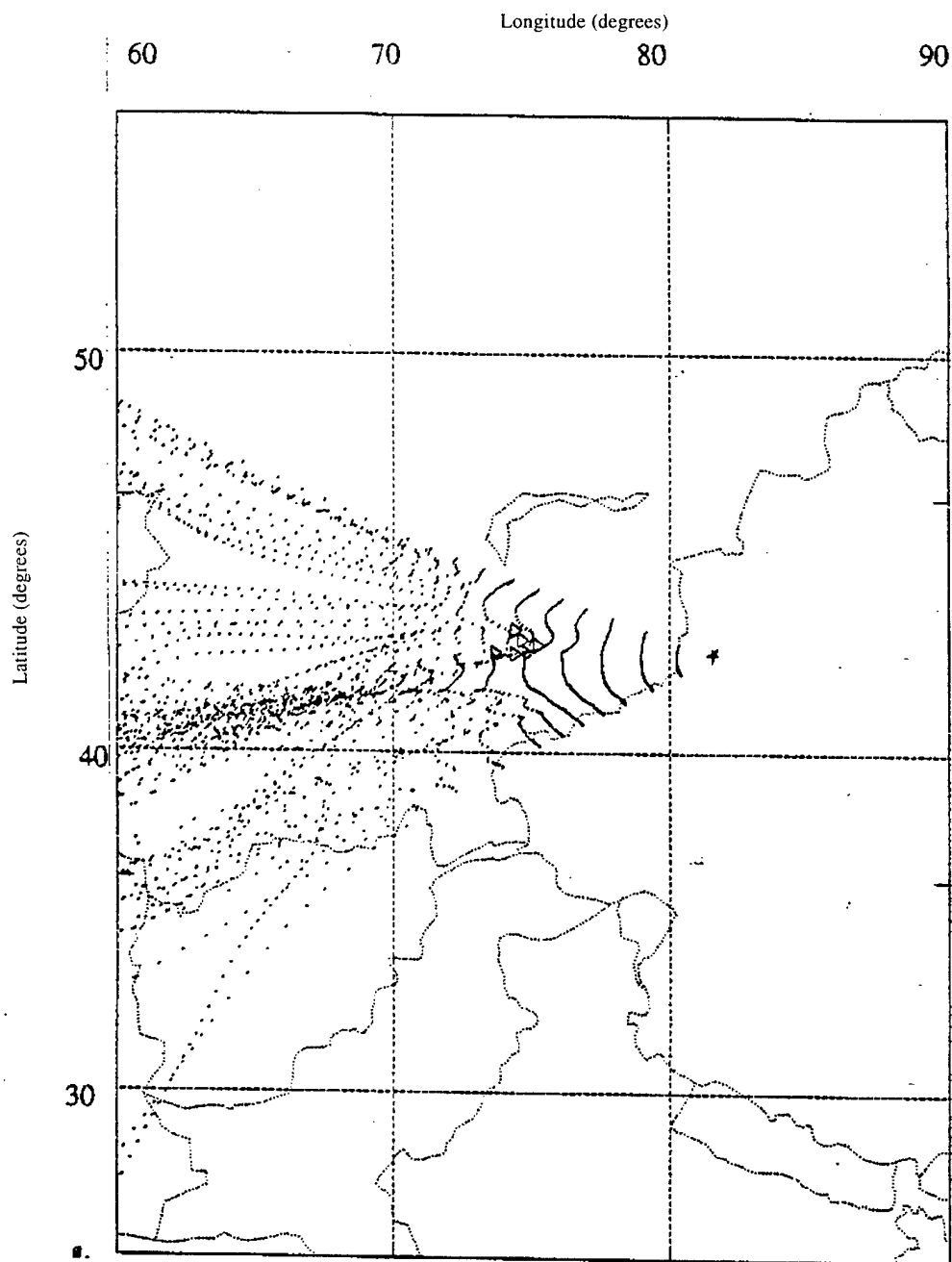
Figure 15: Origin in Tien Shan. Map view of ray bounce points from dynamic ray tracing for event #3. Wavefront appears to remain coherent for 10 bounces.
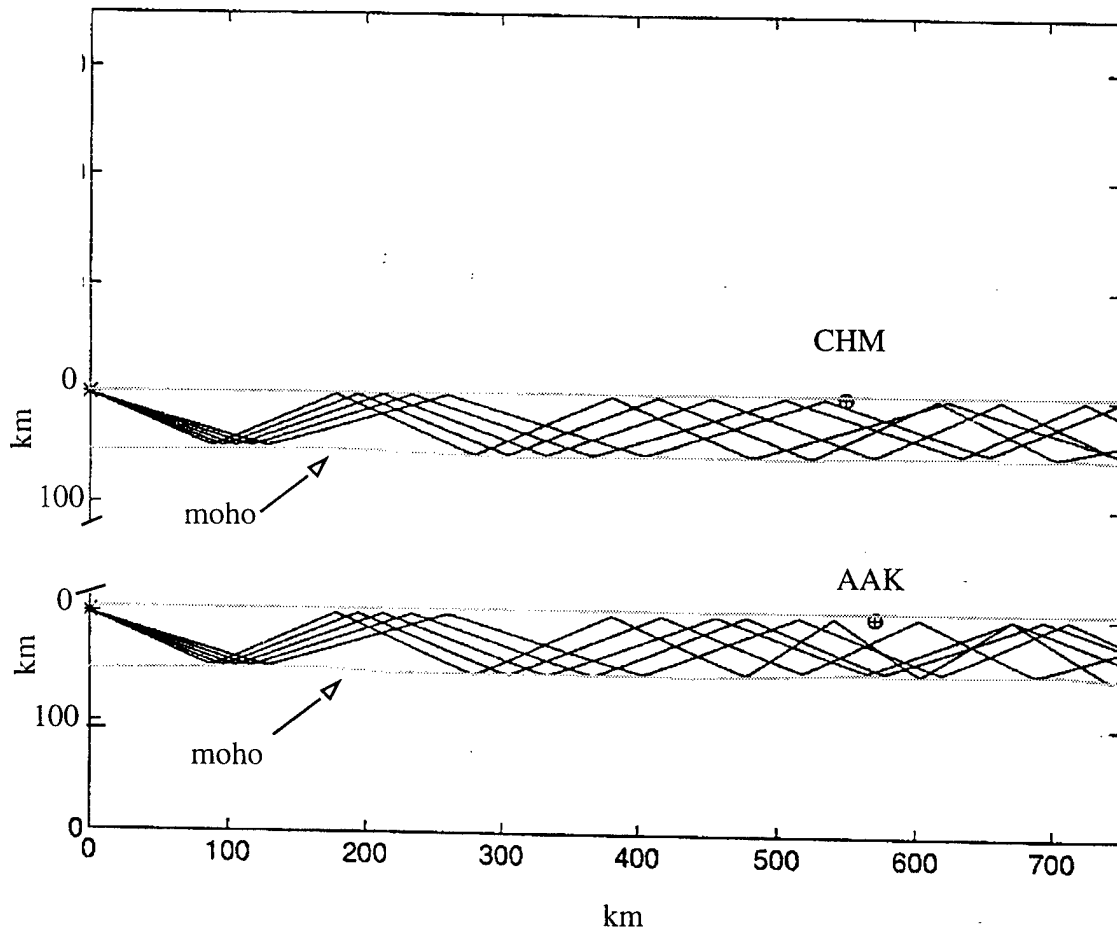
Figure 16: Tien Shan Vertical Cross-section. Rays for event #3 at take off angles 61-69 degrees for paths to stations AAK and CHM. Due to the relatively flat Moho along the ray path, ray paths are similar out to 500-600 km.
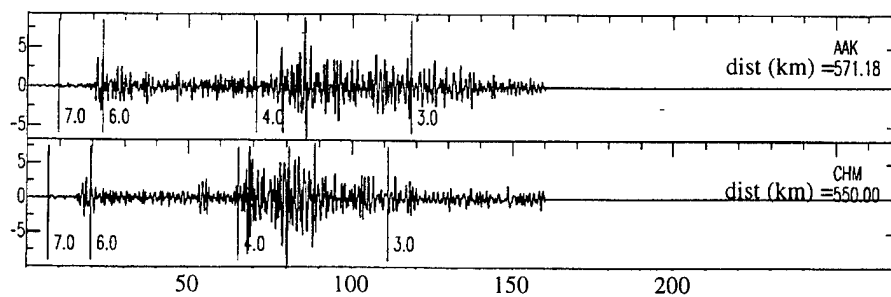
Figure 17a: Seismograms from event #3 recorded at stations AAK and CHM. Band passed 1-5Hz.
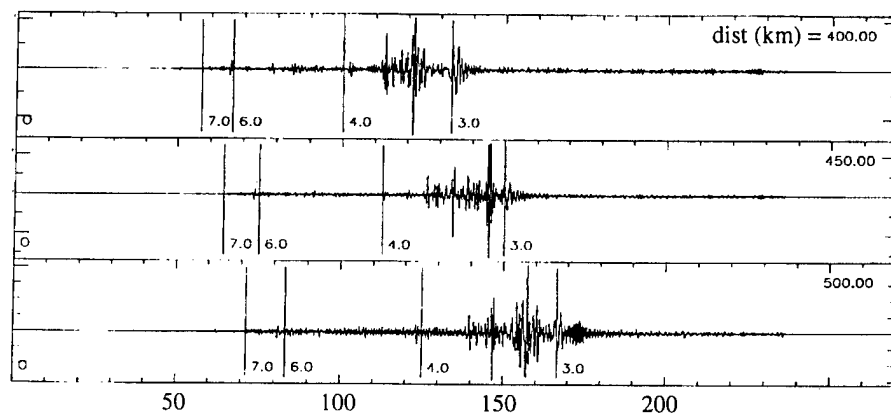
Figure 17b: Preliminary synthetic from CRFL program for event #3.
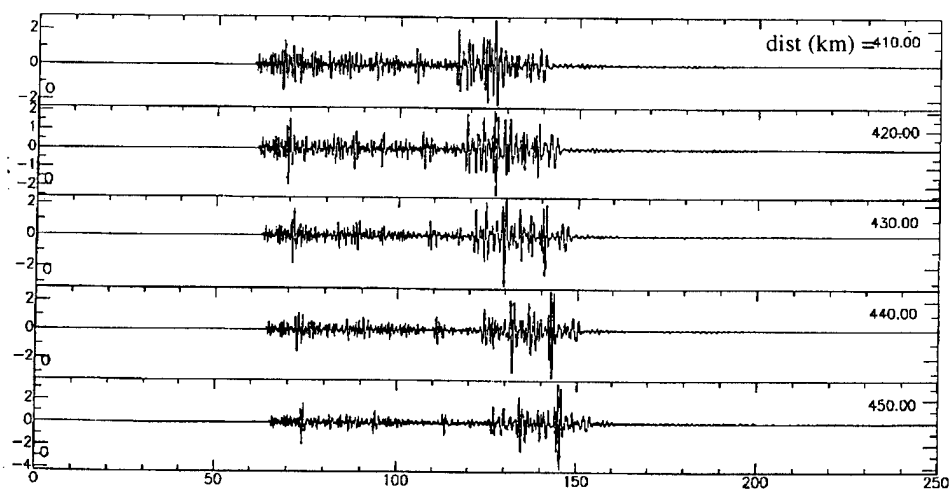
Figure 17c: At ranges of 420-430 km there is a good match in coda length, shape and Lg/Pn amplitude, indicating a need for relocation.
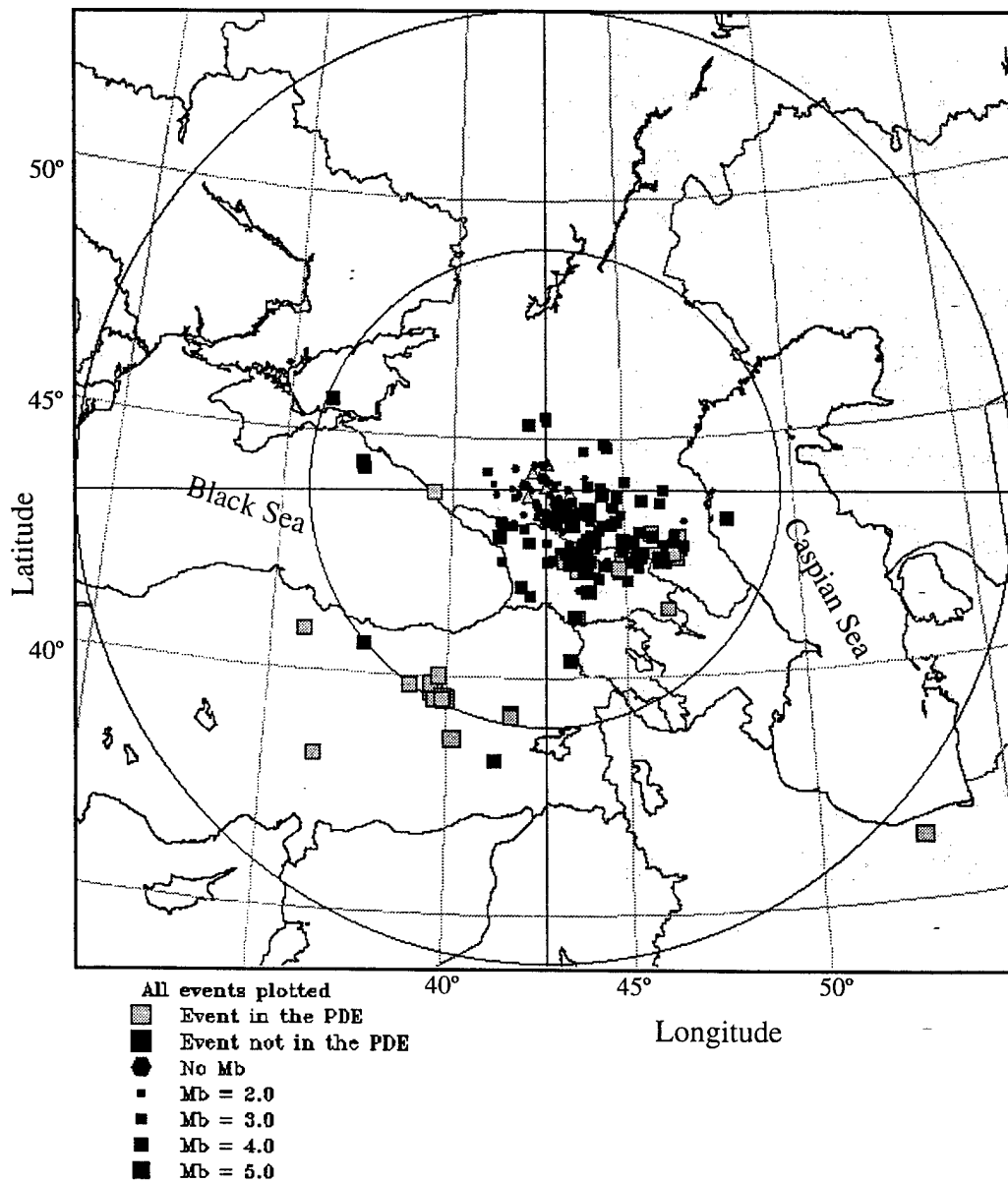
Figure 18: Events triggered during January 1, 1992 to November 9, 1992 from CNET, centered at KIV, circles indicate increments of 5° (JSPC, 1994).

JSPC CNET EVID 21 LAT 42.62 LON 46.29
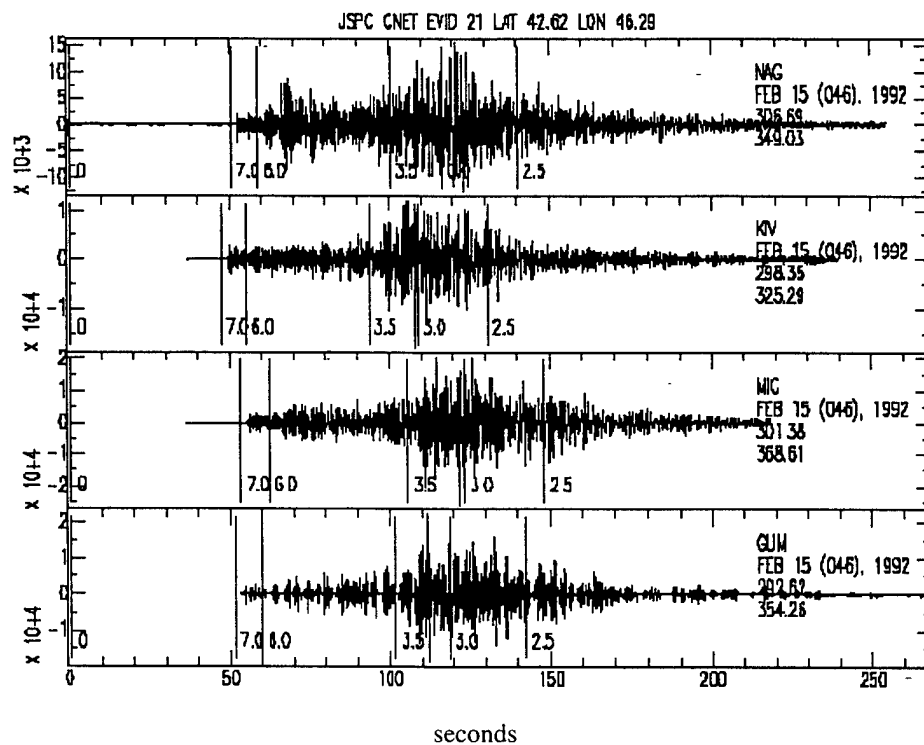
Figure 19a: Example of efficient Lg propagation from an event to the east of KNET.

JSPC CNET EVID 127 LAT 40.60 LON 37.63
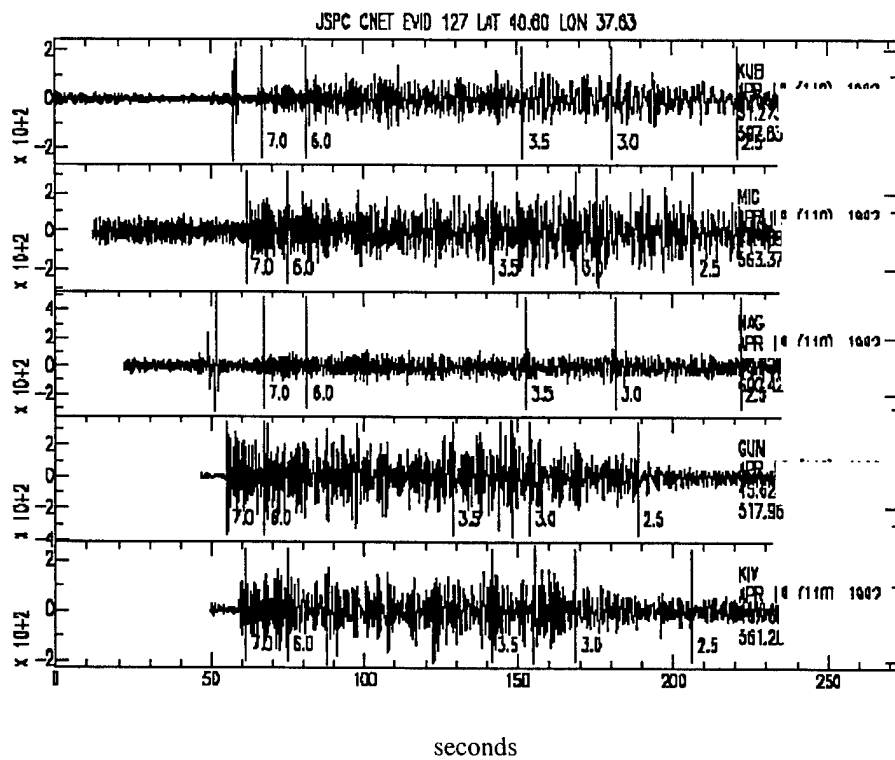
Figure 19b: Example of inefficient Lg propagation from an event to the west and south-west of KNET.
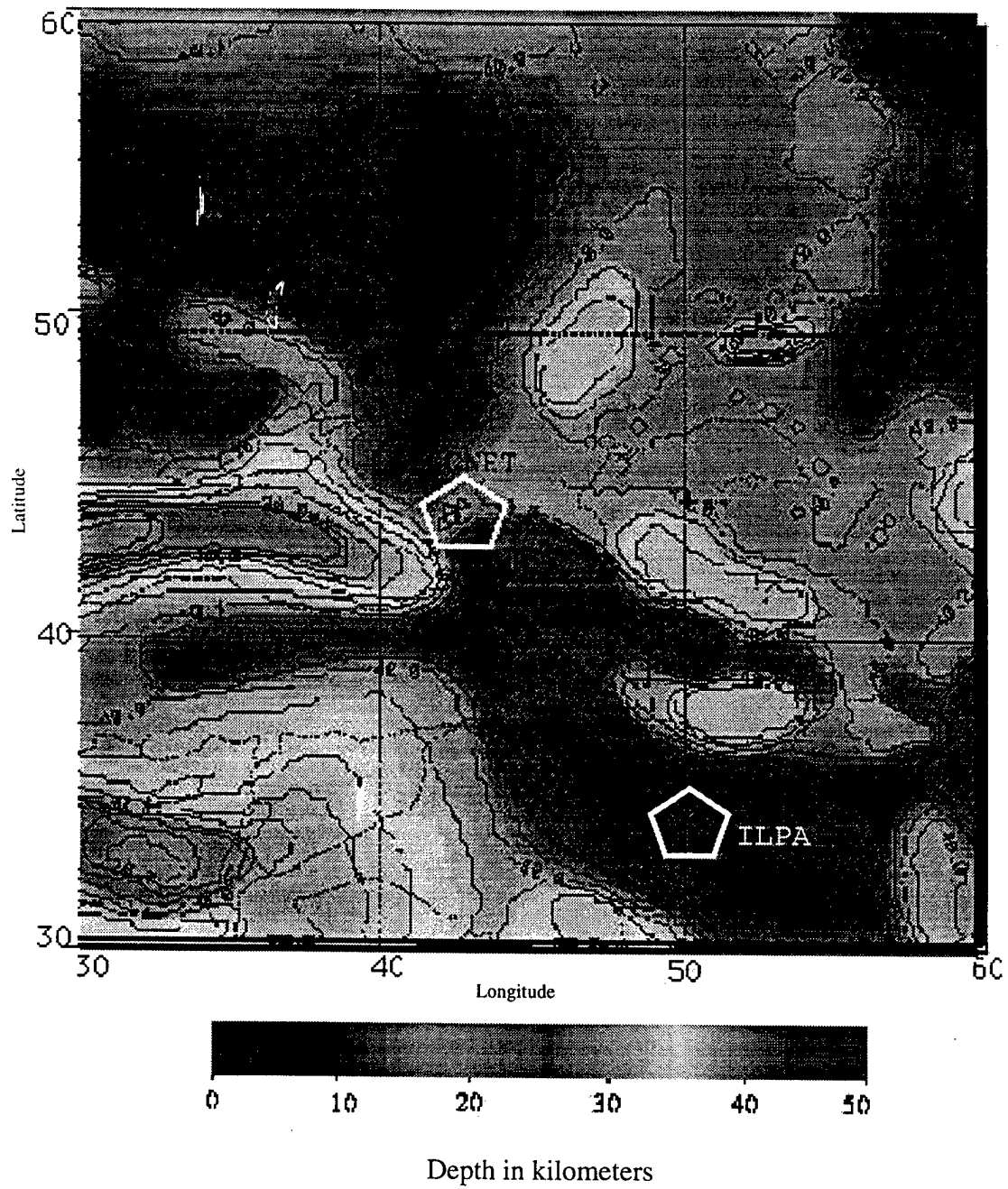
Figure 20: Moho structure in the vicinity of CNET and ILPA arrays based on Fielding et al., 1993.
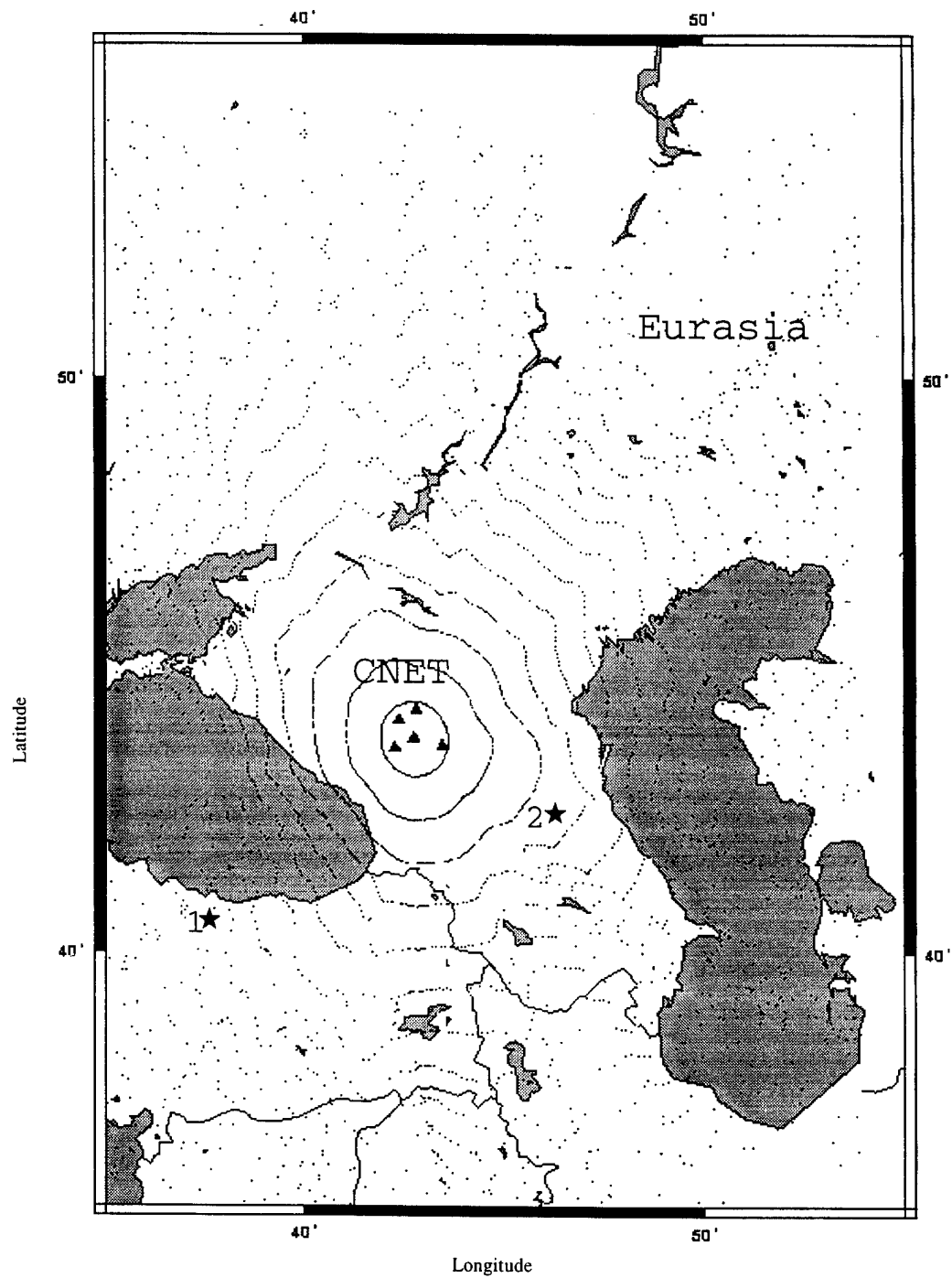
Figure 21a: Map view of ray bounce points from a regional model that includes the
Fielding Moho database. Ray take-off dip angle is 60°, source depth is 1 km.
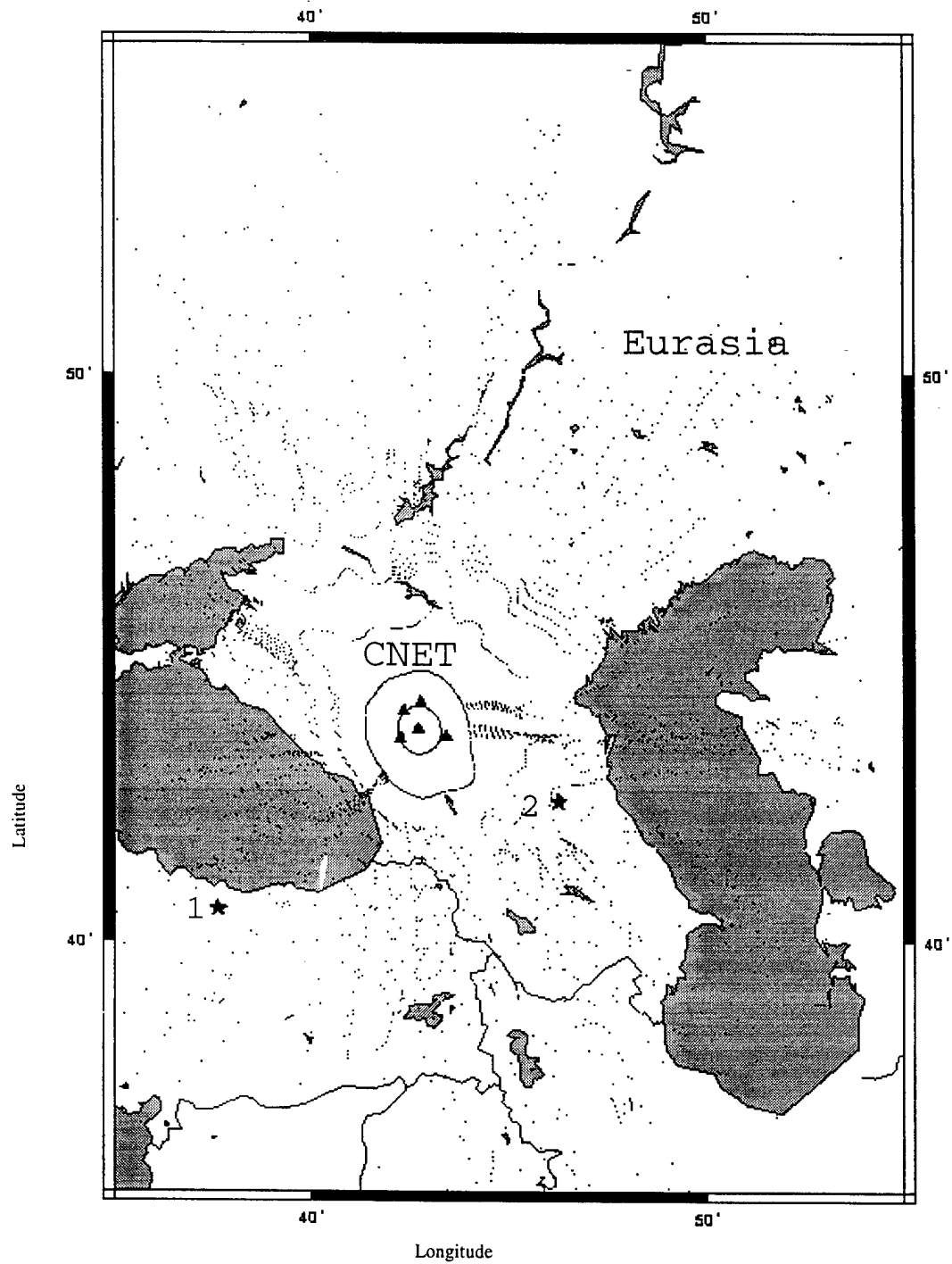Rays were shot at 1° azimuthal increments for 360°.
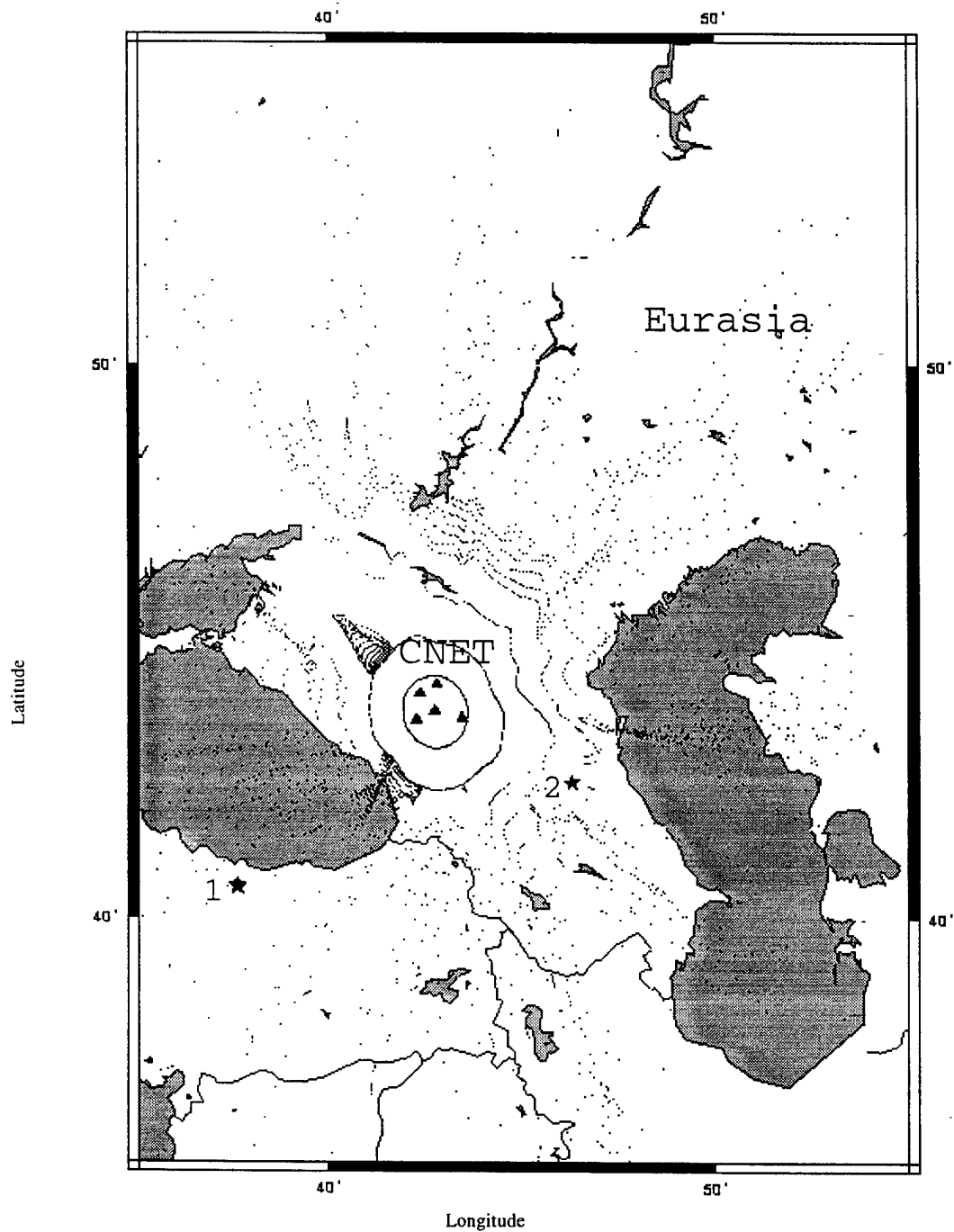
Figure 21b: Map view of ray bounce points from a regional model that includes the Fielding Moho and basin databases. Ray take-off dip angle is 60°, source depth is 1 km. Rays were shot at 1° azimuthal increments for 360°.
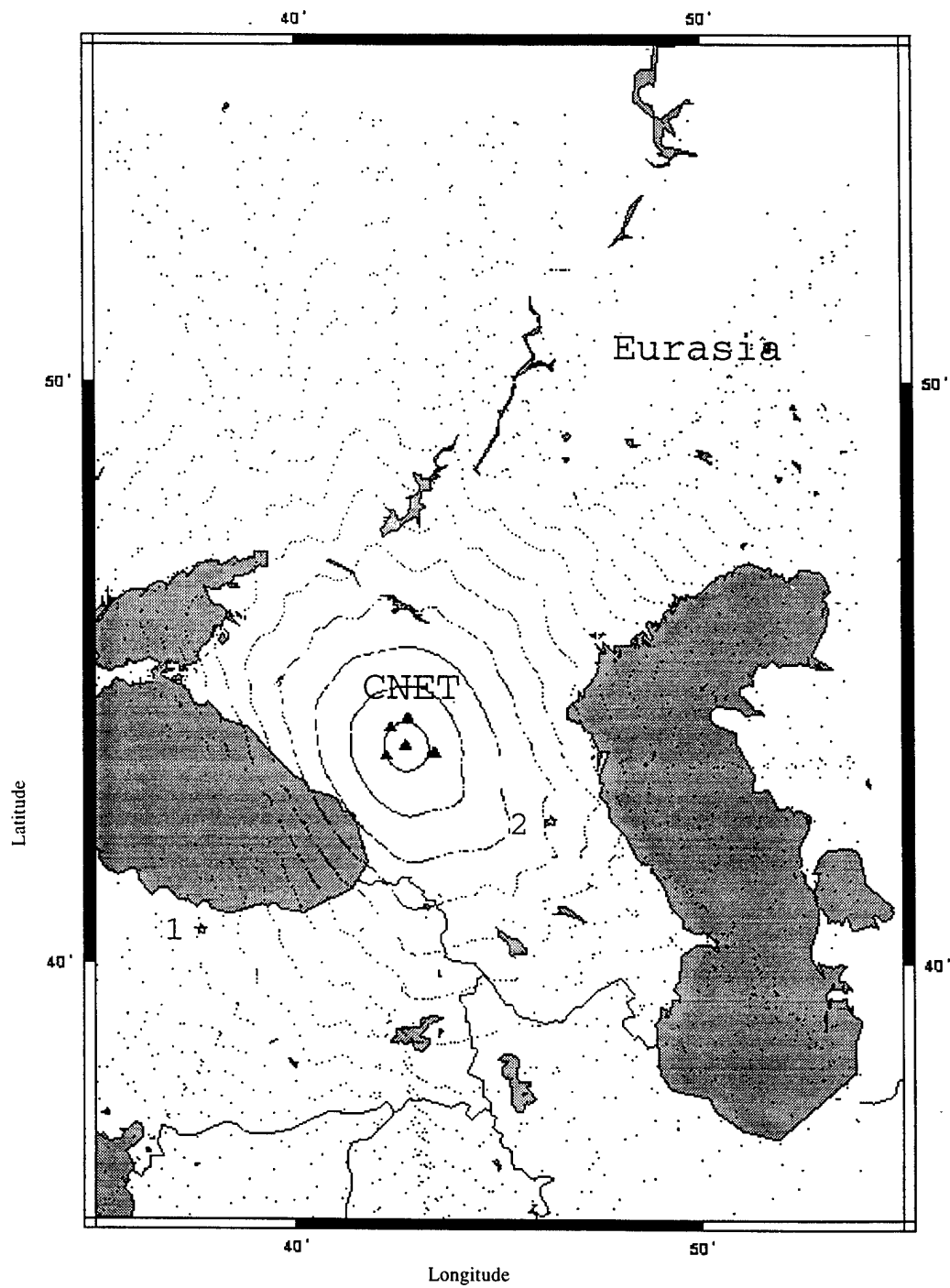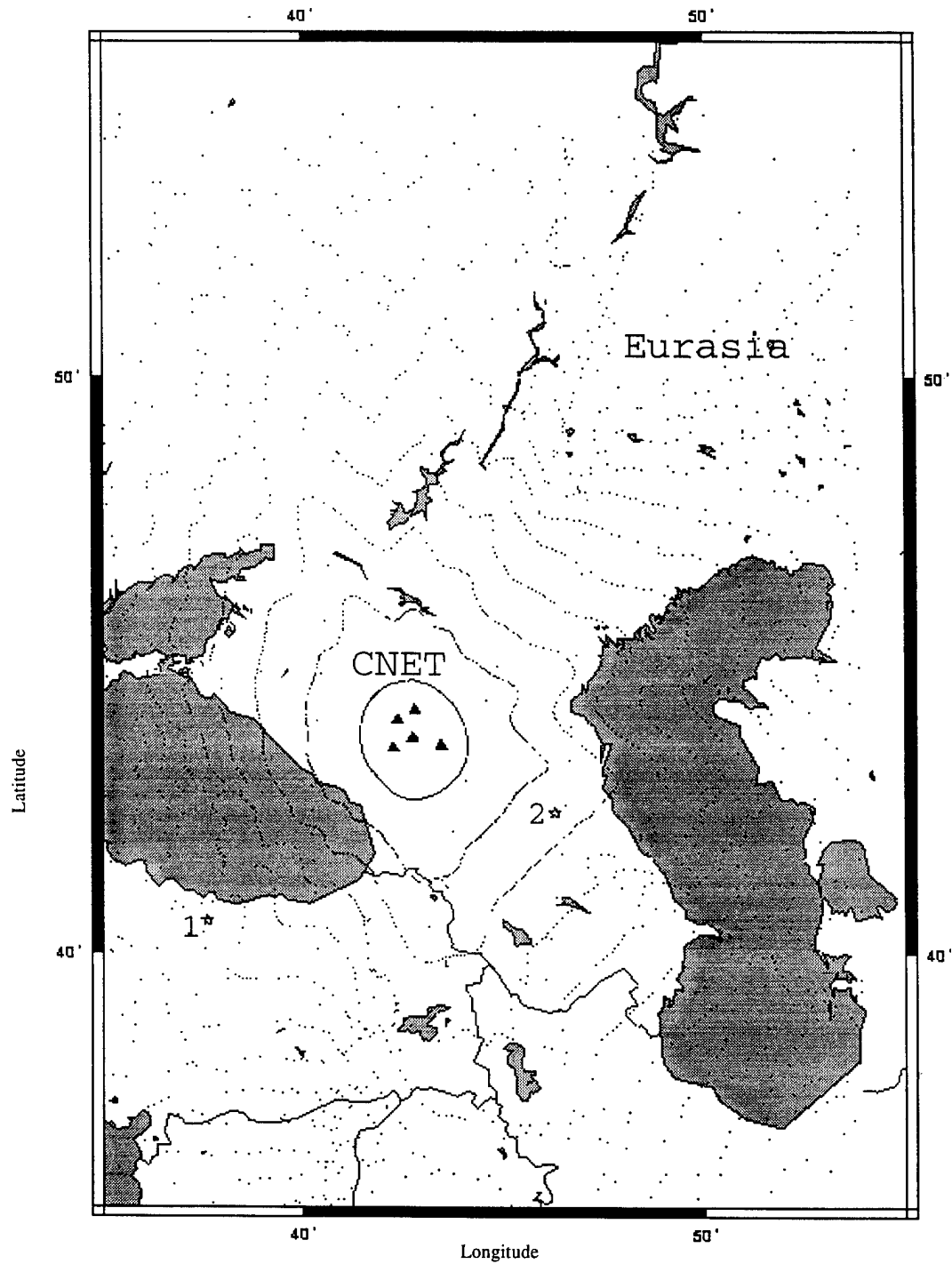
Figure 21c: Map view of ray bounce points from a regional model that includes the Fielding Moho database. Ray take-off dip angle is 60°, source depth is 15km. Rays were shot at 1° azimuthal increments for 360°.
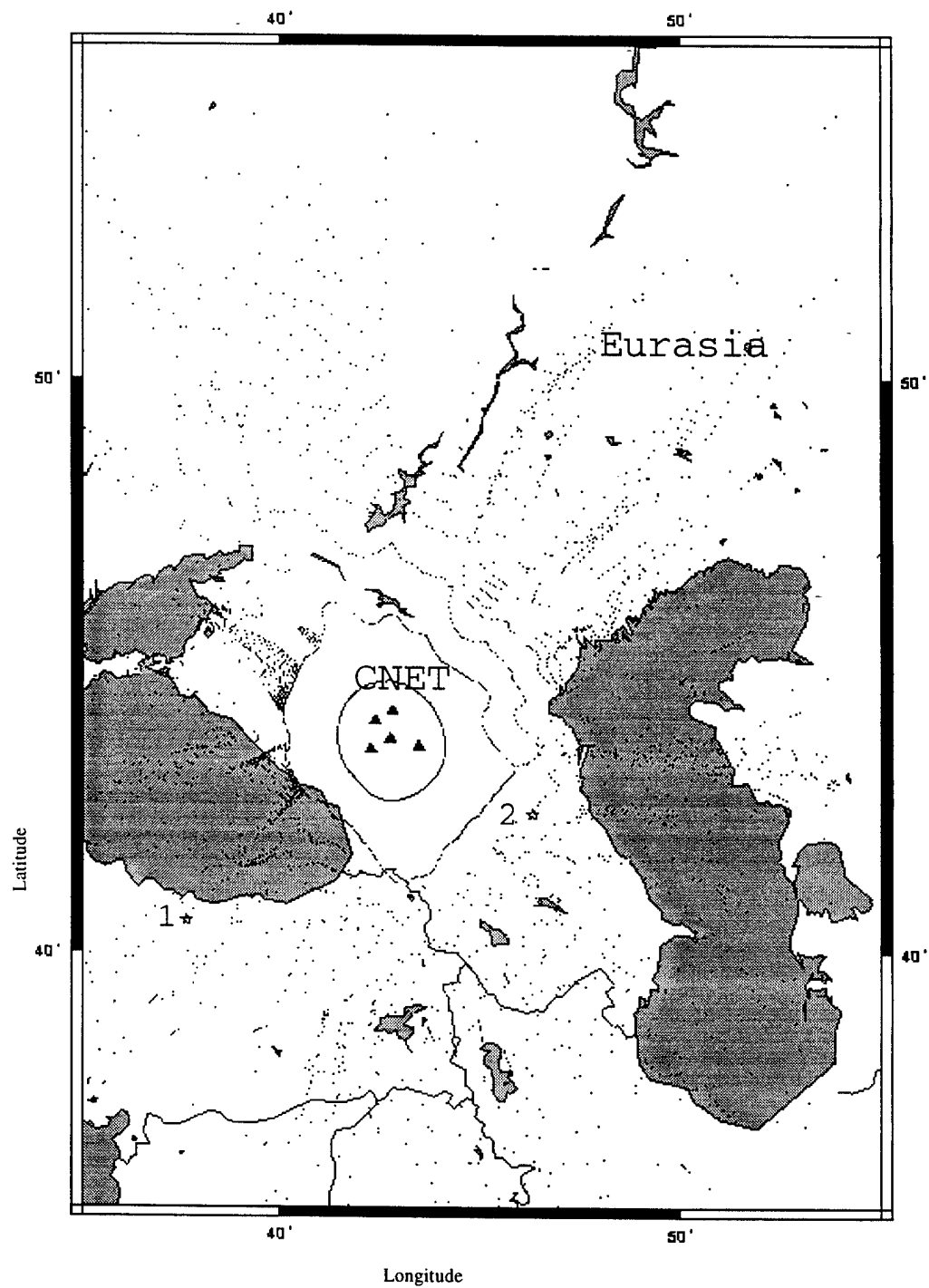
Figure 21d: Map view of ray bounce points from a regional model that includes the Fielding Moho and basin databases. Ray take-off dip angle is 60°, source depth is 15 km. Rays were shot at 1° azimuthal increments for 360°.
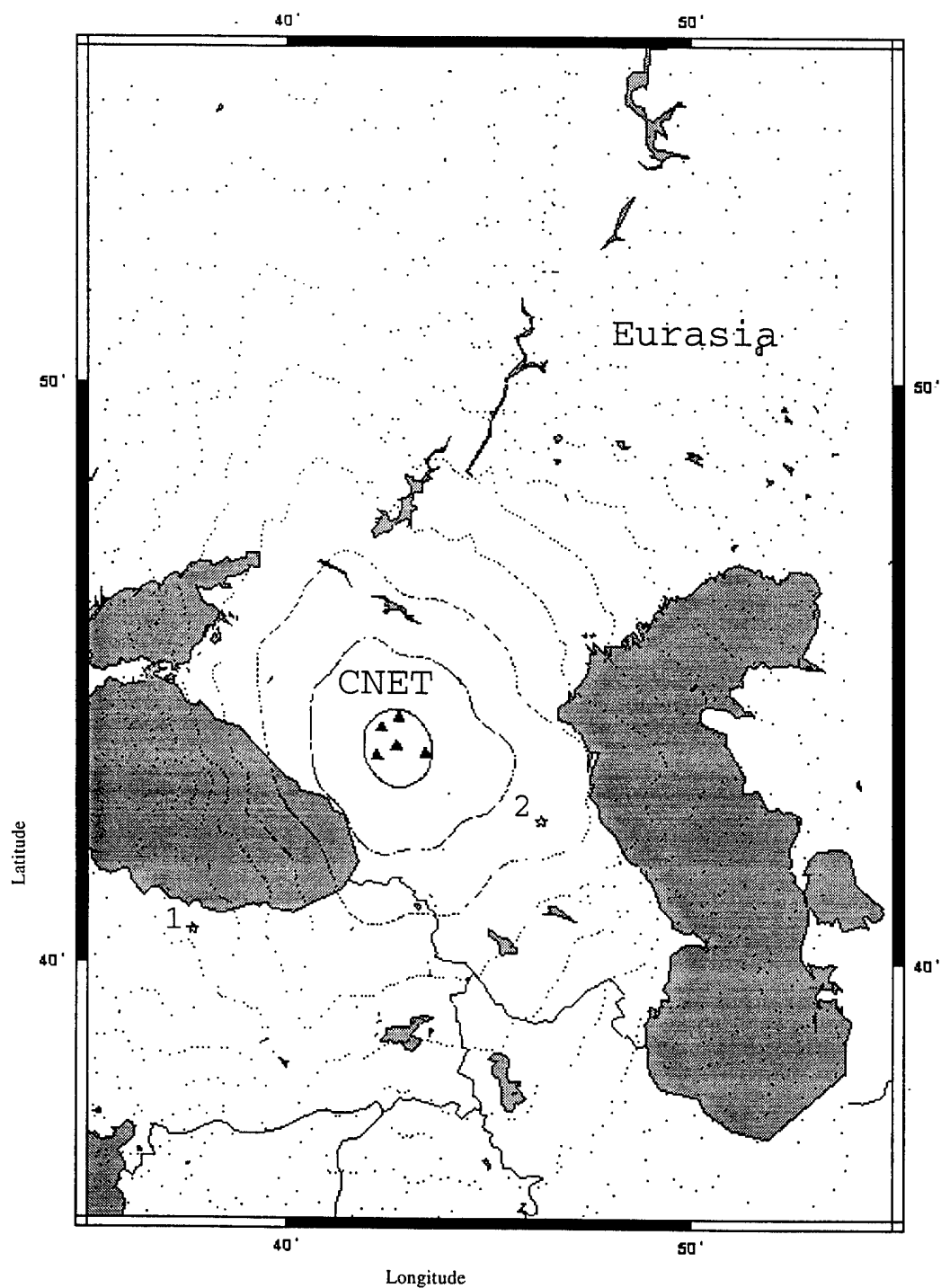
Figure 22a: Map view of ray bounce points from a regional model that includes the Fielding Moho database. Ray take-off dip angle is 70°, source depth is 1 km. Rays were shot at 1° azimuthal increments for 360°.

Figure 22b: Map view of ray bounce points from a regional model that includes the Fielding Moho and basin databases. Ray take-off dip angle is 70°, source depth is 1 km. Rays were shot at 1° azimuthal increments for 360°.

Figure 22c: Map view of ray bounce points from a regional model that includes the Fielding Moho database. Ray take-off dip angle is 70°, source depth is 15 km. Rays were shot at 1° azimuthal increments for 360°.
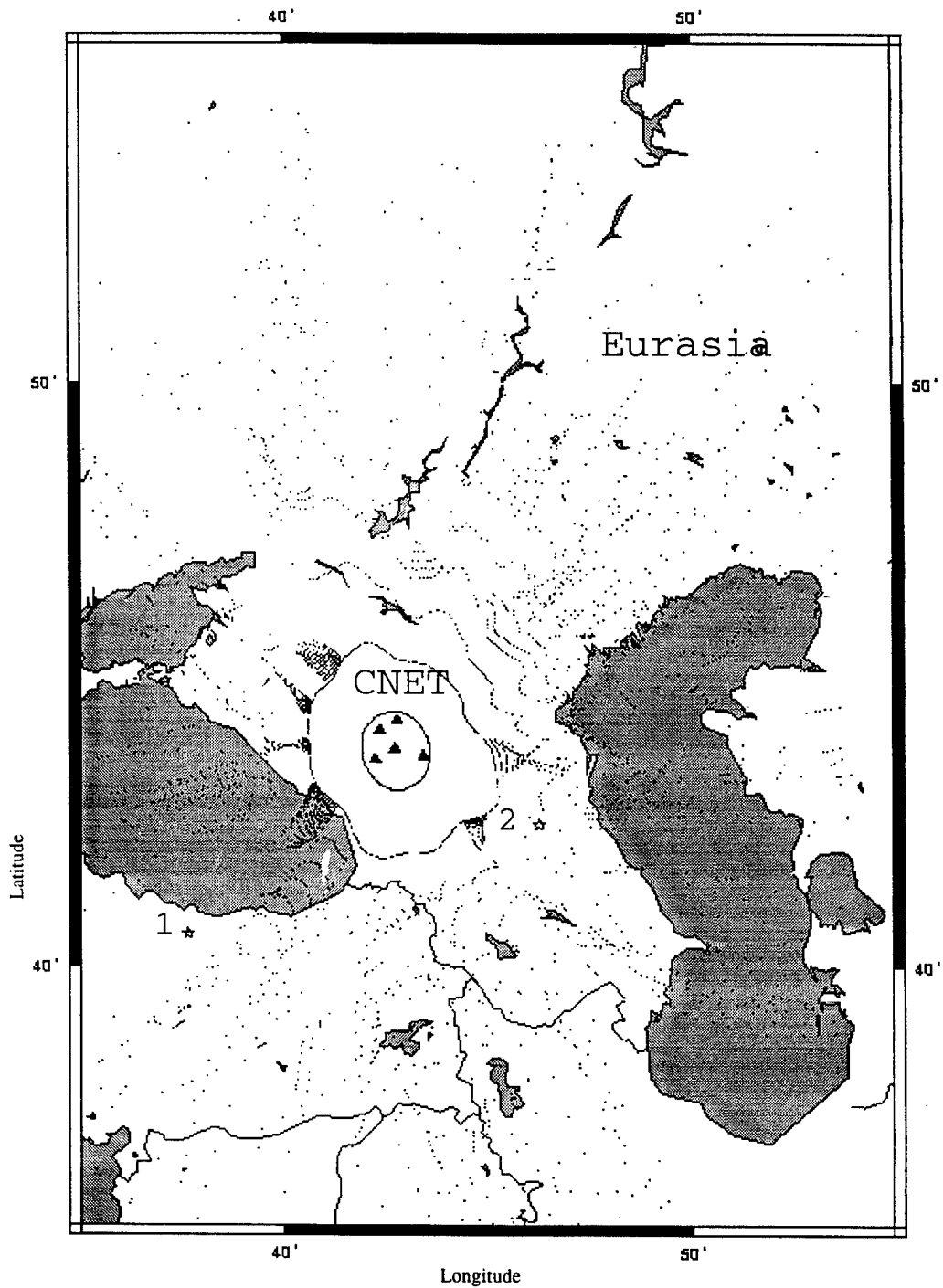
Figure 22d: Map view of ray bounce points from a regional model that includes the Fielding Moho and basin databases. Ray take-off dip angle is 70°, source depth is 15 km. Rays were shot at 1° azimuthal increments for 360°.
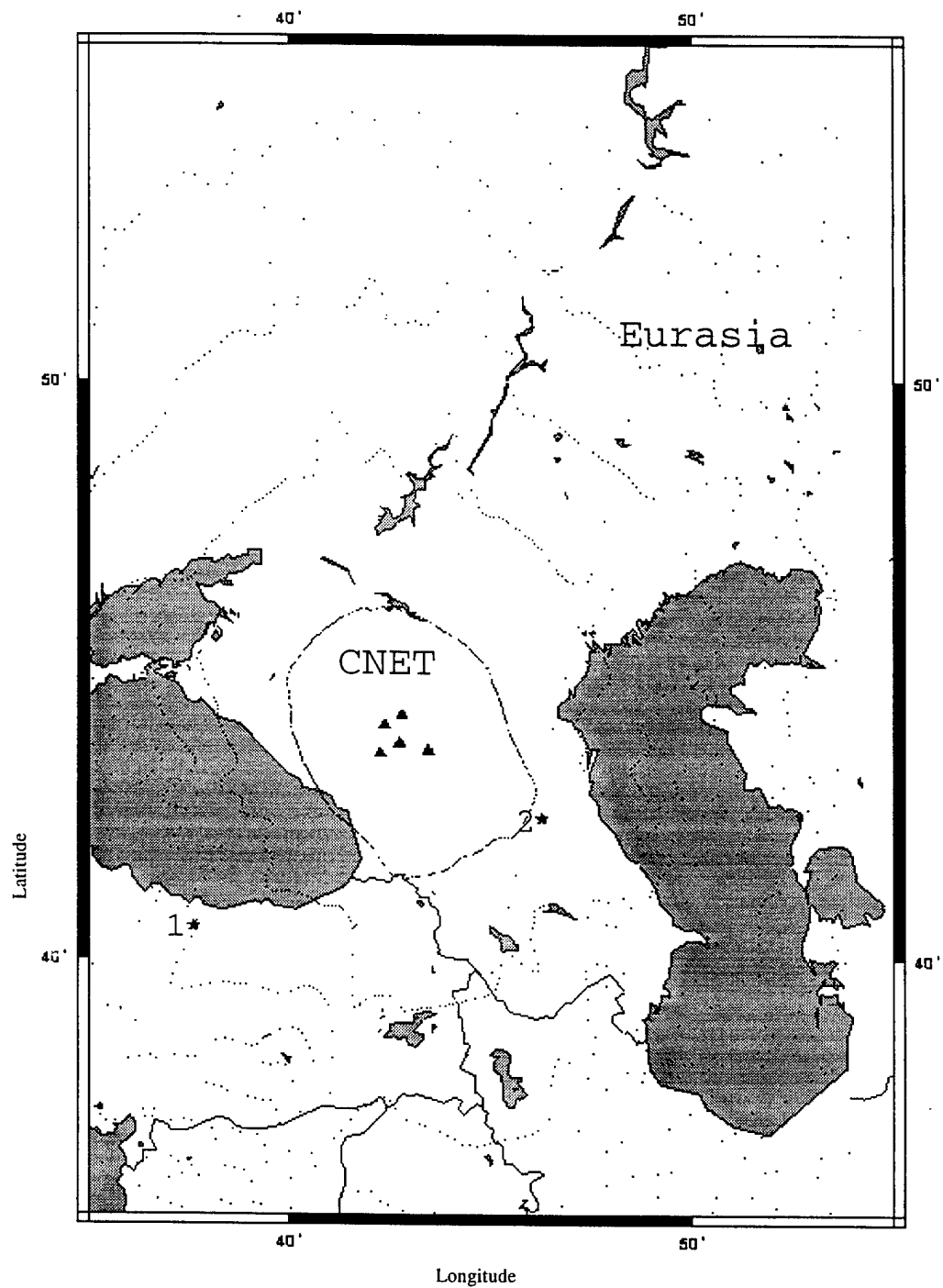
Figure 23a: Map view of ray bounce points from a regional model that includes the Fielding Moho database. Ray take-off dip angle is 80°, source depth is 1 km. Rays were shot at 1° azimuthal increments for 360°.
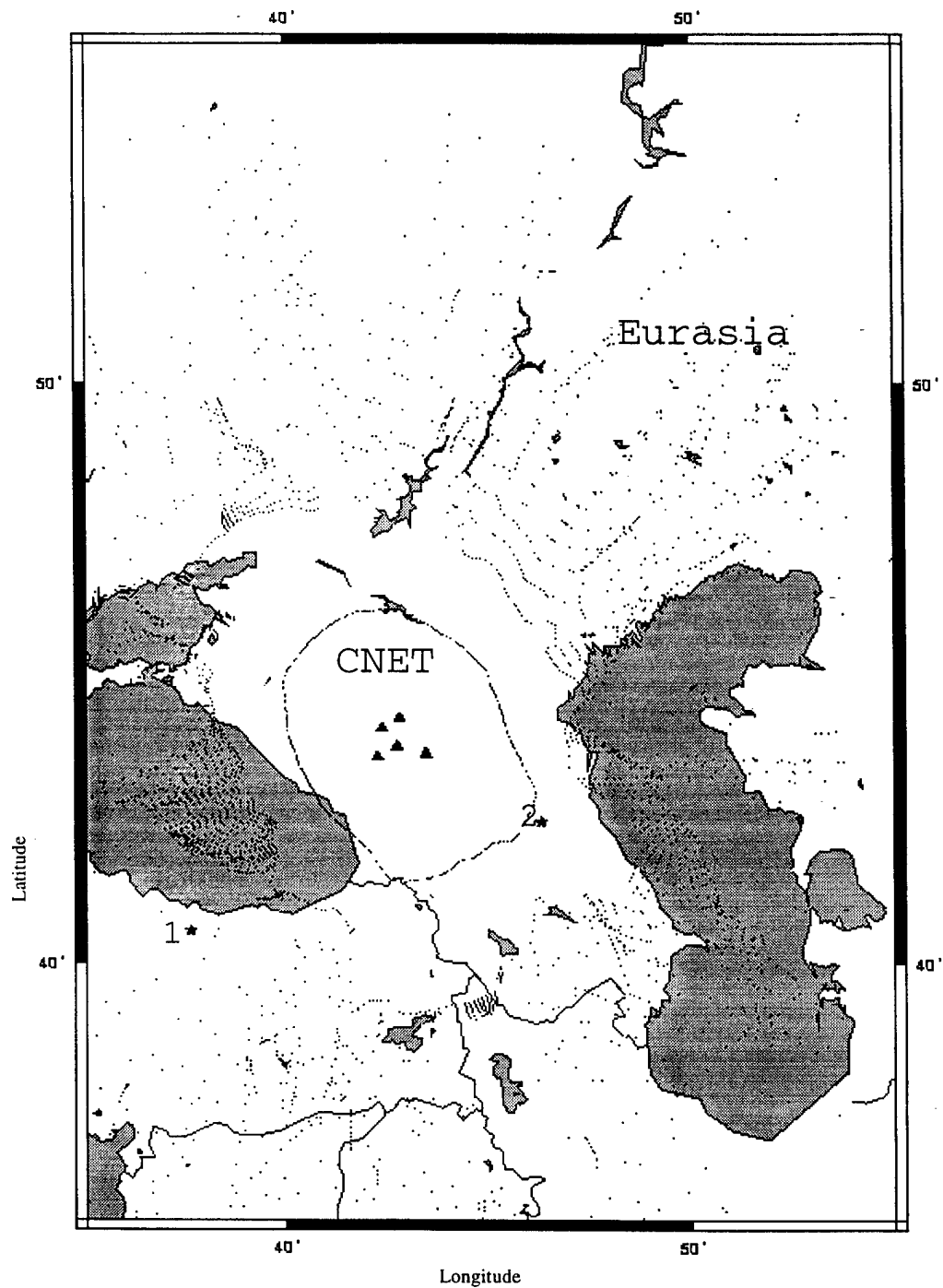
Figure 23b: Map view of ray bounce points from a regional model that includes the Fielding Moho and basin databases. Ray take-off dip angle is 80°, source depth is 1 km. Rays were shot at 1° azimuthal increments for 360°.
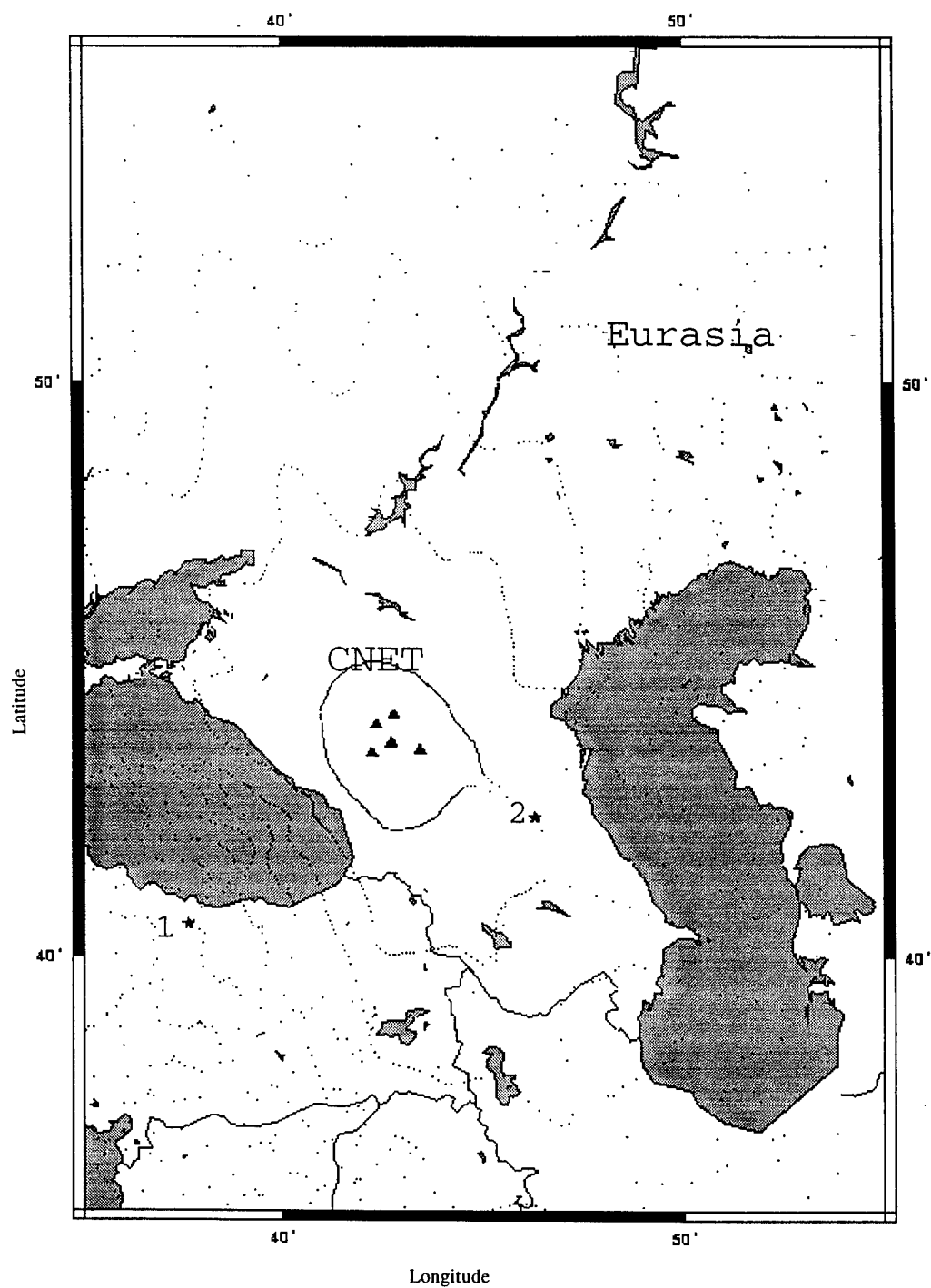
Figure 23c: Map view of ray bounce points from a regional model that includes the
Fielding Moho database. Ray take-off dip angle is 80°, source depth is 15 km.
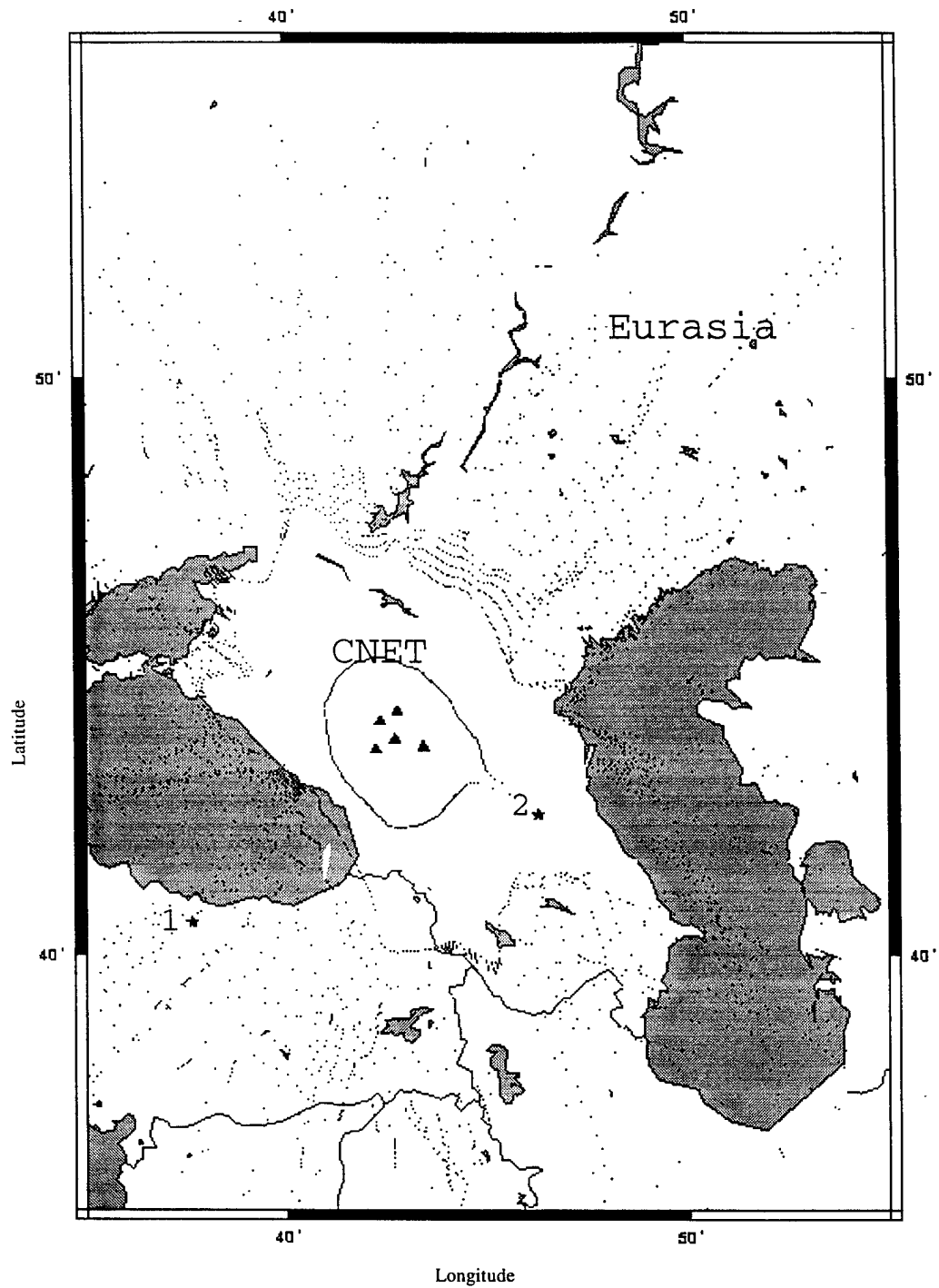Rays were shot at 1° azimuthal increments for 360°.

Figure 23d: Map view of ray bounce points from a regional model incorporated with Fielding Moho and basin databases. Ray take-off dip angle 80°, source depth 15km. Rays were shot at 1° azimuthal increments for 360°.

Figure 24a: Map view of ray bounce points from a regional model that includes the Fielding Moho database. Ray take-off dip angle is 60°, source depth is 1 km. Rays were shot at 1° azimuthal increments for 360°.

Figure 24b: Map view of ray bounce points from a regional model that includes the Fielding Moho and basin databases. Ray take-off dip angle is 60°, source depth is 1 km. Rays were shot at 1° azimuthal increments for 360°.
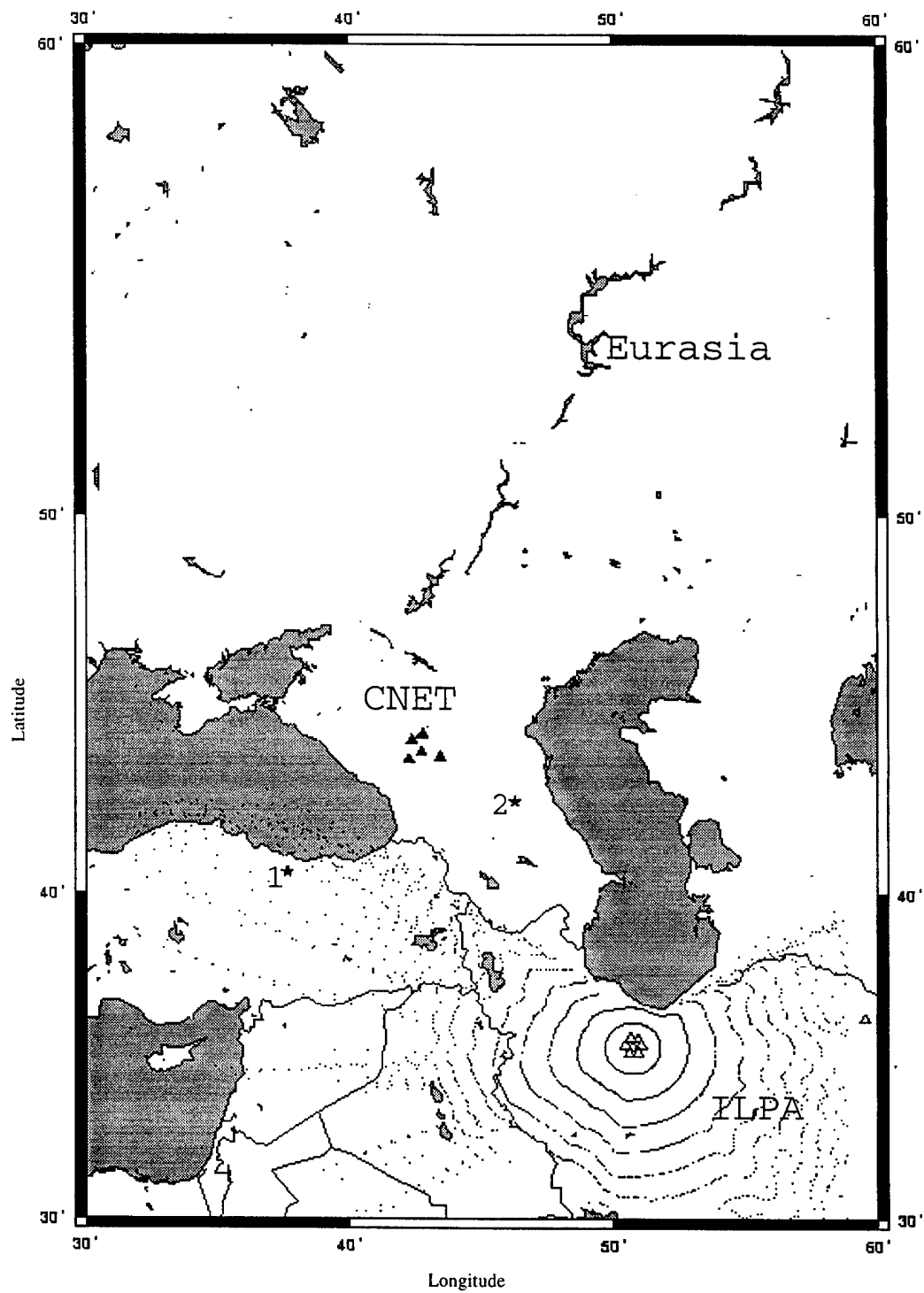
Figure 24c: Map view of ray bounce points from a regional model that includes the
Fielding Moho database. Ray take-off dip angle is 60°, source depth is 15 km.
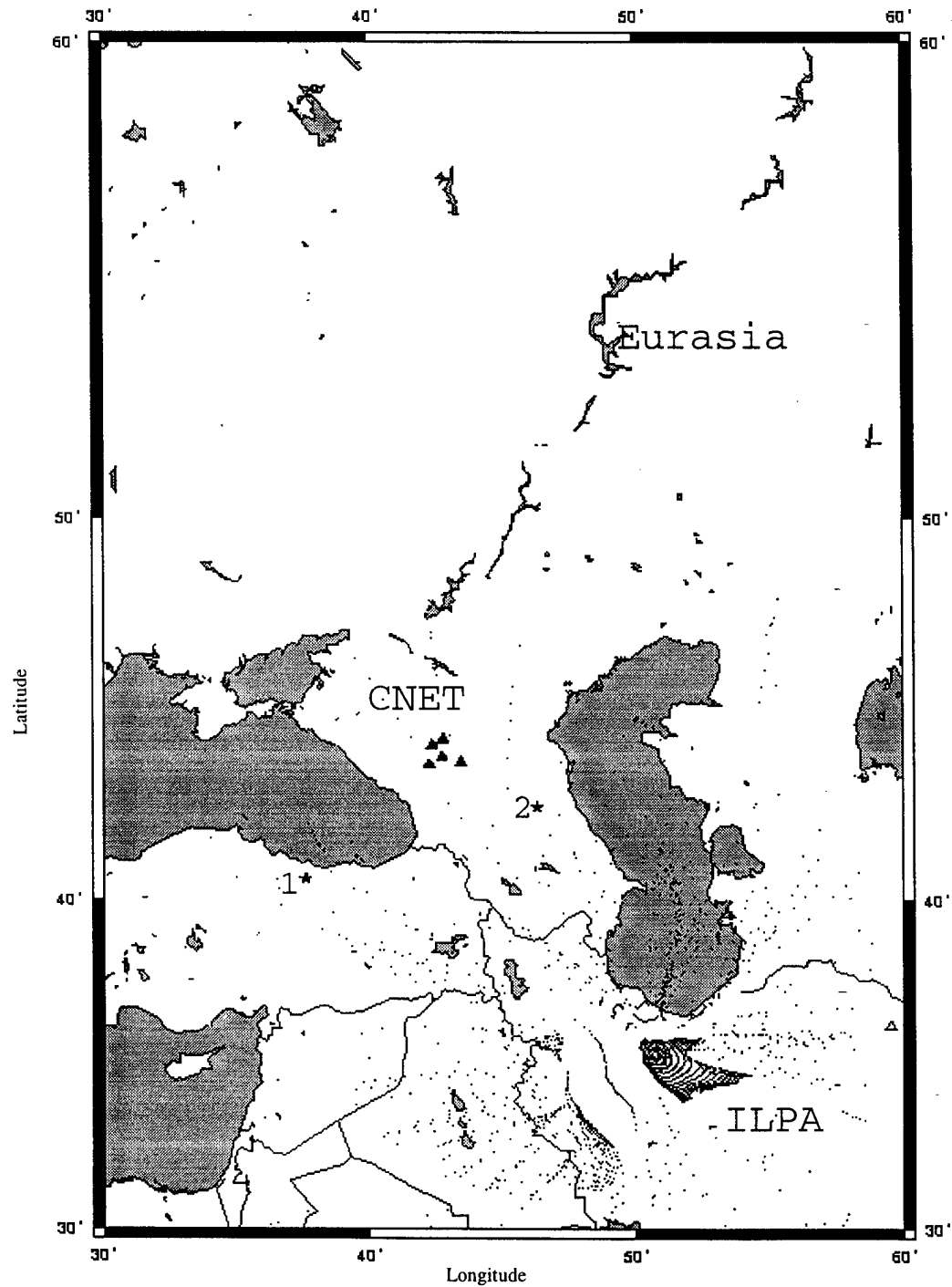Rays were shot at 1° azimuthal increments for 360°.

Figure 24d: Map view of ray bounce points froa m regional model that includes the Fielding Moho and basin databases. Ray take-off dip angle is 60°, source depth is 15 km. Rays were shot at 1° azimuthal increments for 360°.

Figure 25a: Map view of ray bounce points from a regional model that includes the Fielding Moho database. Ray take-off dip angle is 70°, source depth is 1 km. Rays were shot at 1° azimuthal increments for 360°.

Figure 25b: Map view of ray bounce points from a regional model that includes the Fielding Moho and basin databases. Ray take-off dip angle is 70°, source depth is 1 km. Rays were shot at 1° azimuthal increments for 360°.
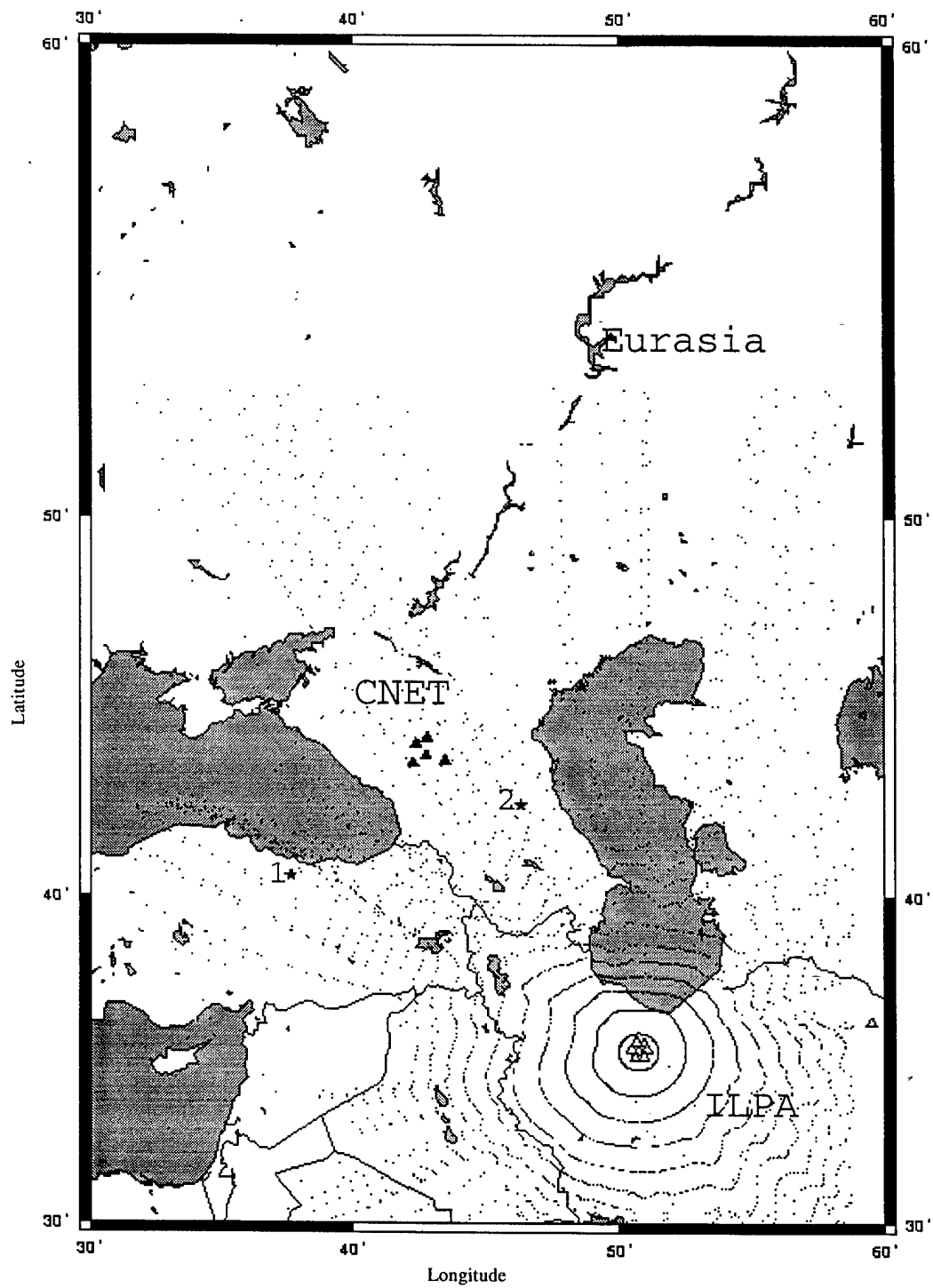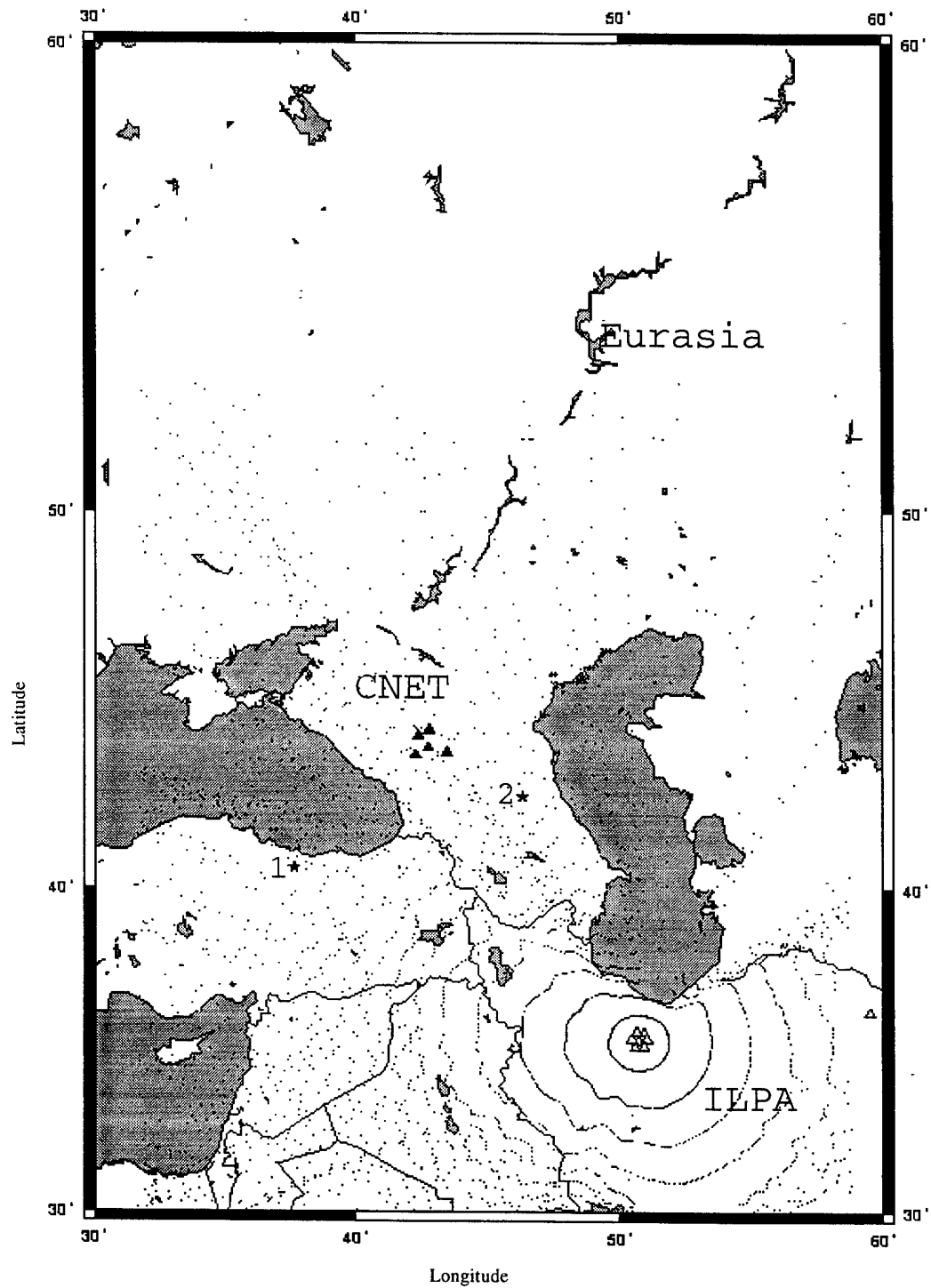
Figure 26c: Map view of ray bounce points from a regional model that includes the Fielding Moho database. Ray take-off dip angle is 70°, source depth is 15 km. Rays were shot at 1° azimuthal increments for 360°.
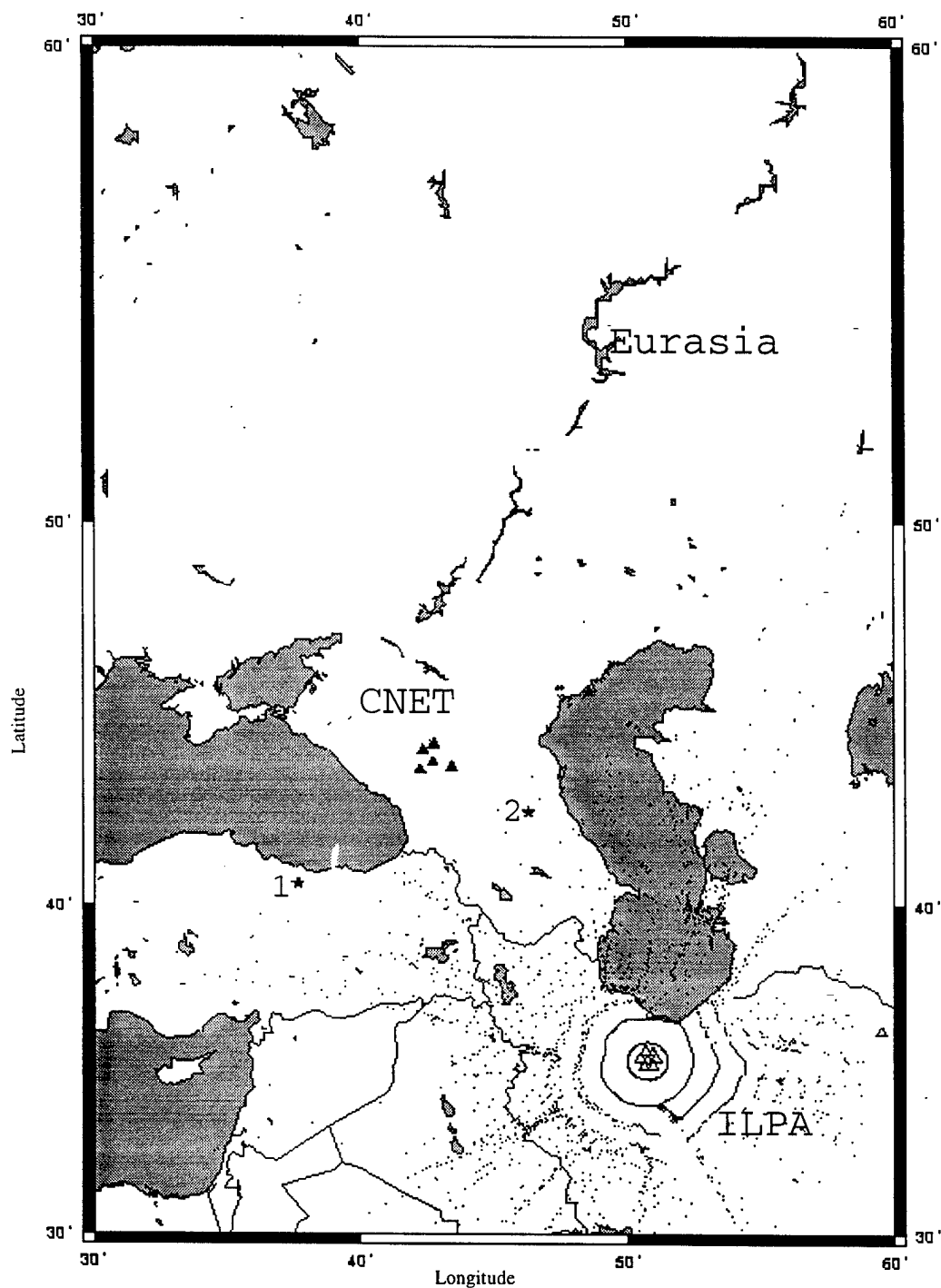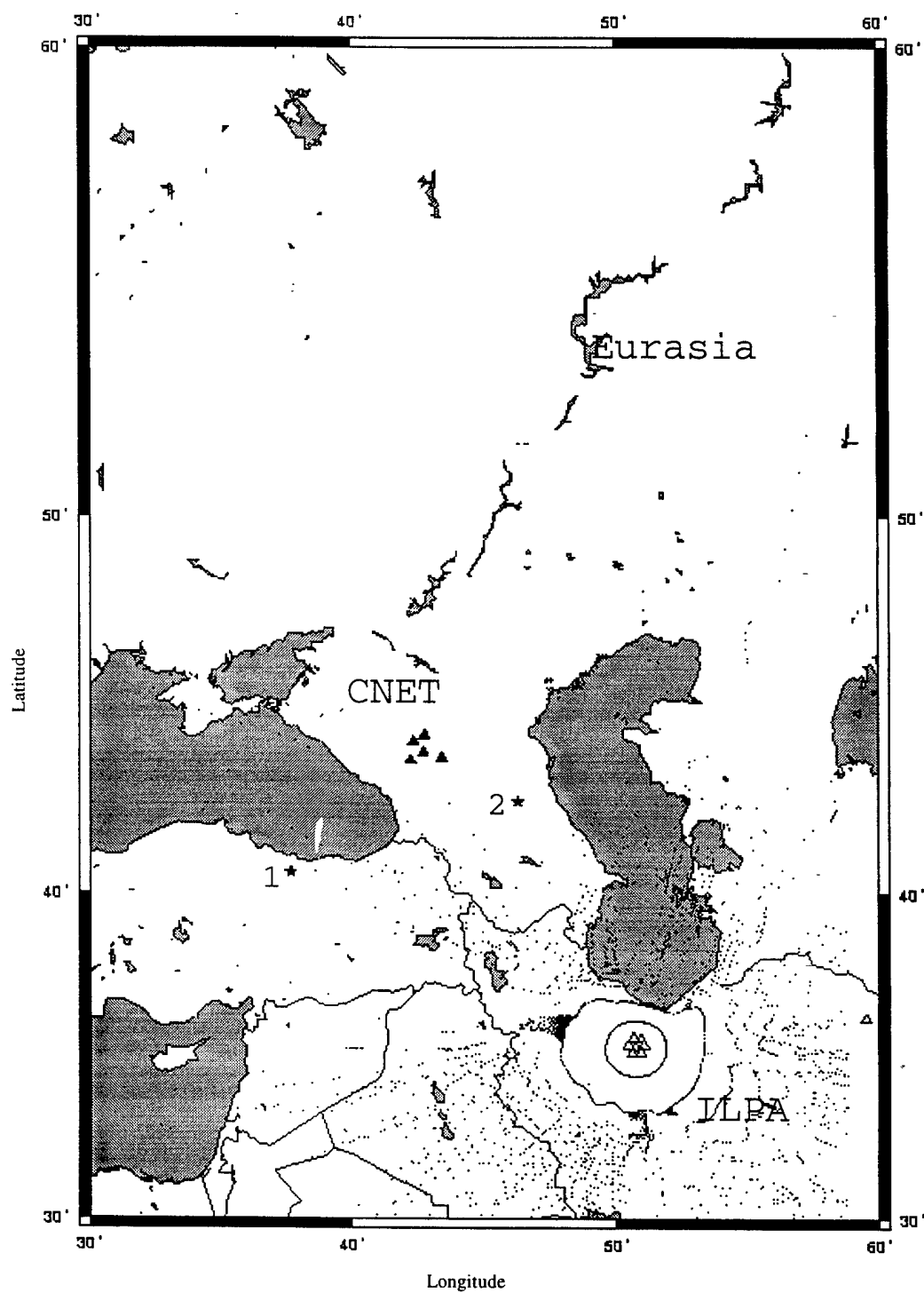
Figure 25d: Map view of ray bounce points from a regional model that includes the
Fielding Moho and basin databases. Ray take-off dip angle is 70°, source depth is 15 km.
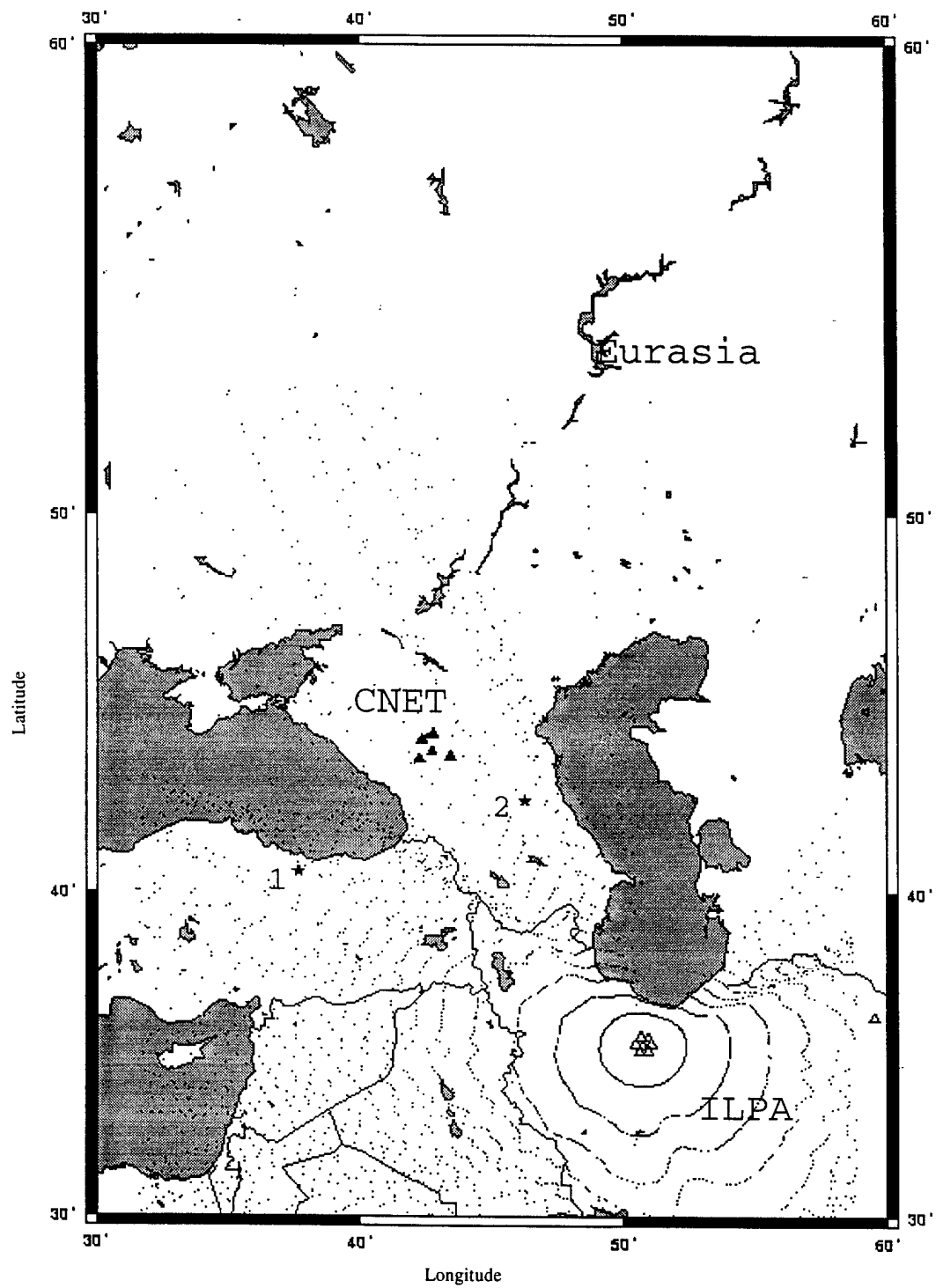Rays were shot at 1° azimuthal increments for 360°.
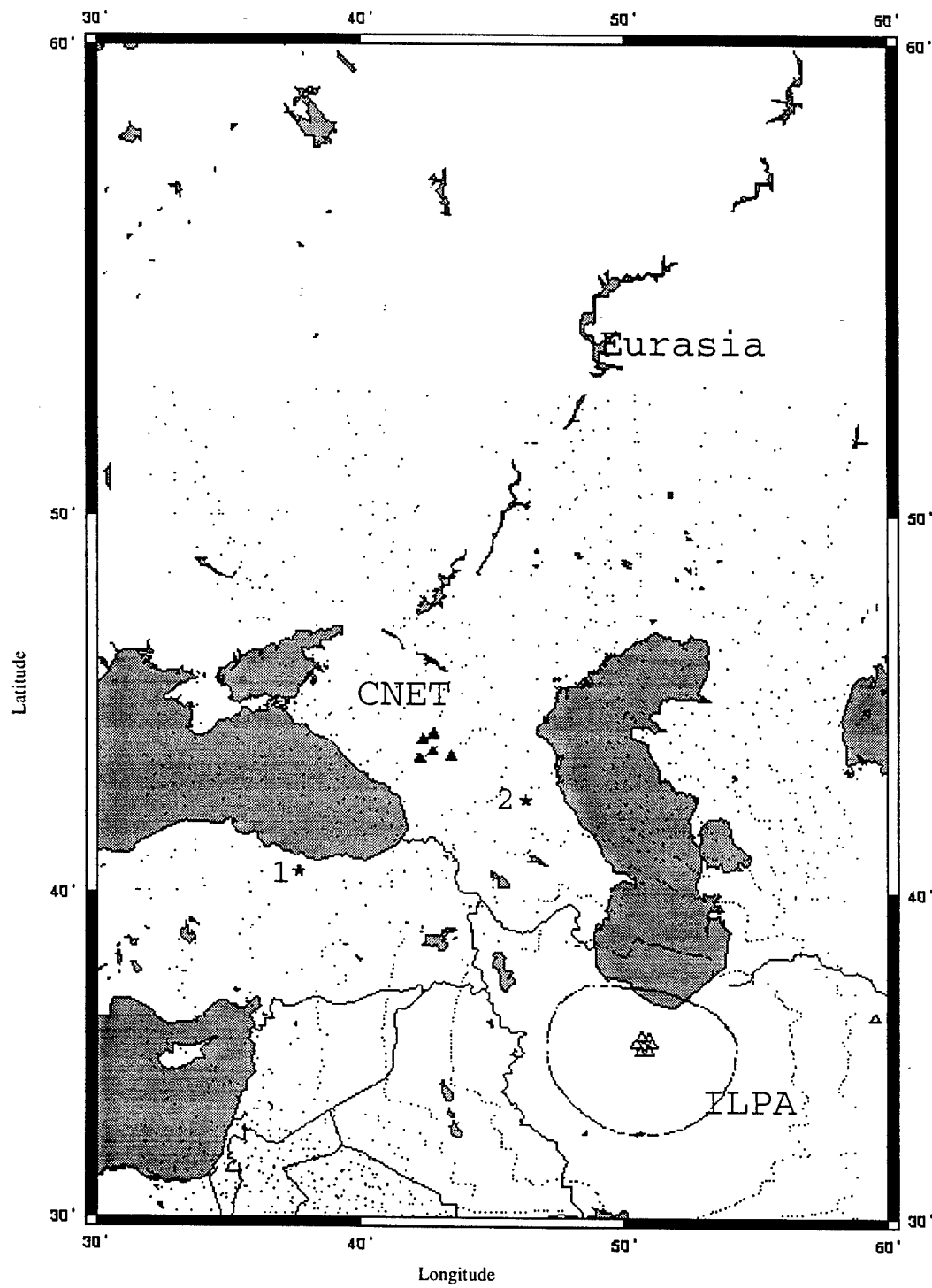
Figure 26a: Map view of ray bounce points from a regional model that includes the Fielding Moho database. Ray take-off dip angle is 80°, source depth is 1 km. Rays were shot at 1° azimuthal increments for 360°.
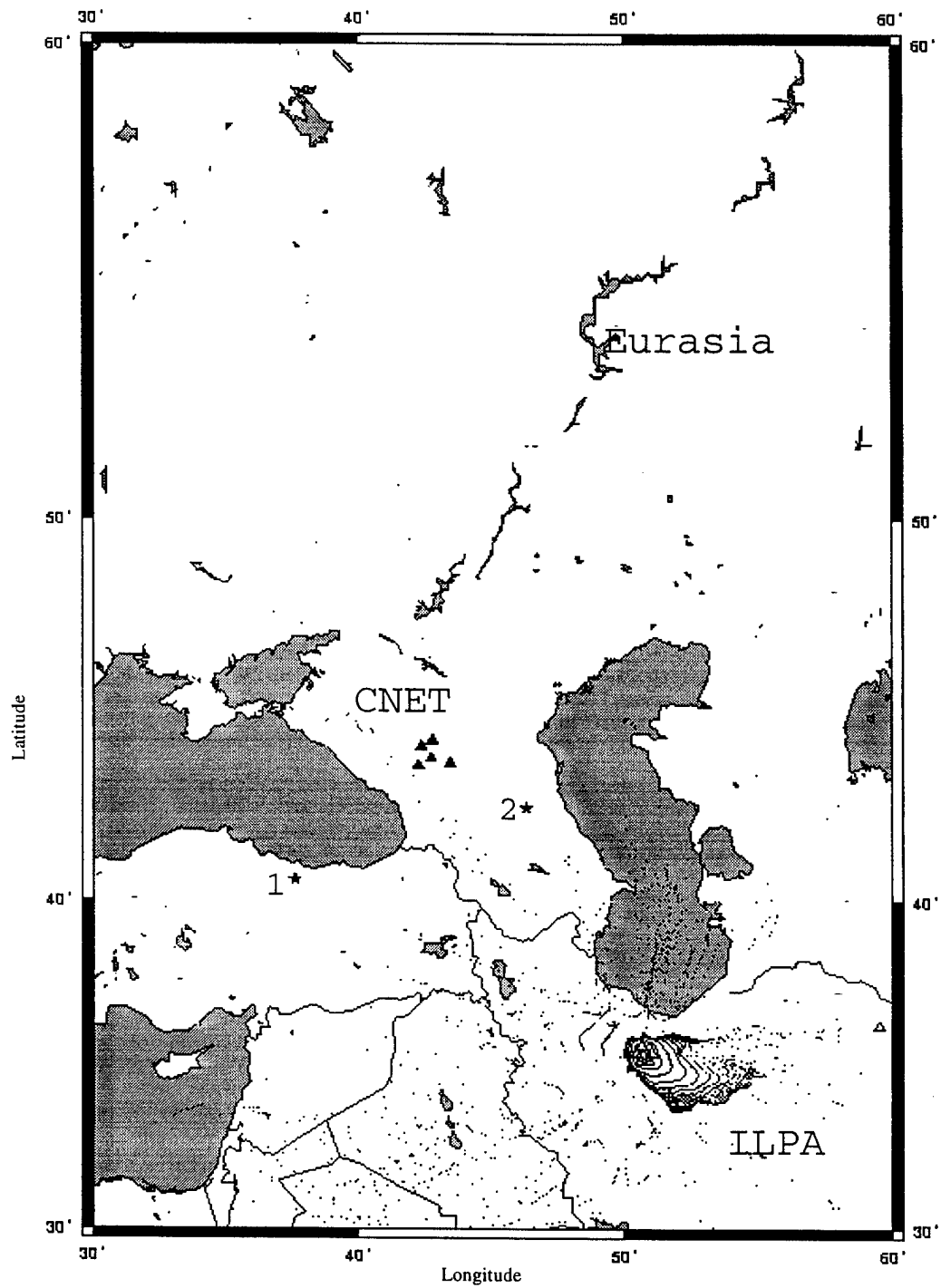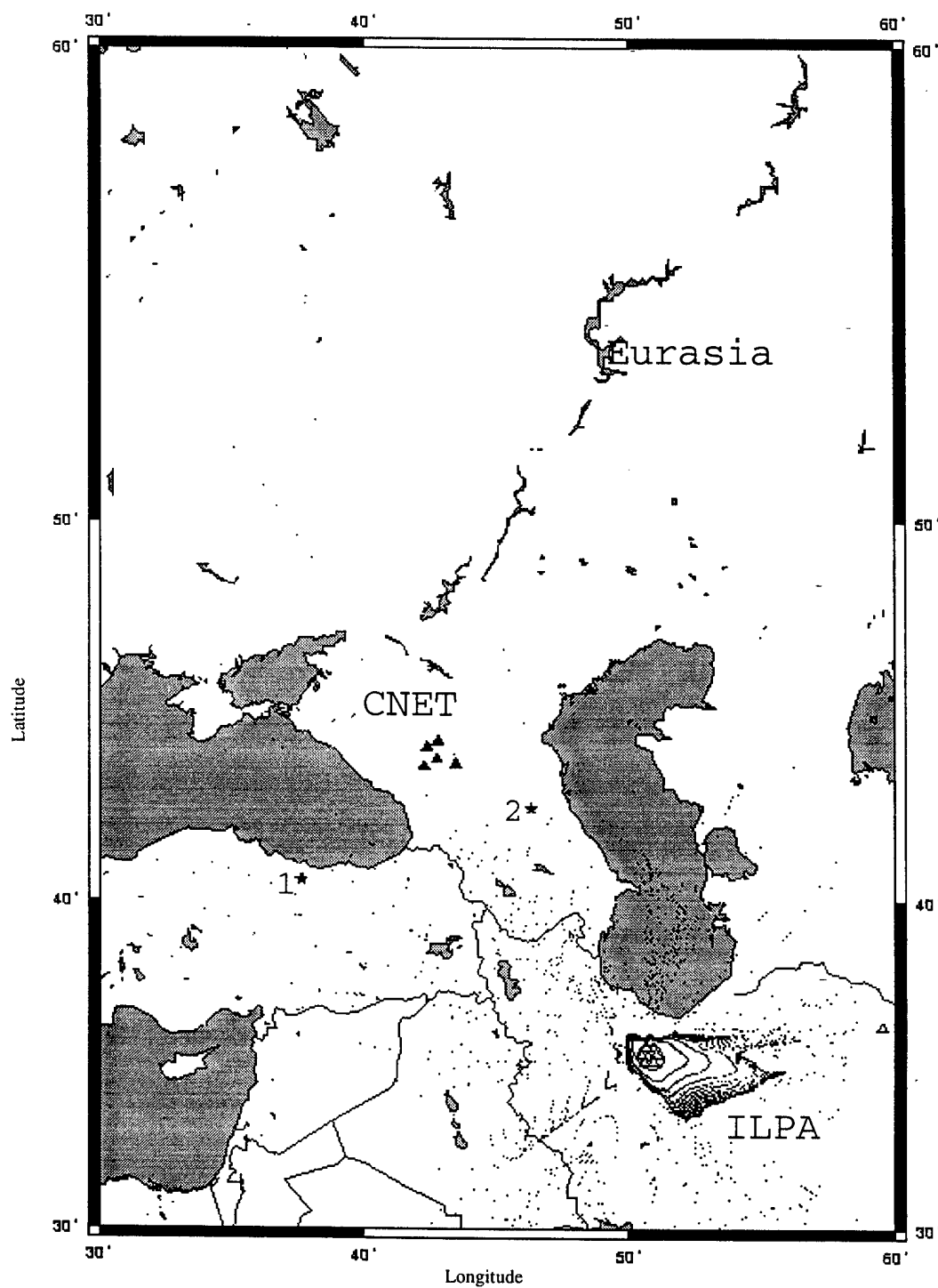
Figure 26b: Map view of ray bounce points from a regional model that includes the Fielding Moho and basin databases. Ray take-off dip angle is 80°, source depth is 1 km. Rays were shot at 1° azimuthal increments for 360°.

Figure 26c: Map view of ray bounce points from a regional model that includes the Fielding Moho database. Ray take off-dip angle is 80°, source depth is 15 km. Rays were shot at 1° azimuthal increments for 360°.

Figure 26d: Map view of ray bounce points from a regional model that includes the Fielding Moho and basin databases. Ray take-off dip angle is 80°, source depth is 15 km. Rays were shot at 1° azimuthal increments for 360°.
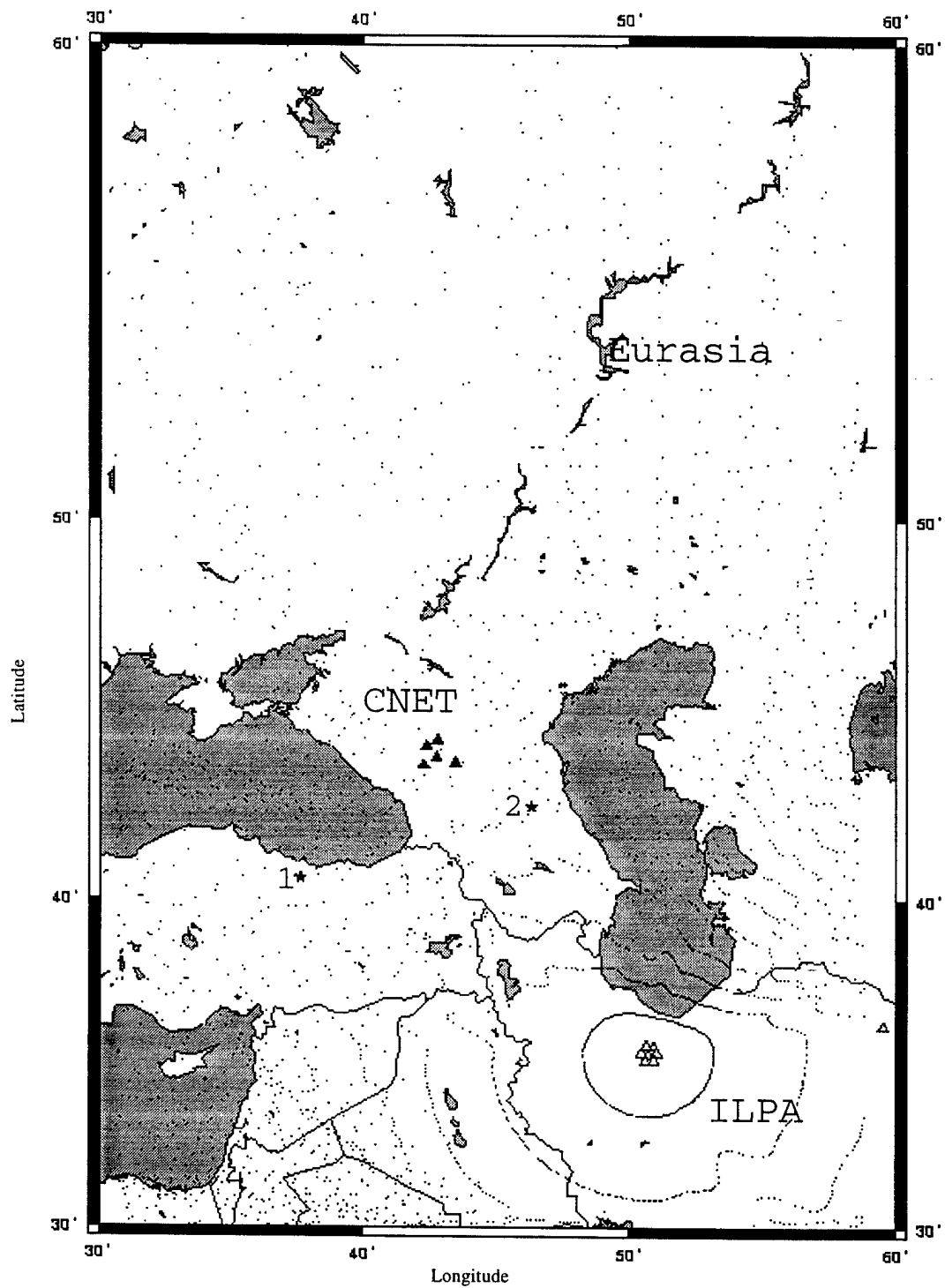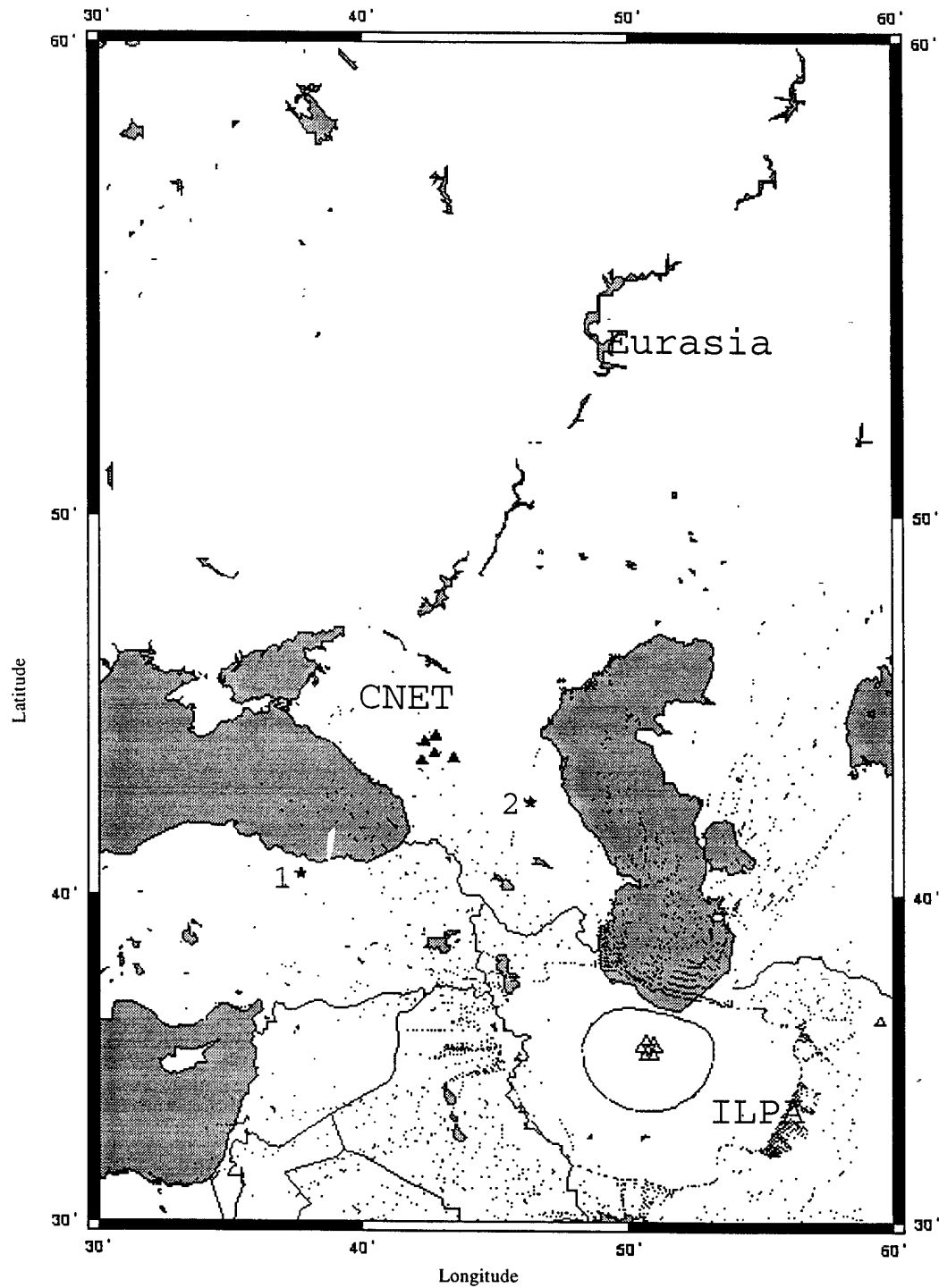
3 Effects of Small Scale Structure

3.1 Previous work and limitations

Ray models of Lg phase are useful in qualitatively predicting gross features of blockage by large scale crustal transitions, but the effects of smaller scale heterogeneity are more difficult to numerically model. The most important effects of small scale heterogeneity can still be accurately included in modeling by the Rayleigh-Born approximation to scattering when the scale length of the heterogeneity is much smaller than the wavelength. Realistic waveform complexity, however, is difficult to achieve in a ray method without fine scale layering and large numbers of scatterers. The coda of Lg, including equalization of Lg energy on all components of motion, has been attributed to back-scattering of seismic energy off lateral heterogeneities in the crust (Aki and Chouet, 1975). The heterogeneities that contribute to the scattered field are contained within two ellipses (figure 27a) that have foci at source and receiver and have a major axes equal to vt and v(t+dt), where v is the velocity of the wave field and t is time. In this section, the effects of fine scale heterogeneity in plane-layered, laterally homogeneous structures, are modeled by the locked mode method (Cormier et al. 1991, Harvey 1981) together with the Rayleigh-Born approximation.

The Rayleigh-Born approximation was first used in the 2-D surface wave problem by Kennett (1972). Snieder (1986) developed the theory for 3-D heterogeneities by using a dyadic representation of the far-field Green's function in a laterally homogeneous medium. Wang and Hermann (1988) used Born scattering to investigate surface and body waves in a layered medium. Wang and Hermann's study (1988) accounted for mode conversion, wave type conversion, finite scatterer distribution and attenuation from scattering as well as

from intrinsic anelasticity. Wang and Hermann's study established the importance of mode conversion and found that Rayleigh to Love wave scattering may be small except at close distances. Due to the computational enormity of the problem, their study limited the number of modes used in conversion to ten. In the study reported here, we use mode summation similar to that of Wang and Hermann (1988) but implement Wu's derivation for Rayleigh scattering in terms of equivalent sources having different force and force moments corresponding to perturbations in density and elastic moduli. This enables computation of the complete mode interaction without the expense of computing individual mode to mode scattering coefficients. The computation of modes at any given frequency is thereby reduced from m^2 to $2m$, where m is the number of modes, thus making the computation of the all mode interactions a tractable problem for any frequency band.

3.2 Modeling method

We begin by following Wu and Aki's (1985) adaptation of the Gubernatis et al. (1977a, 1977b) formulation of the single-scattering problem. Given an arbitrary heterogeneity with variations in parameter's

$$\lambda(x) = \lambda_0 + \delta\lambda(x), \qquad \qquad \delta\lambda << \lambda_0$$
$$\mu(x) = \mu_0 + \delta\mu(x), \qquad \qquad \delta\mu << \mu_0$$
$$\rho(x) = \rho_0 + \delta\rho(x), \qquad \text{where} \qquad \delta\rho << \rho_0$$

and is located in a homogeneous medium with parameters λ_0, μ_0 and ρ_0. The displacement field U can be written as the sum of the direct wave

$$U = U^0 + U^1$$

Scatterers are treated as equivalent sources using the Born approximation (Haddon and Cleary, 1974; Gubernatis et al., 1977 a, b; Aki and Richards, 1981; Wu and Aki, 1985). For Rayleigh scattering, in which the wavelength is much larger than the inclusion, the

scattered field can be equated to a point source consisting of a single force proportional to the density contrast and a moment tensor proportional to the contrasts in elastic moduli . The equivalent point force at a scattering heterogeneity can be written as

$$F_i = \int_v Q_i dV \approx \omega^2 \overline{\delta\rho} V U_i^0 (\vec{x}_0)$$

(3.1)

and the moment tensor can be written as

$$M_{ik} = \int_v Q_i x_k dV(\vec{x})$$

$$M_{ik} = -\delta_{ik} \overline{\delta\lambda} V \nabla \cdot U^0(x_0) - \overline{\delta\mu} V \left[\frac{\partial U_i^0(\vec{x}_0)}{\partial x_k} + \frac{\partial U_k^0(\vec{x}_0)}{\partial x_i} \right]$$

(3.2)

where Q_i is the equivalent body force, V is the volume of the inclusion, $\overline{\delta\lambda}, \overline{\delta\mu},$ and $\overline{\delta\rho}$ are the average perturbations in Lame's parameters and density, and δ_{ij} is the Kronecker delta. It may be noted that the $\delta\lambda V$ in equation 3.1 has only diagonal components, all equal, which corresponds to an explosion. The moment tensor due to $\delta\mu V$ is a symmetric tensor that may have both diagonal and non-diagonal elements. The diagonal elements of $\delta\mu V$ correspond to on-line force couples, and the off diagonal element pairs correspond to torsion double couples.

All displacements appearing in the equivalent source representations are calculated as a sum of locked Rayleigh and Love modes, using a modified version of the locked mode code of Harvey (1981). The displacement at the inclusion is calculated by summing over modes at each frequency,

$$U^0(k,z,\omega) = \sum_{k=1}^{n\,modes} U^0(k,z,\omega)$$

,

where k is wavenumber, z is depth and ω is angular frequency. The equivalent point force is then computed for each inclusion and reradiated towards the receiver. This entails taking

the horizontal and vertical derivatives of the stress displacement vector to compute the force

moment tensor of the equivalent point force vector. The scattered far field (Aki and

Richards, 1981; Wu, 1984) is then calculated as

$$U_i^1 = F_j * G_{ij} + M_{jk} * G_{ij,k} \quad,$$

with F the point force, M the equivalent moment and G, the Green's function response.

This convolution is performed within the mode summation program, by looping over the

modes again and computing the response due to the point force and moment tensor. The

original program allows for sources and receivers to be located in arbitrarily in a Cartesian

coordinate system and rotates this coordinate system into the source-receiver paths so that

motion can be partitioned into a sum of either pure Rayleigh and or pure Love modes.

These coordinate rotations are performed for both the path segment from the source to

scatterer and the path segment from the scatterer to receiver. Figure 28 displays a map

view of the geometry for the source-scatterer-receiver used in computations.

In all calculations, a step function time dependence is assumed for the displacement in the

near-field, corresponding to a delta function time dependence for both P and S body waves

observed in the far-field. This is assumed to be a good approximation for earthquakes of

body wave magnitude 2.5 and smaller, having far-field P corner frequencies higher than 2

Hz.

3.3 Results of computational experiments

3.3.1 A single inclusion

To determine where in the wave guide it is necessary to know the detailed fine scale

structure that affects Lg propagation, a simple scenario is tested. The scattered field is

calculated for a single inclusion for a source-receiver pair that are located 17.75 km apart. The structural model used is for the Pinion Flats region in California (Scott et al., 1994). This region is chosen due to a well constrained velocity model from prior studies as well as the arrays' proximity to a large regional fault that may have scattering effects. The structure from the region used to calculate the mode catalogue is in table 2. While the range is too close for a true Lg phase to develop, the coda following the S arrival that is the result from lateral heterogeneities has the same characteristics as coda observed at greater distances. The scattering bodies are assumed buried in this study. This simplifies the algorithm and avoids more computations of perturbations at the surface boundary. An impulsive explosion source in a cavity is used to illustrate the conversion of modes and generation of Lg. An explosive source in a homogeneous medium will not generate energy on the transverse component, so any energy observed here on the transverse component is the result of mode conversion through scattering by the inclusion.

The volume of the inclusion used in this study is 5 km^3 . This corresponds to a sphere of radius of approximately 1.59 km. For a frequency of 3 Hz, this is slightly larger than the condition that provides for validity of the Rayleigh approximation:

$$k_{max} R = \frac{\omega R}{c_{min}} \ll 1,$$

where c_{min} denotes the minimum velocity and k_{max} denotes the corresponding wavenumber, ω is angular frequency, and R is the radius of the volume. Such a violation in the volume size may produce amplitude errors on the order of 30%, but the fundamental scattering characteristics will valid. The variation in Lame's parameters, μ and λ, used for the heterogeneity is -8% and density, ρ, is -5%. These variations are used to represent realistic variation observed in crustal seismic velocities and densities.

The inclusion is placed at a constant depth of 2 km and then moved away from the source in 2 km increments at a 45 degree azimuth. The geometry for this is illustrated in figure 29. The inclusion is then held at a constant range of 2 km and 45 degrees and it is placed at depth in 2 degree increments. The same procedure is used to test heterogeneities at distances relative to the receiver. Synthetics of the scattered component are then computed with the Born-mode method and plotted for each location. Figures (30-33) illustrate the synthetics that resulted from this test.

The synthetics of the scattered component for a near-source scatterer at constant depth show that the amplitude in the group velocity window 2.75-3.5 km/s rapidly decreases with distance as the inclusion is moved out at 45 degrees from the source in 2 km increments (figure 30). The transverse energy (figure 30b) that is generated is on the same order as the scattered components generated on the radial and vertical components (figures 30a, c). The synthetics generated from scatterers at a constant range of 2 km and for depths to 10 km in increments of 2 km are plotted in figure 31. The energy decay on all components appears much faster with depth than previously observed with increasing range. This is a little misleading due to the fact that the source-scatterer-receiver distance increases more rapidly when the inclusion is moved at the same interval in the z direction as in the horizontal direction. The synthetic seismogram that is due to the scattered field illustrates how the scattered wave field amplitude varies with inclusion distance and depth from the source. The inclusions closest to the source contribute most to the amplitude of the scattered wave field. This is noted in both the horizontal range and the vertical range.

The synthetics from models where the heterogeneity is placed near the receiver yield very similar results. In both the increasing horizontal range and depth cases (figures 32-33), those heterogeneities closest to the receiver yield the highest amplitude scattered wave. It is noted that transverse energy is observed for all placements of the heterogeneity.

68

The components due to the near-source and near-receiver scattered contributions are summed with the direct arrivals (figure 35a) and compared to the direct arrivals. It is noted that some transverse energy is generated, but not to the same extent of the radial or vertical component. The vertical and radial components indicate attenuation due to deconstructive interference. The length of the coda or wave train that follows is lengthened past 10 seconds. This is better illustrated in the envelope of the traces (figure 35b). The envelope function is defined as

$$env(t) = \sqrt{x^2(t) + y^2(t)}$$

where x(t) is the original signal x(t) and y(t) is the Hilbert transform. The envelope function is a useful way to observe decay on complex signals such as Lg coda. The envelope of the direct arrival clearly has a shorter duration and decays much faster than the envelopes that include all of the scattered components. The coda in this case was significantly increased with the addition of only eighteen point scatterers, thus creating a more complex looking waveform. In this case the majority of the contribution came from shallow scatterers (2 km) and whose range was increased horizontally. The contribution of the individual inclusions rapidly drops with increasing depth, as can be seen when comparing maximum envelope amplitudes for the Lg group velocity window 3 3.5 km /s (figure 34).

3.3.2 Multiple inclusions

The crust of the earth is thought to be highly heterogeneous on all scales, therefore, in this section, clusters of inclusions will be modeled at different ranges and depths to determine to what extent the fine scale structure needs be known accurately to model Lg. Both shallow earthquakes and explosions (1 km depth) are used as sources to generate complete

synthetic seismograms and to examine Lg generation in an effort to understand what effect the source type has on scattering. To further examine range and depth dependence, inclusions are put arbitrarily near the source, near the receiver, and at mid-range spatial distributions. Synthetics are generated in models where the heterogeneities are at shallow crustal depths of 3 and 5 km and deeper crustal depths 25 to 27 km for a source-receiver distance of 225 km apart (figure 36). The inclusions have variations in Lame's parameters μ and λ -9% and density, ρ, -3%, respectively. The volume of the inclusion is 25 km^3. The parameters are chosen on the upper limit of what is expected in the crust. Scattering scales linearly with the volume of the of the inclusions.

The first source type considered is an earthquake source. Source parameters are a step function time dependence of near-field displacement a strike, dip, and rake of 61°, 70°, 14° respectively, appropriate for an earthquake typical for the Caucasus region. The radial component synthetics due to the earthquake source (figure 37) show the contribution from shallow scatterers (in gray) are more than twice the size of the contribution from deeper scatterers, except for the mid-range case. Near-source shallow scattering, however, greatly exceeds mid-range shallow or deep scattering and contributes most in amplitude to the final synthetic (figure 38a-b). The duration of the Lg is extended as scattered energy arrives later in the Lg group velocity window when compared to the direct arrival. It should be noted that the amplitudes of the synthetics due to scattering are plotted relative to each other and not relative to the direct wave, as the parameters of the inclusions may be changed to produce greater or smaller scattering amplitudes relative to the direct wave. The direct wave is plotted for shape and duration reference only. In the case of the transverse component due to the earthquake source, almost all of the scattered energy that is seen is due to shallow near-source and near-receiver components with little or none due to the mid-range scattering (figure 39). The scattered energy is also seen to be peaking later in the Lg window compared to the Lg in the direct wave. The envelope of the transverse component

(figure 40b) due to shallow scattering is lengthened considerably and extends throughout the Lg group velocity window. The vertical component due to the earthquake source does contain considerable energy due to mid-range scattering (figure 41). Near-source shallow scattering, however, is still the dominant contribution to the synthetic, adding most of the energy later in the Lg group velocity window. This is due to the large amplitude fundamental mode Rayleigh wave that is scattered near the source or receiver before rapidly attenuating. In figure 42 a-b the direct vertical component synthetic is plotted along with the synthetics of the combined amplitudes due to shallow scattering and due to deep scattering. The envelope of the vertical synthetics show that the shallow scattering contributes energy that peaks at 70 seconds and tails off near the end of the group velocity window.

The same scattering geometry is used to compute synthetic seismograms for the scattered energy due to an explosion source in a cavity of .1 km^3. The radial components of the direct and scattered arrivals are plotted in figure 42-44. The shallow near-source scattering is considerably larger than the other synthetics. Shallow, near-receiver scattering also contributes to the waveform, but inclusions that are at a mid-range distance between the source and receiver produce a very small amplitude scattered wave at the receiver (figure 44a). The same test for deep scatterers produces similar results for range, but much smaller than from shallow scattering (figure 44 b). The shallow scattering makes up almost all of the scattered energy seen when summed (figure 44 a, b). The Lg that is generated, peaks around 74 seconds and decays several seconds after the Lg group velocity window. The transverse component has no direct wave due to an explosive source. The transverse components that are generated from scattering are plotted in figure 47 a. It is obvious that the shallow contributions dominate here, as well as the near-source and near-receiver contributions. The synthetics for the transverse component are summed and plotted (figure 445 b). The Lg that is generated illustrates realistic Lg shape and length. The coda is seen to emerge at the beginning of the Lg group velocity window and taper off a few seconds

after it. The vertical component due to the scattering illustrates the same general

characteristics (figure 46 a, b). There is a significantly larger near-source shallow effects,

with shallow near-receiver scattering contributing as well. The deep near-source scattering

effect does appear to be considerable. It is small, however, relative to the effects seen from

the shallow scatterer. The summed vertical components show (figure 47 a, b) that the

shallow scattering again dominates the shape and amplitude of the scattered synthetic. The

coda shape and amplitude are extended throughout the Lg group velocity window and

decay similar to observed data. It is noted that the S arrival (approximately at 50 seconds)

has gained considerable amplitude, shape and complexity of its coda.

3.3.3 Scattering at CNET

The mode-Born scattering is used to model regional data from the Caucasus array (CNET)

to see if the shallow near-source and near-receiver scattering can adequately enhance the

direct arrival. The wave path chosen for study traverses a region with shallow sediments

and that is highly faulted. This path does not undergo any significant crustal thinning and

thus may be well represented by a layered model. The chosen path is from an event on

September 22, 1992 00:38:48.347, located at 42.94 N and 44.06 E, to the southwest of the

array. The body wave magnitude of the event was 2.51 and the depth was reported as 0

km. The data (figure 48) shows strong Lg. The horizontal components are rotated to the

great circle path and put into radial and transverse form (figure 48 b). The data is

bandpassed filtered between 1 and 2 Hz and plotted (figure 49 a). An envelope of the traces

is taken to emphasize the arrivals in the Lg group velocity window (49 b). The radial and

the transverse component both have a broad Lg arrival towards the end of the group

velocity window that has a high frequency content, easily seen in the envelope function.

The synthetic of the direct arrival generated using mode summation produces a waveform that has simple peaks when the envelope of the trace is plotted (figure 50 b). The arrivals for the P and the Lg are approximately the same as seen on the vertical trace of the data (figure 49 b), indicating that the layered velocity model for the region works well with this particular source-receiver path.

Scattering is now added to try to match the complexity seen in the regional wave-form. The placement of the near-source scatterers is similar to that used in (figure 37 a). Only shallow scattering is assumed based on the results of the prior studies. Variations in Lame's parameters are 9% with a variation in density of 7%, the inclusion is assumed to be a sphere with radius 0.9 km. The result of near-source scattering for this event is plotted in figure 51. The synthetics of the scattered waves from shallow near-source scatterers have significant Lg and complexity. The envelope function is plotted to emphasize peaks of energy in the waveform. The peak that is observed in the later part of the Lg group velocity window of the direct synthetic is broader and is similar in shape to the observed data. The result for near-receiver combined with near-source scattering does not noticeably alter the scattered components due only to near-source scattering.

Arbitrarily placing scatterers near the source and receiver in this particular case dramatically improved the match between observed data and synthetic. While there is little doubt that arbitrarily placed shallow scattering can adequately model Lg coda, it is unknown whether known small scale crustal features may be incorporated into a model capable of producing realistic coda.

3.3.4 Scattering at Pinion Flat

The conventional thought is that seismic coda is the result of the scattering of waves from randomly distributed subsurface heterogeneities (Aki and Chouet, 1975; Sato, 1977). It has been suggested that regional crustal features such as faults may be a source of scattering (Mitchell 1995), thus offering a deterministic model based on known crustal features instead of a random distribution. Recently, IRIS broadband data from Pinion Flat Observatory (PFO) has been observed to have off-azimuth energy that was not attributed to the standard back-scattering from random lateral heterogeneities, but attributed to the regional north-west trend in crustal structure (Wagner, 1996). As an alternative to a model consisting of randomly placed heterogeneities, Wagner (1997) suggests allowing the heterogeneities to be spatially anisotropic. Spatially anisotropic heterogeneities cause spatially anisotropic scattering, and provide a characterization of subsurface structure that is more consistent with certain geological models (Wagner and Langston, 1992; Wagner,1996).

To test a scenario of spatially anisotropic heterogeneities, mode-Born scattering is applied to model the complexity seen in the regional wave-forms. A fault-like structure is approximated by a linear zone of inclusions surrounding the source and aligned at a 30 degree azimuth with respect to the source (figure 52). The inclusions have volumes of 0.2 km^3 and variations in Lame's parameters, λ and μ, of 3%, and ρ of 2%. The distance between source and receiver is 17.75 km. The direct synthetic due to an explosive source in a cavity of .1 km^3 is plotted with the complete waveform that includes scattering from the 'fault' (figure 53 a). The complexity and shape of the synthetics that account for the spatially anisotropic scattering provide for realistic coda in shape and amplitude. The envelope function of the direct and complete waves are taken to illustrate the amplitude of

the coda (figure 53 b). It is noticed that the explosion generates significant transverse energy when scattered from the fault. The coda envelope lengths double in time and there is slight attenuation in peak amplitude of the vertical component due to deconstructive interference.

To determine if the synthetics could be analyzed for off azimuth energy, a simple array on the same order of Pinion Flat was created to record synthetics (figure 54). Frequency-wave number (f-k) analysis was performed using SAC to plot azimuthal characteristics in arriving energy. The time windowed S coda from this synthetic array is shown in figure 60 along with the f-k plot (figure 55b). The maximum radial wavenumber is 4 radian-seconds/km, and the figure shows linear contour spacing. There is an identifiable trend of 30° azimuth in the f-k plot, which correlates well with the strike of the fault .

3.4 Summary of scattering experiments

Small scale heterogeneity is well modeled by a single scattering approximation and can account for the duration, complexity, and component equalization seen in Lg coda. The mode-Born method of calculating single scattering, which uses an equivalent point source to reradiate the seismic energy, is a fast and efficient way to predict the complexity observed in regional seismic coda

For shallow sources such as mining blasts, surface faults and nuclear explosions, shallow scattering statistics close to the source and receiver are shown to be much more important in controlling Lg complexity than detailed knowledge of scattering statistics all along the crustal waveguide. This supports the hypothesis that shallow sediments account for much of the lateral scattering. The effect of shallow small scale scattering would be compounded

75

if, as in the first part of this report, sediment basins trap Lg and then proceed to scatter Lg by small scale heterogeneities within the basin.

Scattering near-source, can convert the strong fundamental Rayleigh mode to higher modes. The fundamental mode Rayleigh wave is known to attenuate rapidly and travel relatively small distances, and thus does not contribute equally throughout the scattering ellipse. If the fundamental mode Rayleigh wave is not modeled correctly, or if shallow attenuation (Q) is inaccurate, the scattering from the fundamental mode will also be incorrectly modeled.

Explosive sources are seen to generate transverse energy due to near source and near receiver small scale heterogeneity. This is a particularly important point in terms of discrimination, suggesting that in regions of thick sediment, with perhaps structural complexity of folds and thrusts, a small explosion may generate enough transverse energy to be appear earthquake-like. This indicates that in regions with complex sediment structure, particular attention must be paid to array placement. The mode-Born method therefore may be used to predict and optimize array locations to enhance discrimination capabilities in a given area.

The size of the heterogeneities that were capable of adding complexity to the wave form and at the same time not dominate its shape were on the order of .5 - 1.0 km, with small variations of Lame's parameter's of 3% well within maximum crustal variations of 5-6%.

Preliminary tests using spatially anisotropic heterogeneities work well in regions characterized by a dominant trend of deformation. With a general knowledge of basin structure as well as trends in regional geology, it may be possible to model seismic data

very accurately without resorting to a completely statistical descriptions of crustal heterogeneities.

An understanding of the effects of small scale heterogeneities and their variation as a function of large scale crustal structure and tectonic setting, together with the gross effects of phase blockage of large scale structure, will form an important knowledge base for the transportability of seismic methods of detection, discrimination and yield estimation.
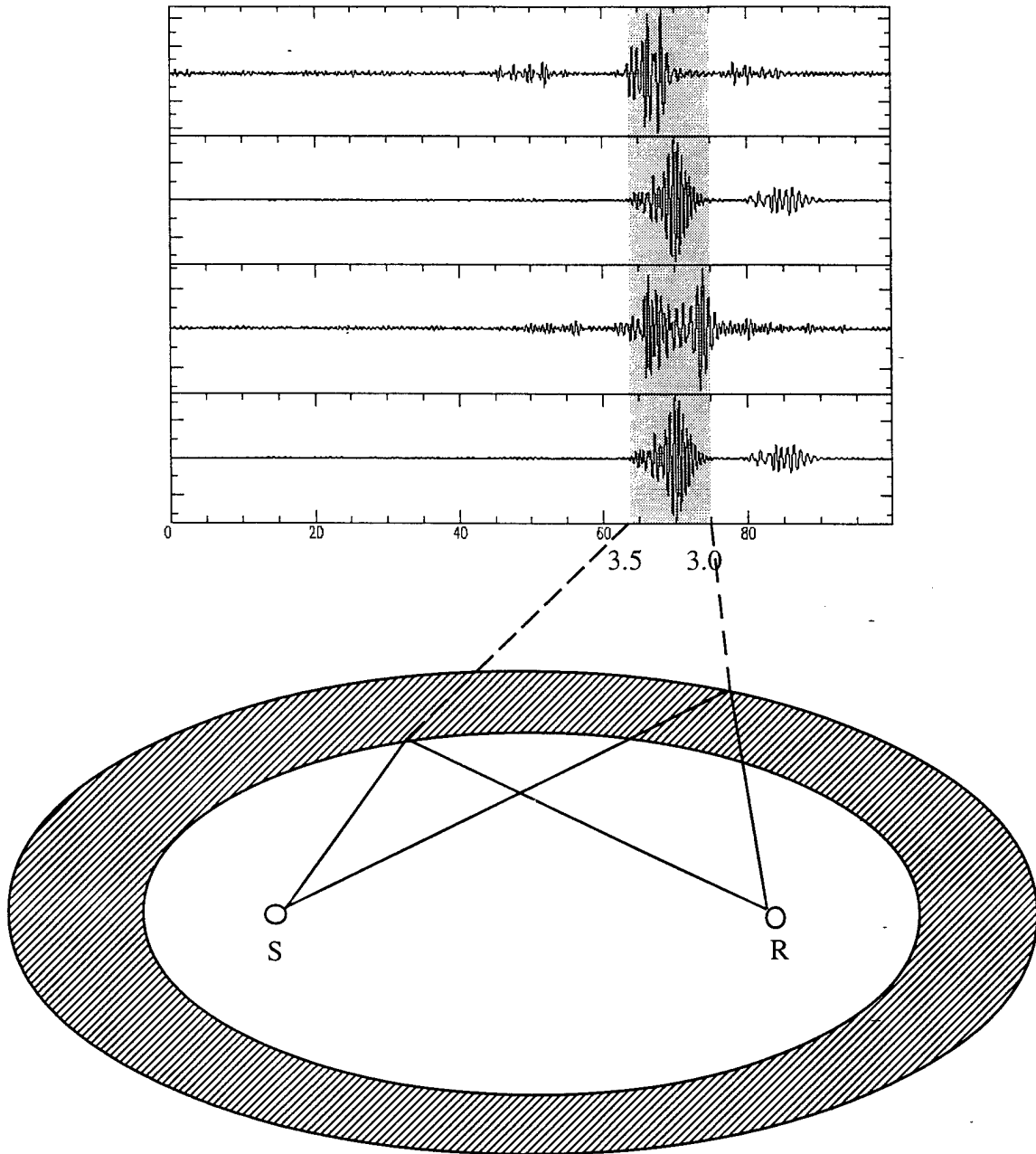
Figure 27: Scattering ellipse, with foci at source and receiver and length of major axis equal to vt and v(t+Δt), where v is velocity, and t is time. Assuming for simplicity that scattering occurs with out mode conversion, for a particular mode, the shaded region represents the region that contributes to a particular velocity window. In the example above, the Lg group velocity is highlighted. The shaded elliptical zone is the region that may contain heterogeneities that would contribute to amplitudes in the group velocity window of 3.0 to 3.5 km/sec.

θ1: Source -scatterer relative position

θ2: Scatterer-receiver relative position used in F2,F3.

θ3: Scatterer-receiver relative position for F1 at scatterer. This is equal to $\pi/2-\theta2$

θ4: Scatterer-receiver relative position for equivalent moment source. This is equal to $\theta2 - \theta1$
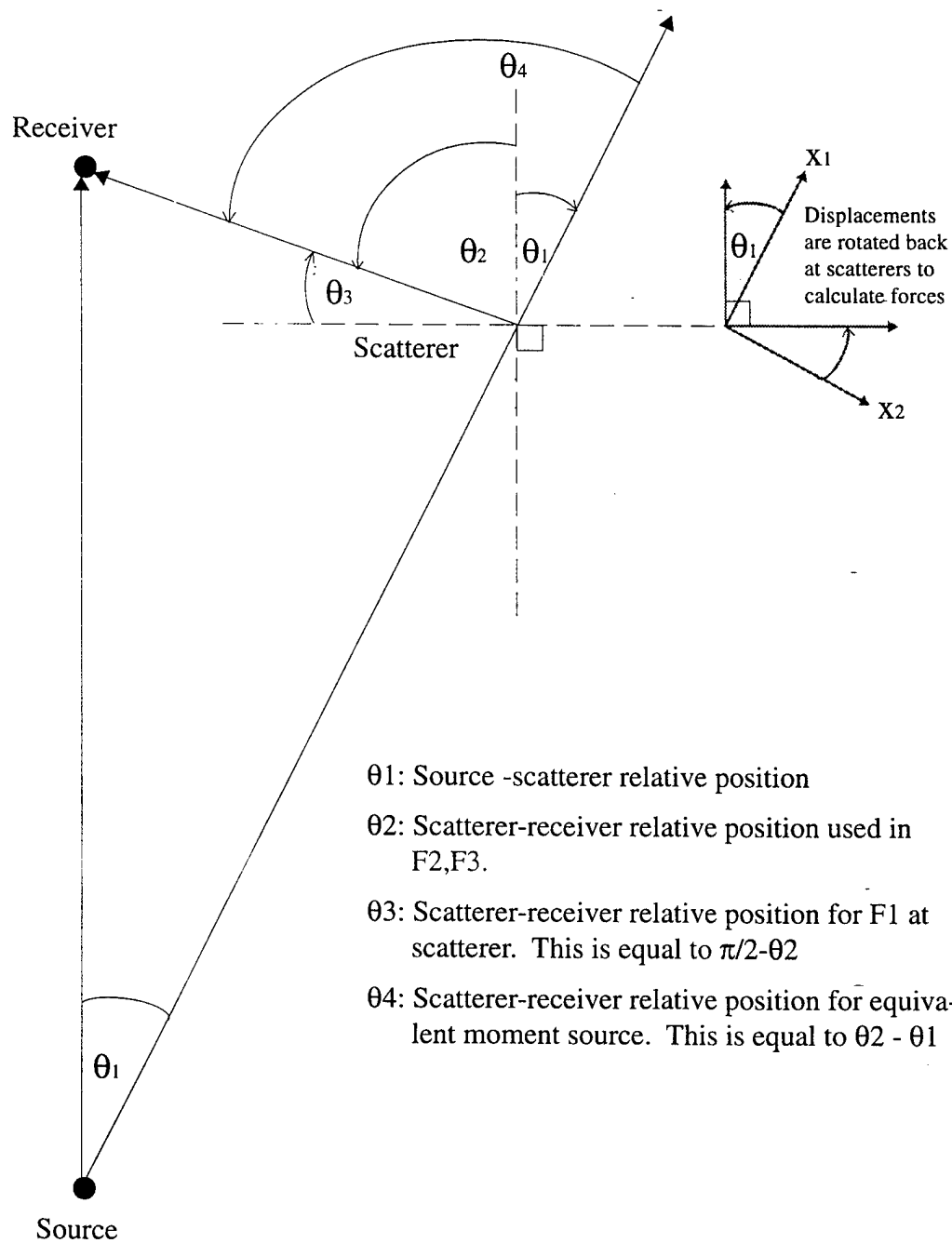
Figure 28: Geometry of source-scatterer-receiver used in Mode-Born program.

layer no.	depth to top (km)	P-wave velocity (km/sec)	S-wave velocity (km/sec)	density (g/cm^3)
1	0.00000	5.53000	3.23000	2.40000
2	0.34500	5.66000	3.31000	2.43000
3	1.34500	5.79000	3.39000	2.46000
4	2.34500	5.90000	3.46000	2.49000
5	3.34500	5.97000	3.50000	2.52000
6	4.34500	6.02000	3.53000	2.55000
7	5.34500	6.05000	3.54000	2.58000
8	6.34500	6.07000	3.56000	2.61000
9	7.34500	6.10000	3.57000	2.64000
10	8.34500	6.12000	3.58000	2.67000
11	9.34500	6.14000	3.60000	2.70000
12	10.34500	6.17000	3.61000	2.73000
13	11.34500	6.19000	3.62000	2.76000
14	12.34500	6.22000	3.64000	2.77000
15	13.34500	6.25000	3.66000	2.78000
16	14.34500	6.28000	3.68000	2.79000
17	15.34500	6.31000	3.69000	2.80000
18	16.34500	6.33000	3.71000	2.81000
19	17.34500	6.36000	3.73000	2.82000
20	18.34500	6.39000	3.74000	2.84000
21	19.34500	6.42000	3.76000	2.85000
22	20.34500	6.45000	3.76000	2.85000
23	21.34500	6.47000	3.79000	2.87000
24	43.34500	8.10000	4.60000	3.34000
25	69.34500	8.60000	4.90000	3.50000
26	399.34500	11.00000	6.00000	6.00000

Table 2: The mode catalogue used for Pinon Flats synthetics was generated using this structure model, based on the optimal 1-D Anza velocity model *(Scott et al., 1994).*
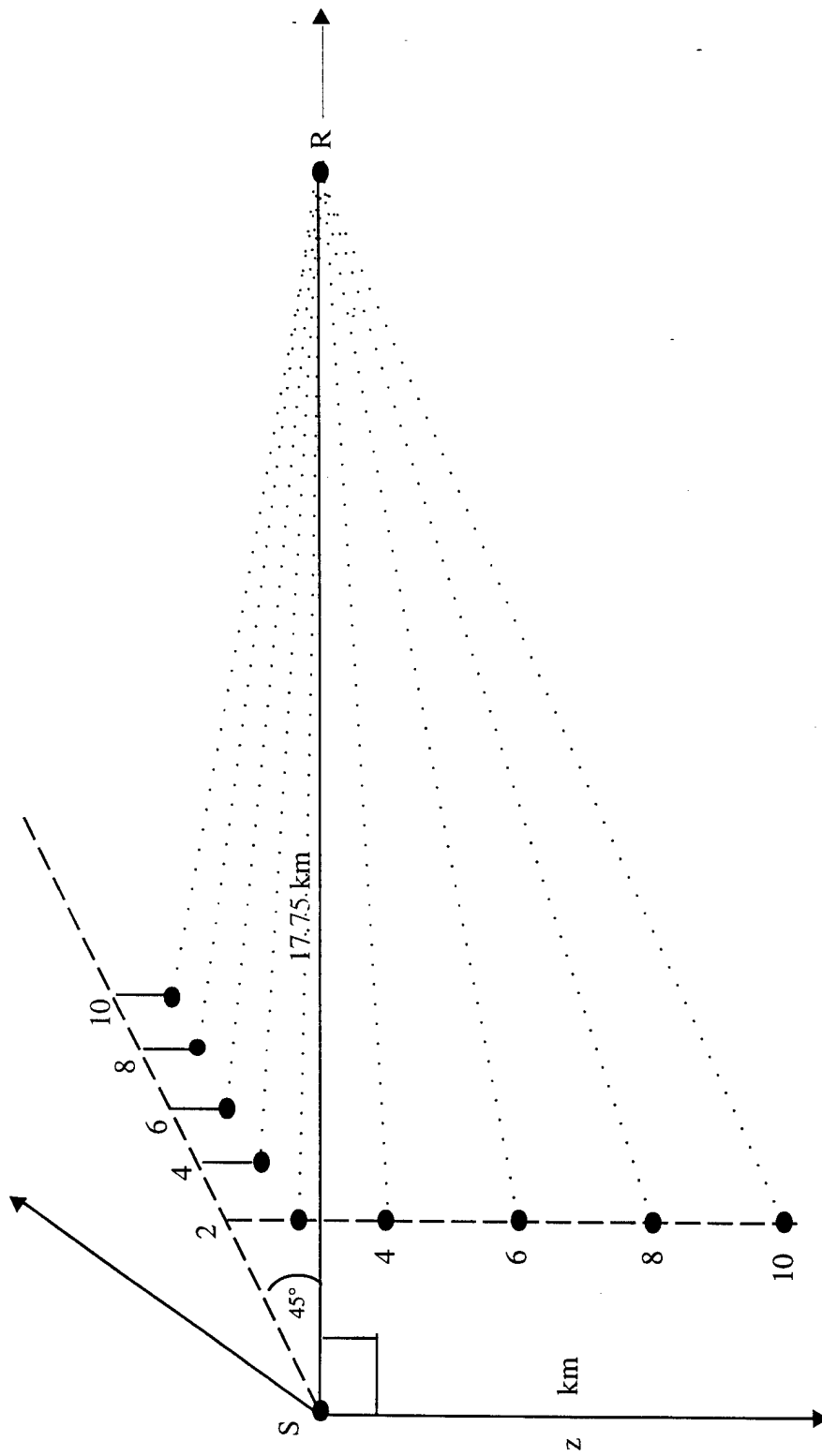
Figure 29: Geometry of scatterers used to calculate synthetic in figures 32-38. The illustration is for near source geometry; the near receiver geometry is set up exactly the same.
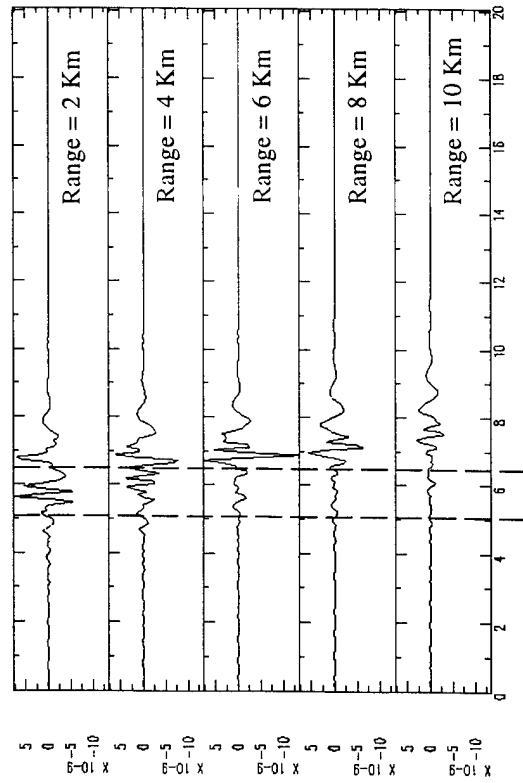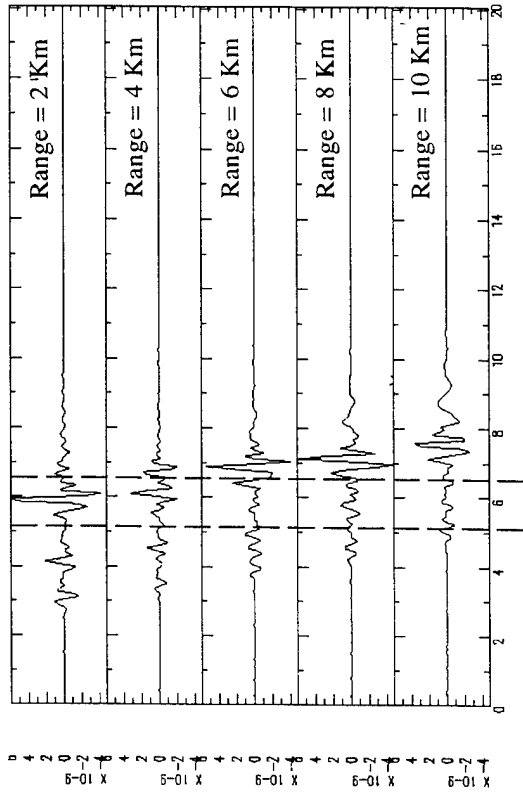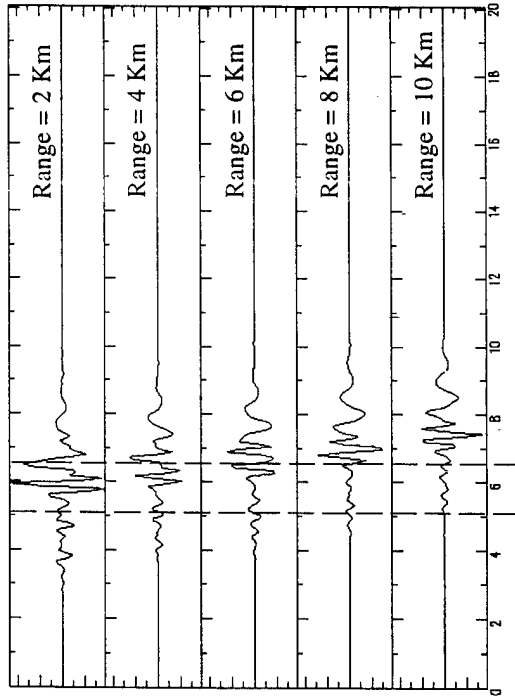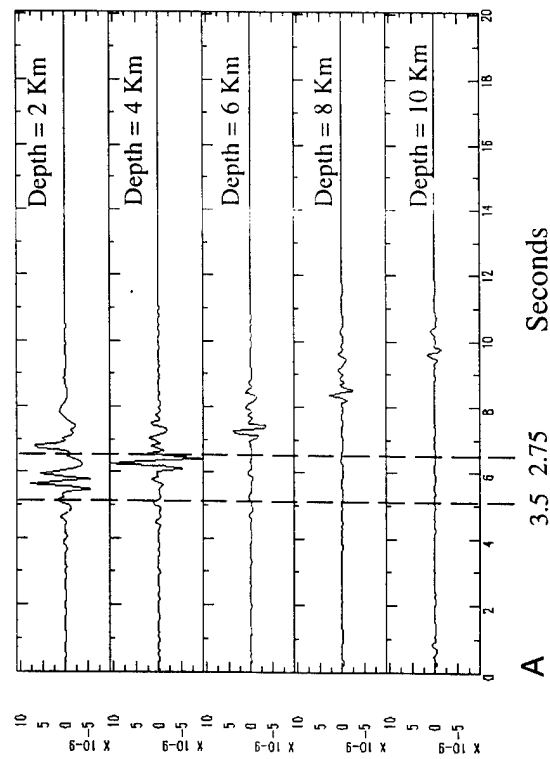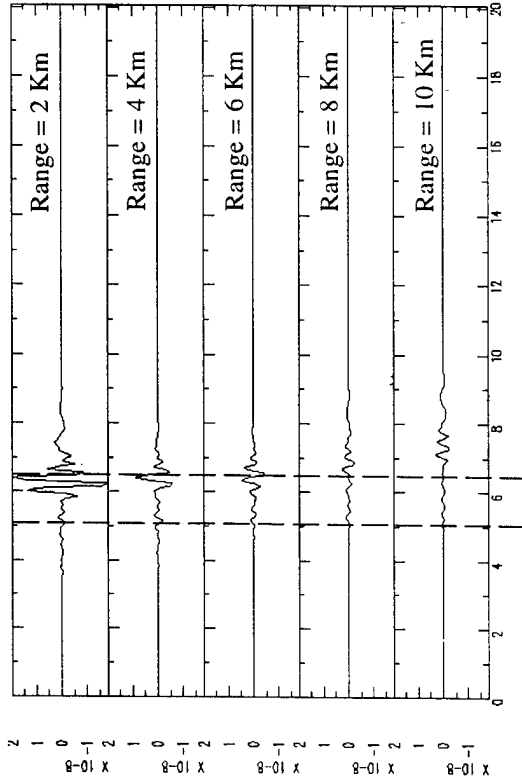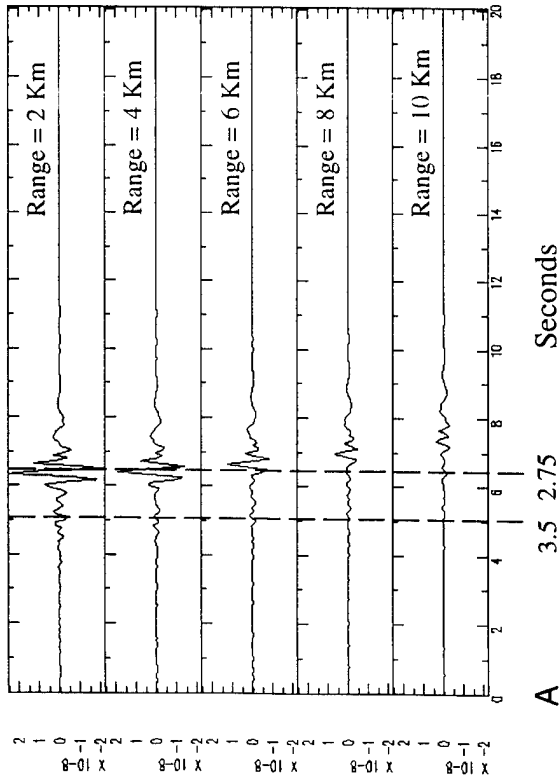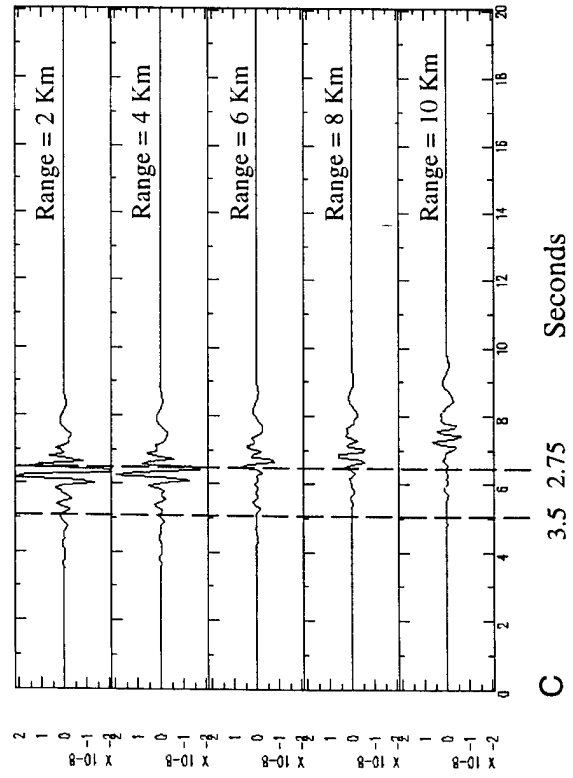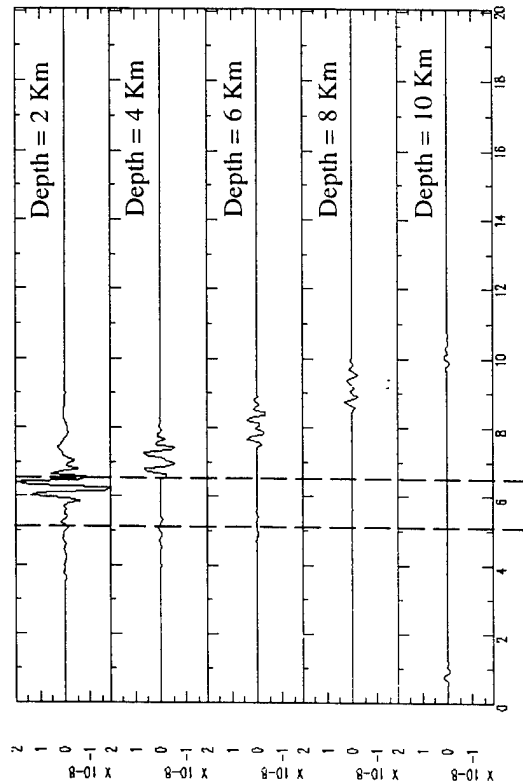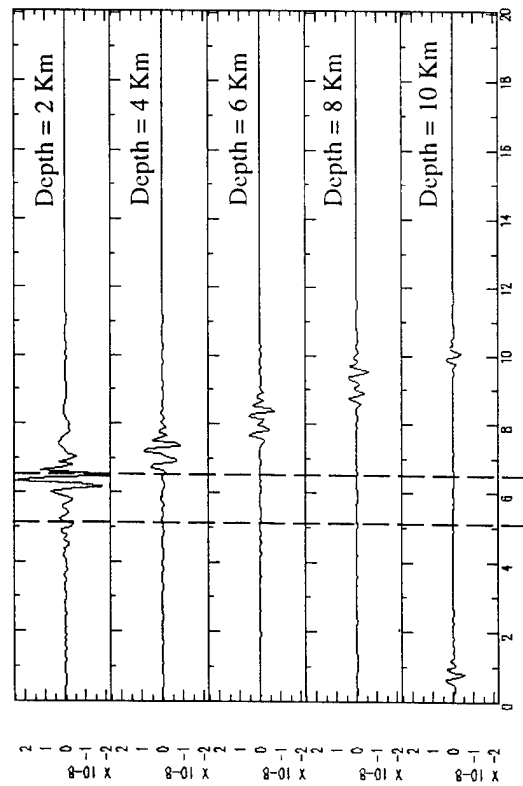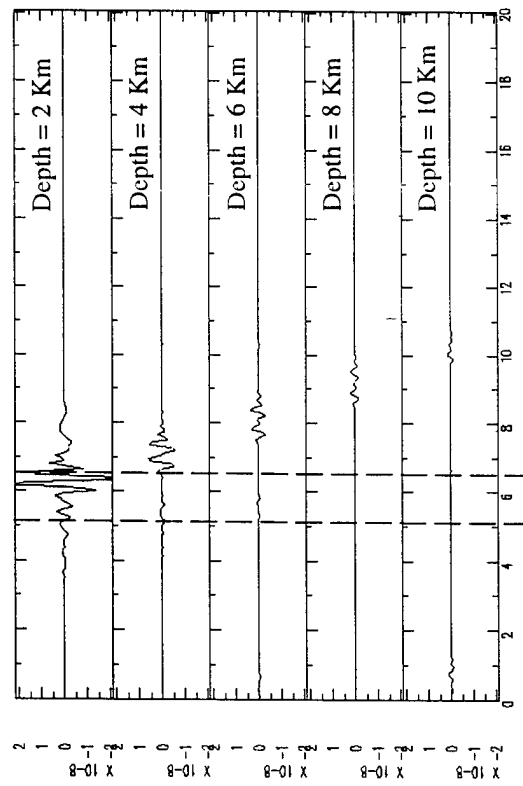
Figure 30: The synthetics generated from a single inclusion with values of λ, μ of -8% and ρ of -5% at a constant depth of 2 km and range increasing in 2 Km intervals along an azimuth 45° from the source (see figure 32). The source-receiver distance is 17.75 Km. A) Radial component B) Transverse component; C) Vertical component Phase velocities of 3.5 amd 2.75 km/s are marked by dashed line to show Lg arrival window.
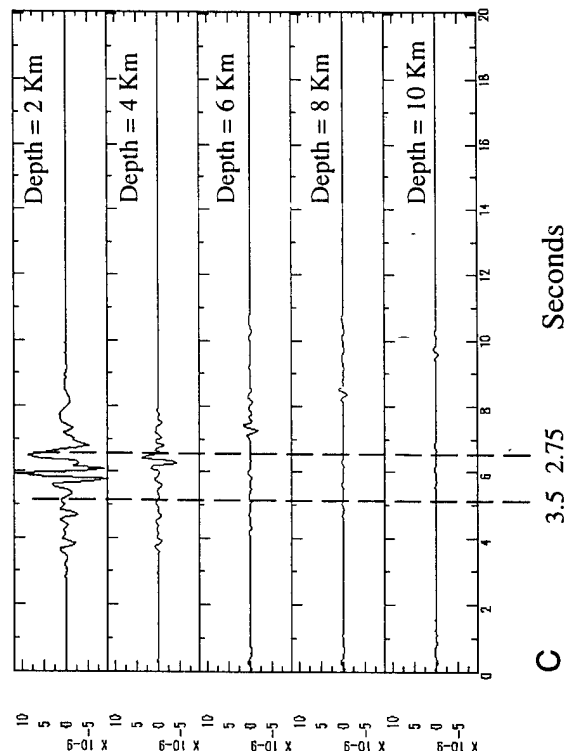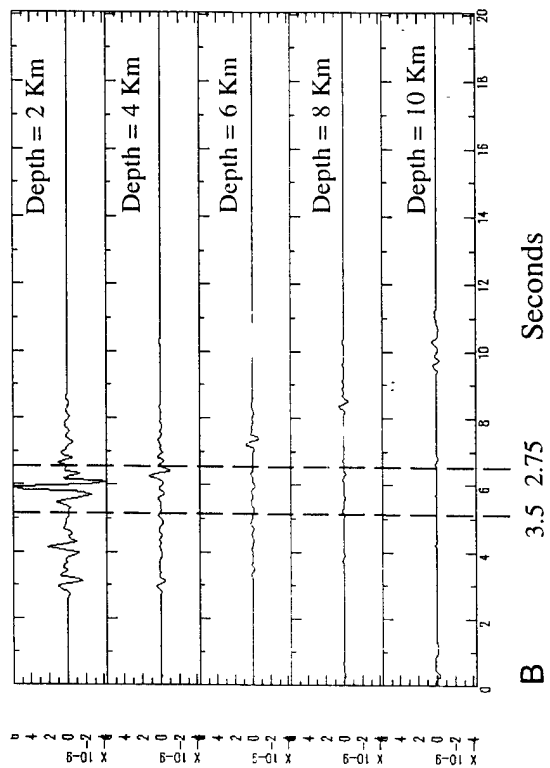
Figure 31: The synthetics generated from a single inclusion with values of λ, μ of -8% and ρ of -5% at a constant range of 2 km along a line with respect to 45° from source and depth increasing in intervals of 2 Km. The source-receiver distance is 17.75 Km. A) Radial component; B) Transverse component; C) Vertical component

Figure 32: The synthetics generated from a single inclusion with values of λ, μ of -8% and ρ of -5% at a constant depth of 2 km and range increasing in 2 Km intervals along an azimuth 45° from the receiver line. The source-receiver distance is 17.75 Km. A) Radial component; B) Transverse component; C) Vertical component

Figure 33: The synthetics generated from a single inclusion with values of λ, μ of -8% and ρ of -5 % at a constant range of 2 km along a line with respect to 45° from receiver and depth increasing in intervals of 2 Km. The source-receiver distance is 17.75 Km. A) Radial component; B) Transverse component; C) Vertical component

Amplitude of Lg phase window for Envelope
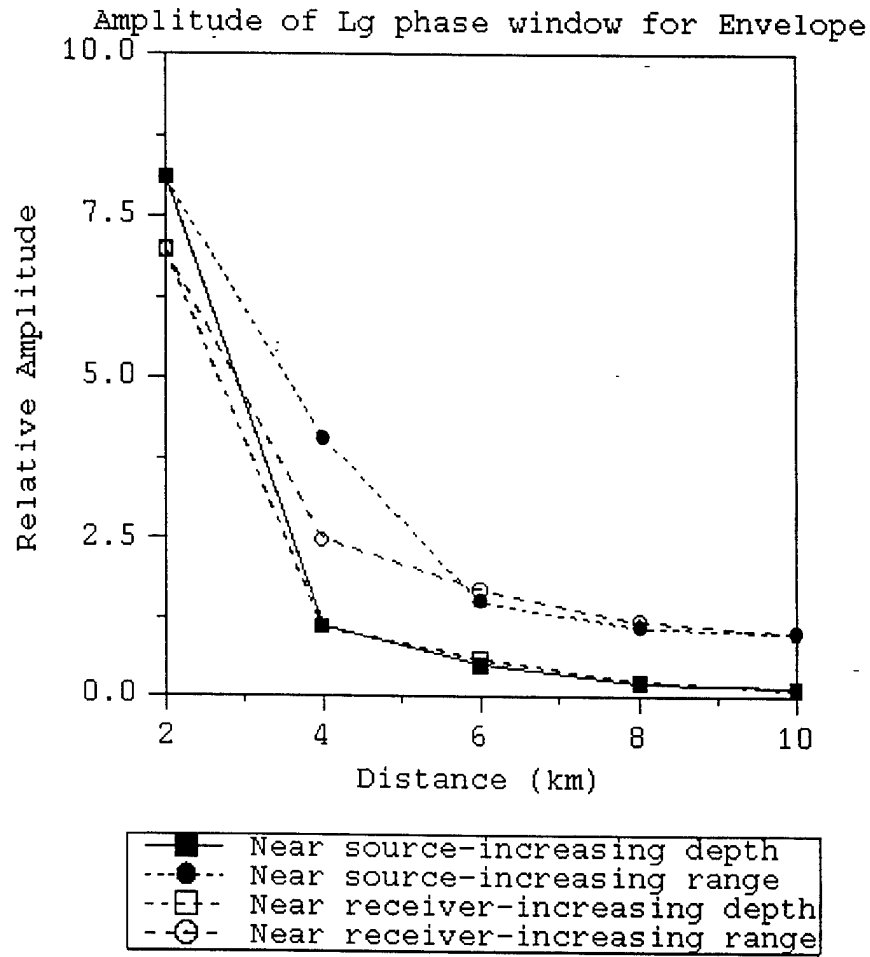
Figure 34: Plotted are the maximum envelope amplitudes from the phase velocity group velocity window 3-3.5 km/s for the vertical component in figures 5-8. The near source and near receiver scenarios produce amplitudes that vary almost identically as the inclusion is moved in both increasing horiziontal range and depth.
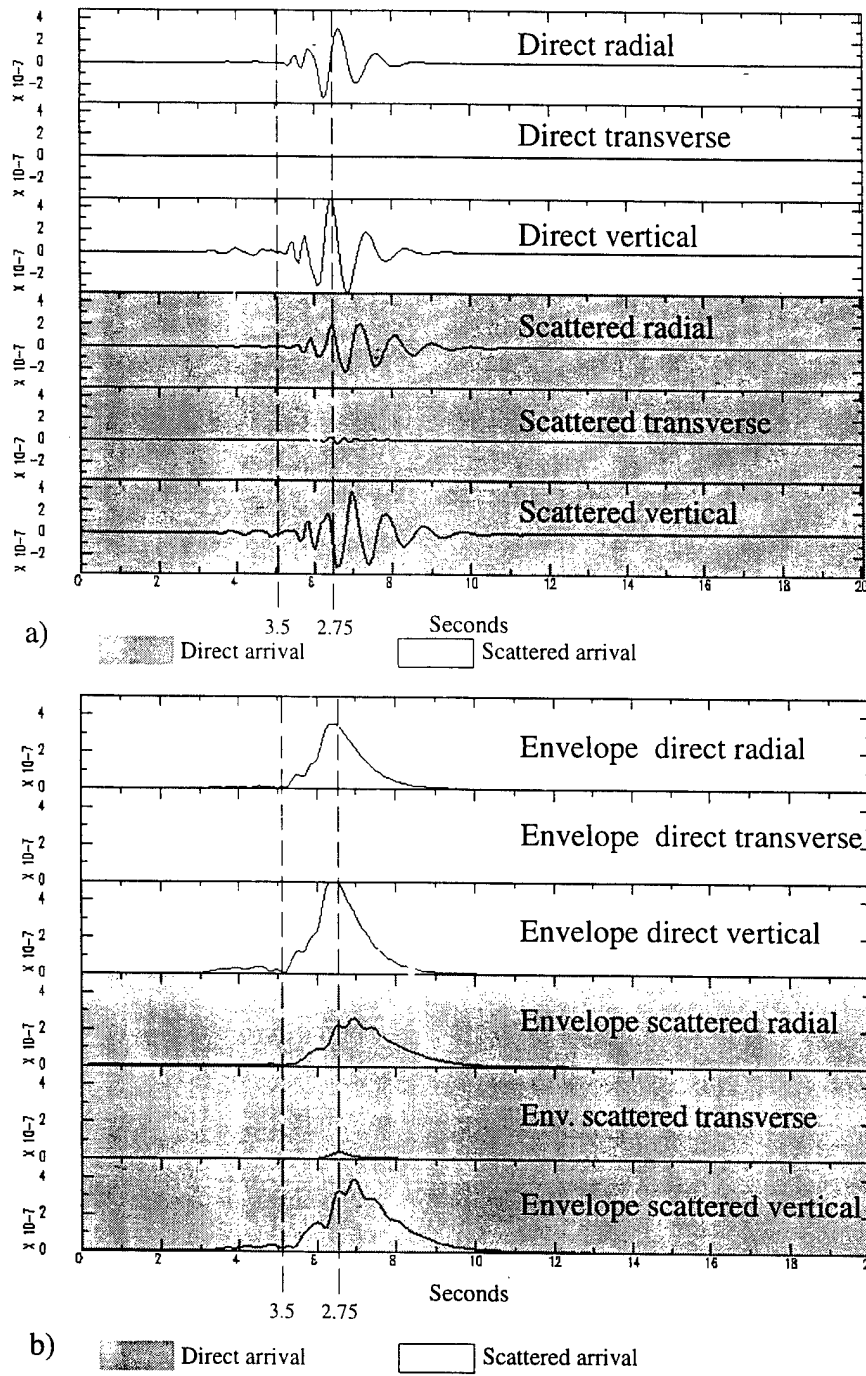
Figure 35: a) Reference waveforms plotted with summation of scattered synthetics.

b) Envelope of reference waveforms and scattered components. Notice that the maximum

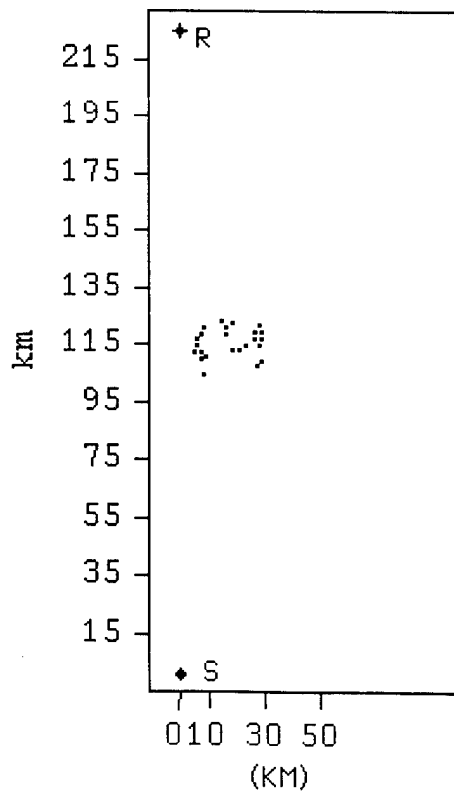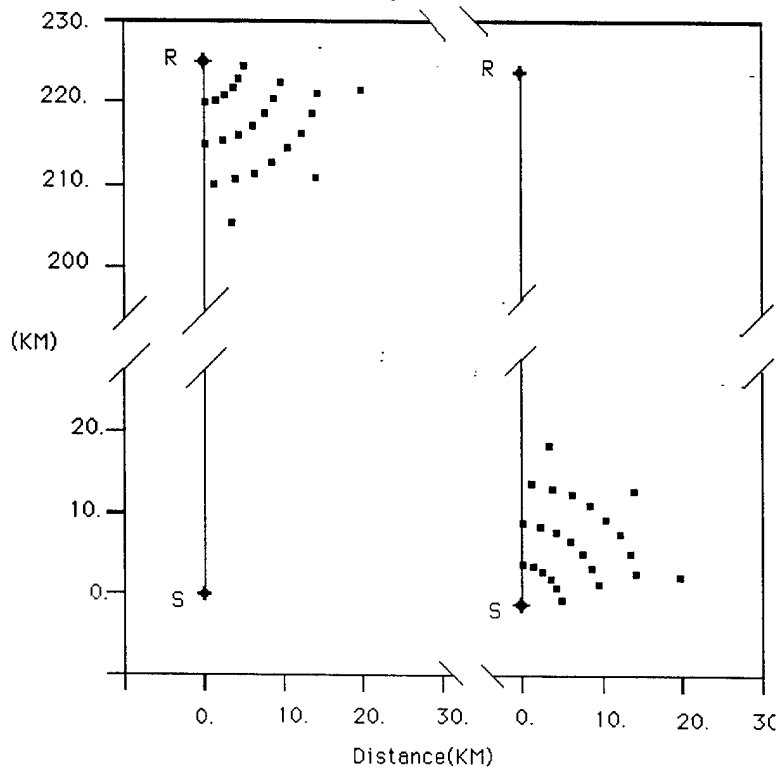amplitude has decresed but the length and amplitude of coda has increased.

Figure 36: Map views of scattering geometry for synthetics illustrated in figures 40-52. These geometries are used to test the effects of scatterers at shallow (2-4 km) and deep (25-27 km) locations relative to the source and receiver.
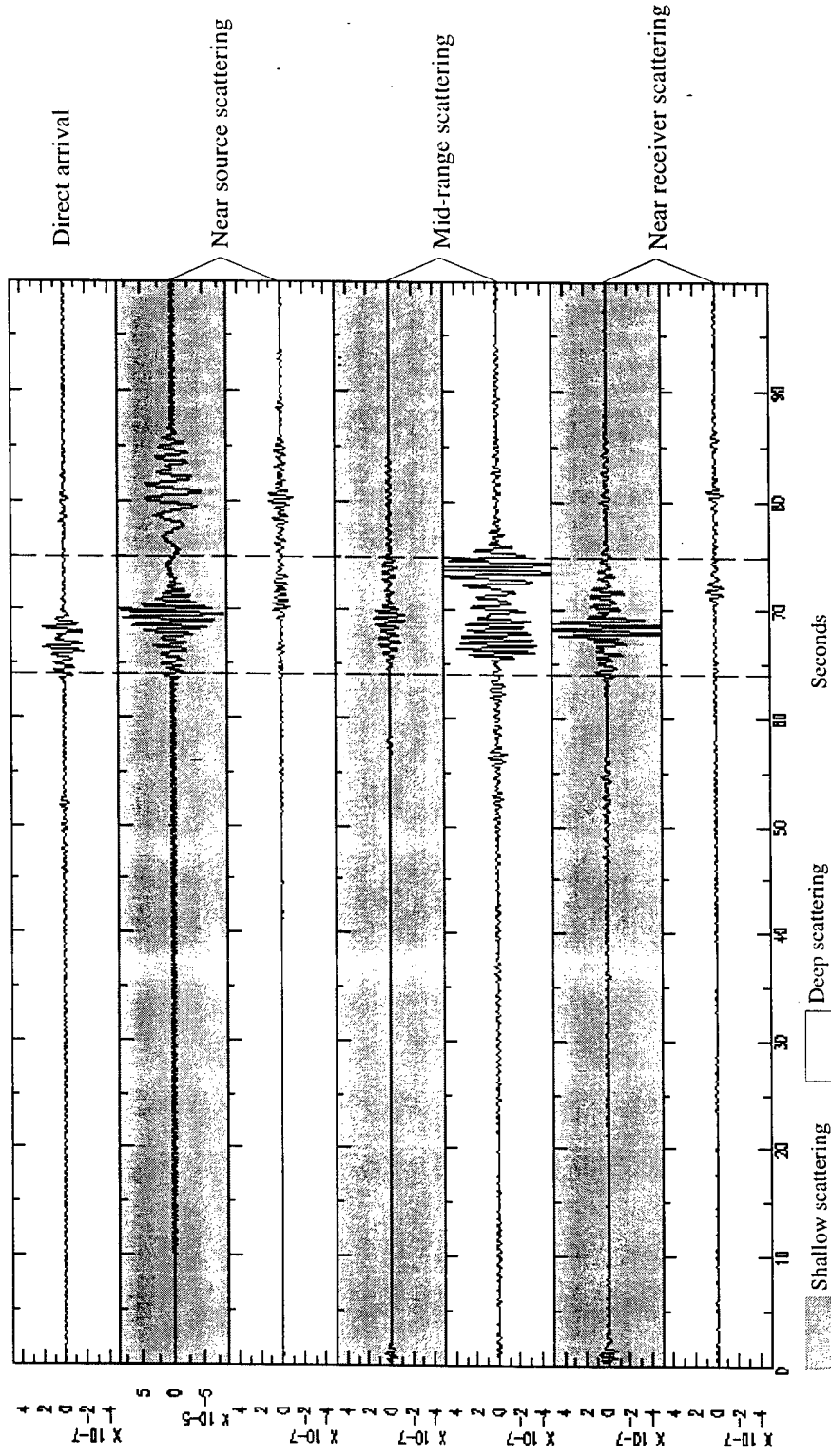
Figure 37: Radial component of mode synthetics due to an earthquake source. This illustrates range and depth effects on the scattered components (see figure 39 for location geometry). Top trace is the direct arrival and is plotted to scale with other all arrivals except the synthetic due to shallow near source inclusions. The shallow near source effects dominates by a factor of 10. It is noted that mid source scattering contributes on the same order to the L_g phase arrival as near receiver scattering.
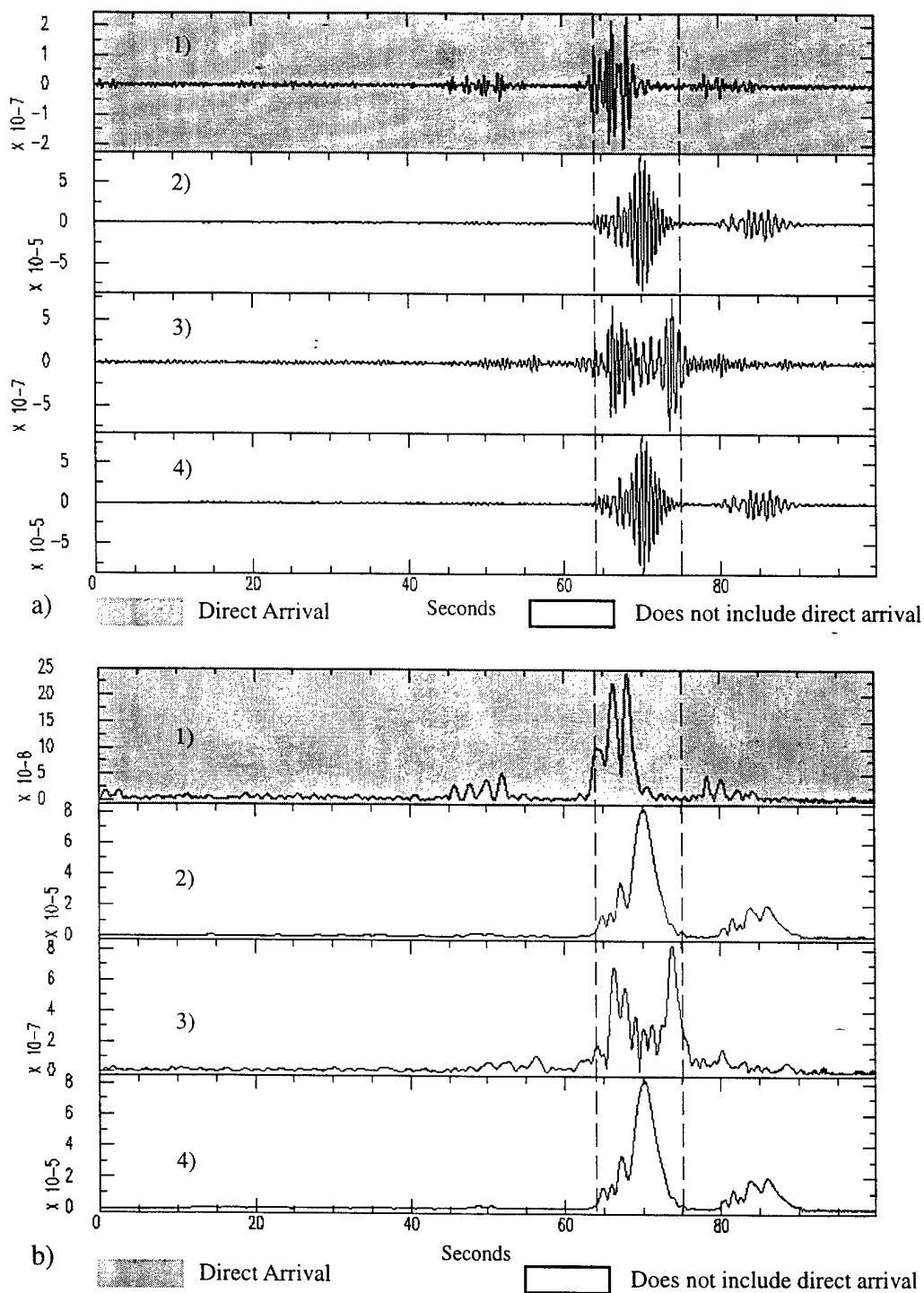
Figure 38: Radial component of mode scattering synthetics due to an earthquake source. a) Illustrates 1) direct waveform, 2) summation of synthetics from shallow scattering all ranges, 3) deep scattering all ranges and 4) entire geometrical spectrum. Shallow scattering effects dominate in the synthetic that is a sum of all contributions. b) A plot of the envelopes of the waveforms in figure a. Note that the shallow scattering geometry may increase the coda in amplitude and duration.
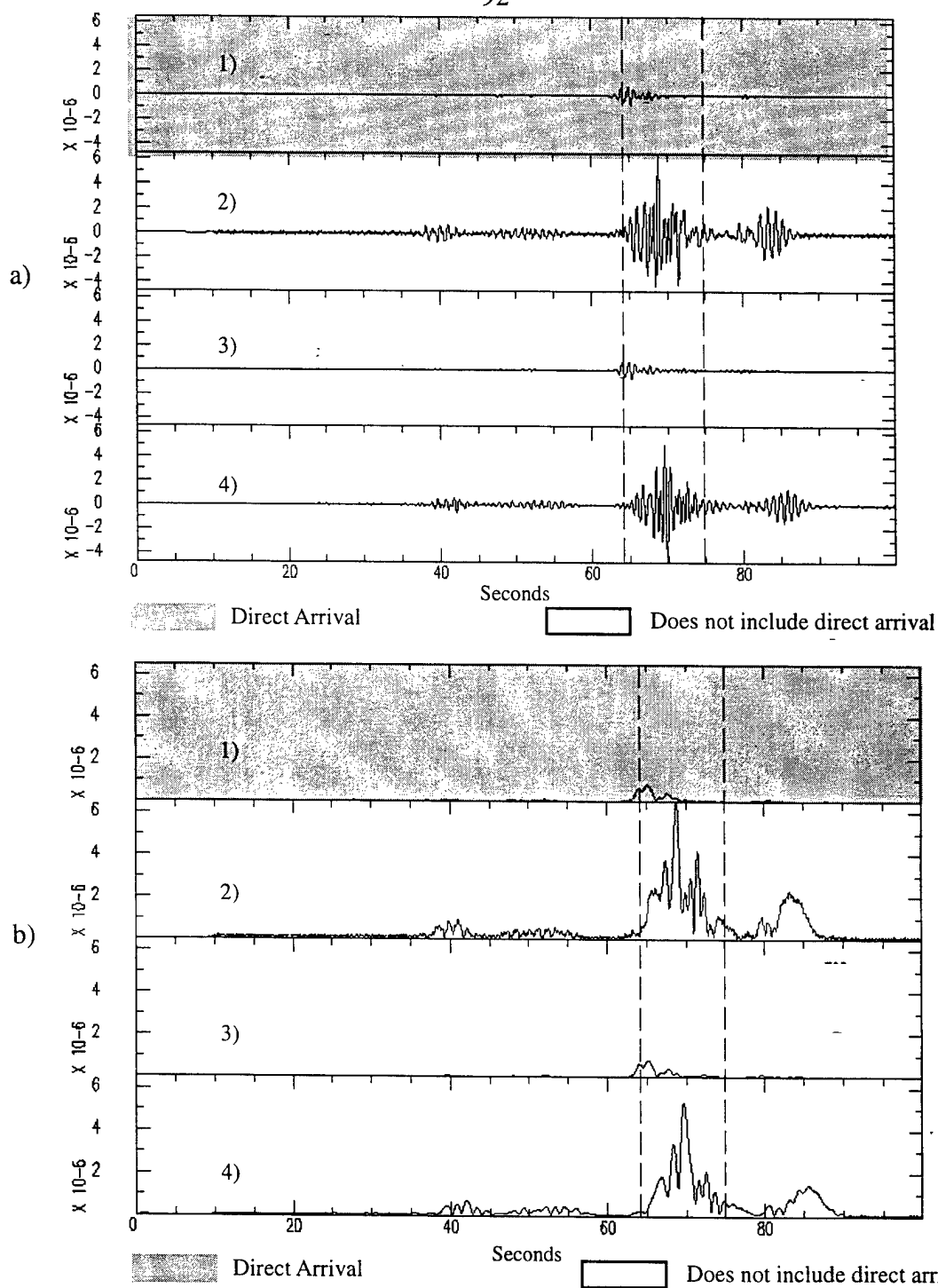
Figure 39: Transverse component of mode scattering synthetics due to an earthquake source. This illustrates range and depth effects on the scattered components (see figure 39 for location geometry). Top trace is the direct arrival. It is noted that shallow near source scattering and near receiver contributions dominate scattering effects and that scatterers at mid range geometry do not have a strong effect.

Figure 40: Tranverse component from Earthquake. a) 1) direct waveform, 2) summation of synthetics from all depths and ranges ranges, 3) deep scattering all ranges and 4) shallow scattering all ranges. Deep scattering effects have a smoothing effect on the coda in the synthetic that is a sum of all contributions. b) A plot of the envelopes of the waveforms in fig a. Note that the scattering adds significant amplitude and length to Lg compared to the direct wave and that while deep scattering smooths and attenuates the Lg, it does not change the characteristics significantly.
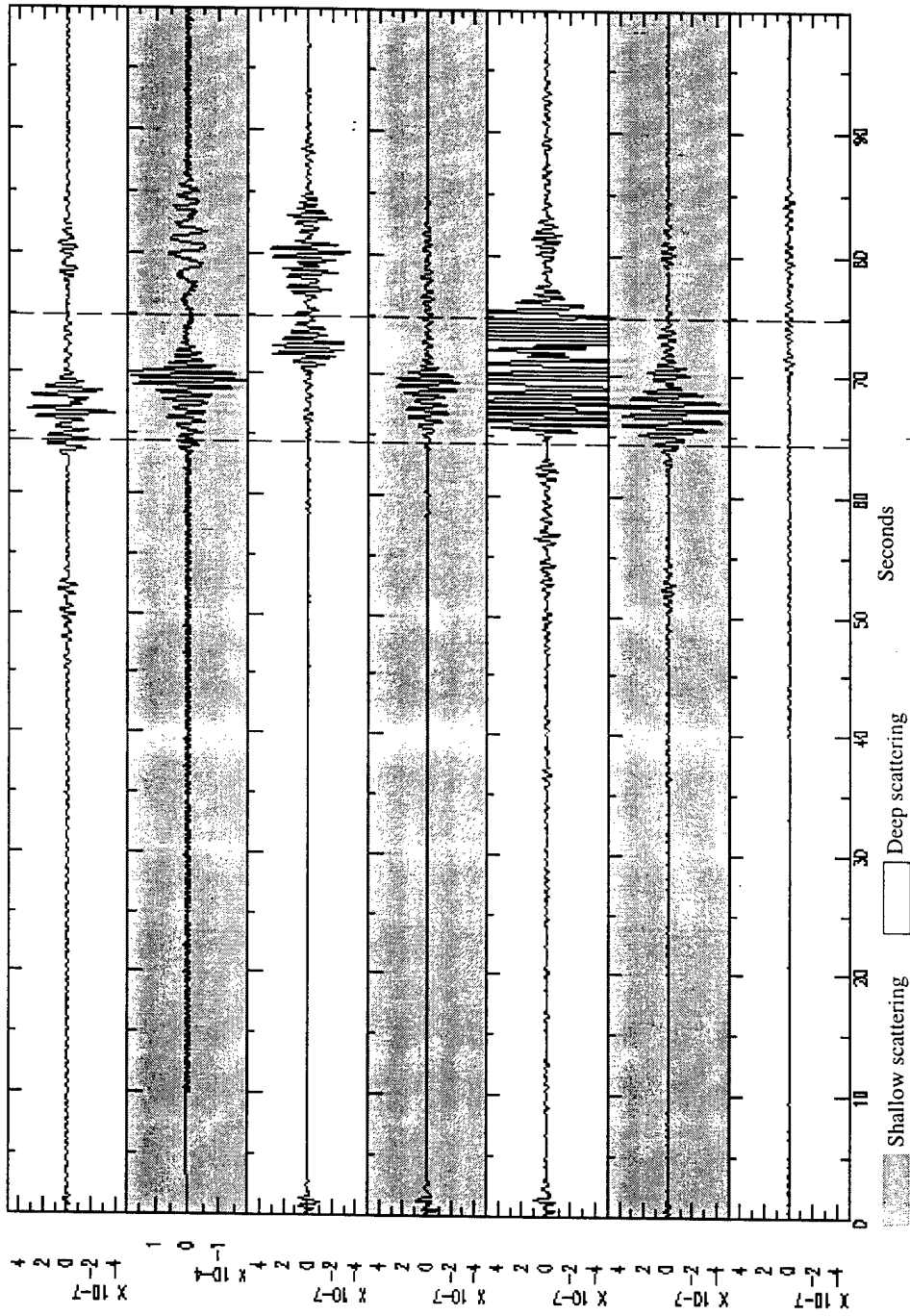
Figure 41: Vertical component of mode scattering synthetics due to an earthquake source. This illustrates range and depth effects on the scattered components (see figure 39 for location geometry). Top trace is the direct arrival. The shallow near source effects dominate by a factor of 100. It is noted that mid-source scattering contributes on the same order to the Lg phase arrival as the deep near source and shallow near receiver scattering.
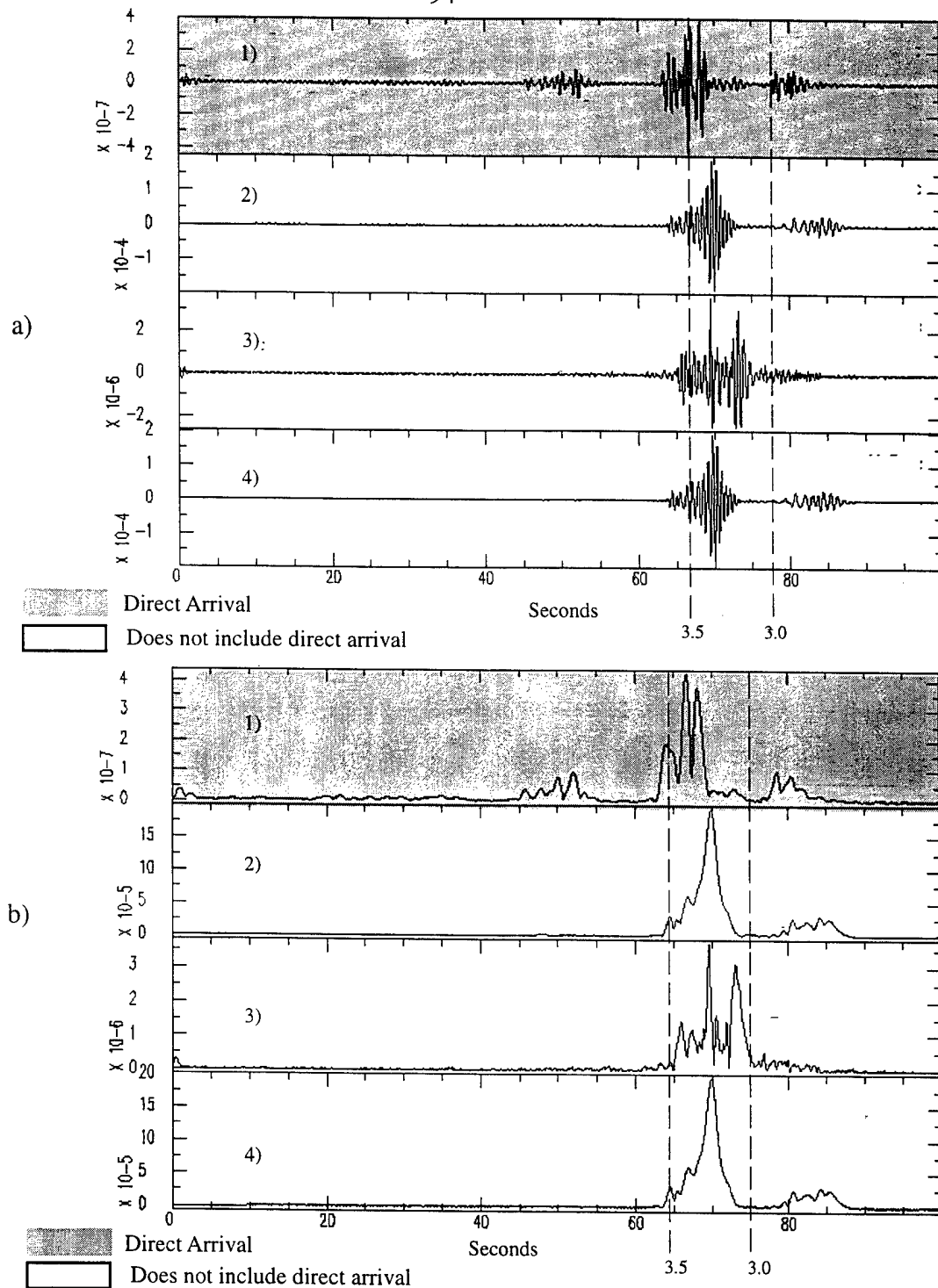
Figure 42: Vertical component mode scattering synthetics from an earthquake source. a) The 1) direct arrival, 2) direct arrival and all scattered components, 3) direct arrival and contribution from deep scattering, 4) direct arrival and contribution from shallow scattering. Note that the shallow scattering is significantly larger than the deep scattering. b) The envelopes of the synthetics are plotted to illustrate the lengthening of coda due to scattering from lateral heterogeneities. Shallow effects contribute most to lengthening the coda envelope.
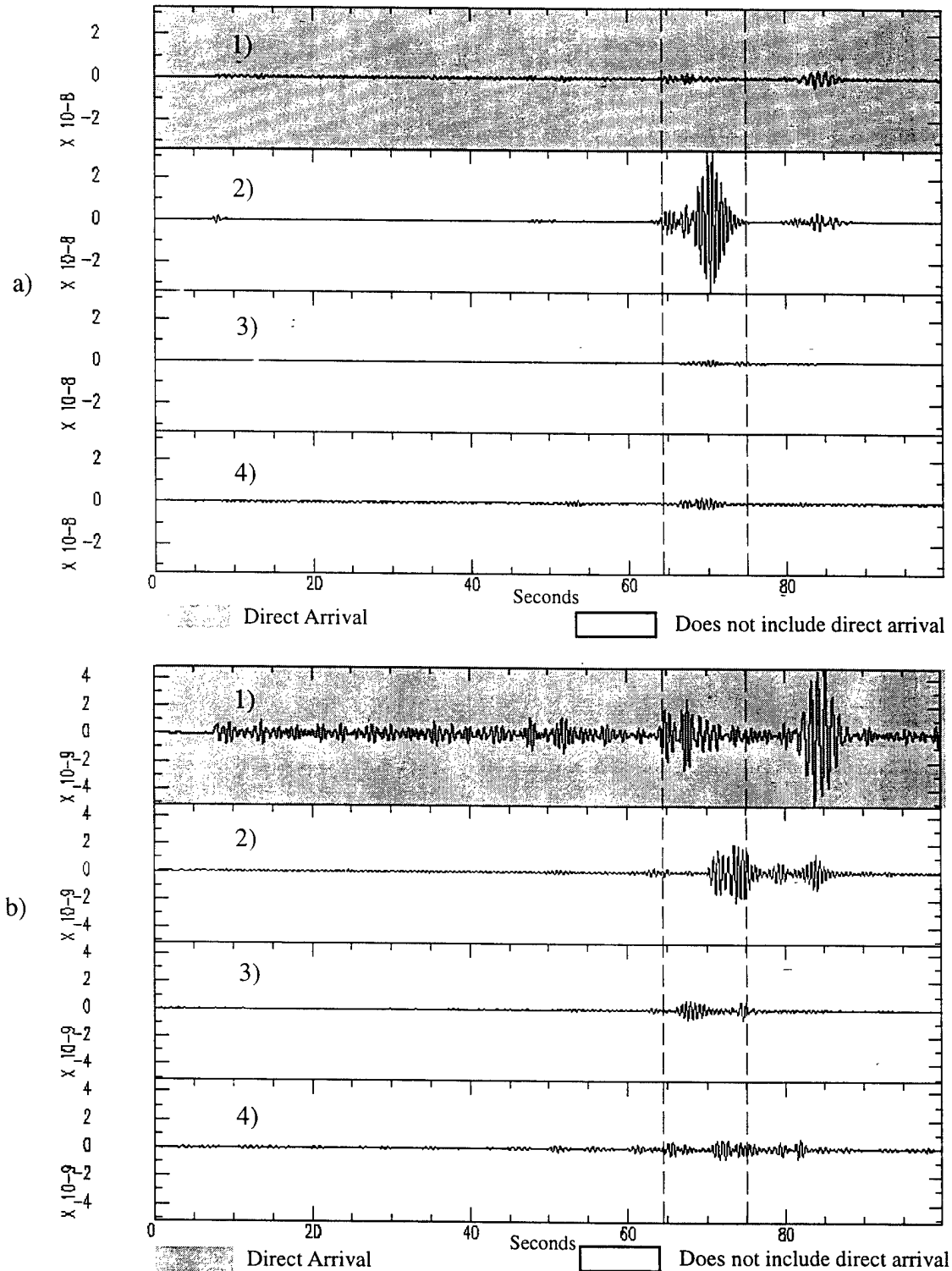
Figure 43 a,b: Radial component of mode scattering synthetics due to an explosion source. a) This illustrates range effects from shallow scattering 1) direct arrival, 2) near-source, 3)mid-range, 4) near-receiver. b) Range effects due to deep heterogeneities. scattering 1) direct arrival, 2) near-source, 3)mid-range, 4) near-receiver. The shallow near source effects dominates by a factor of 10. It is noted that mid-range scattering contributes on the same order to the Lg phase arrival as near-receiver scattering.
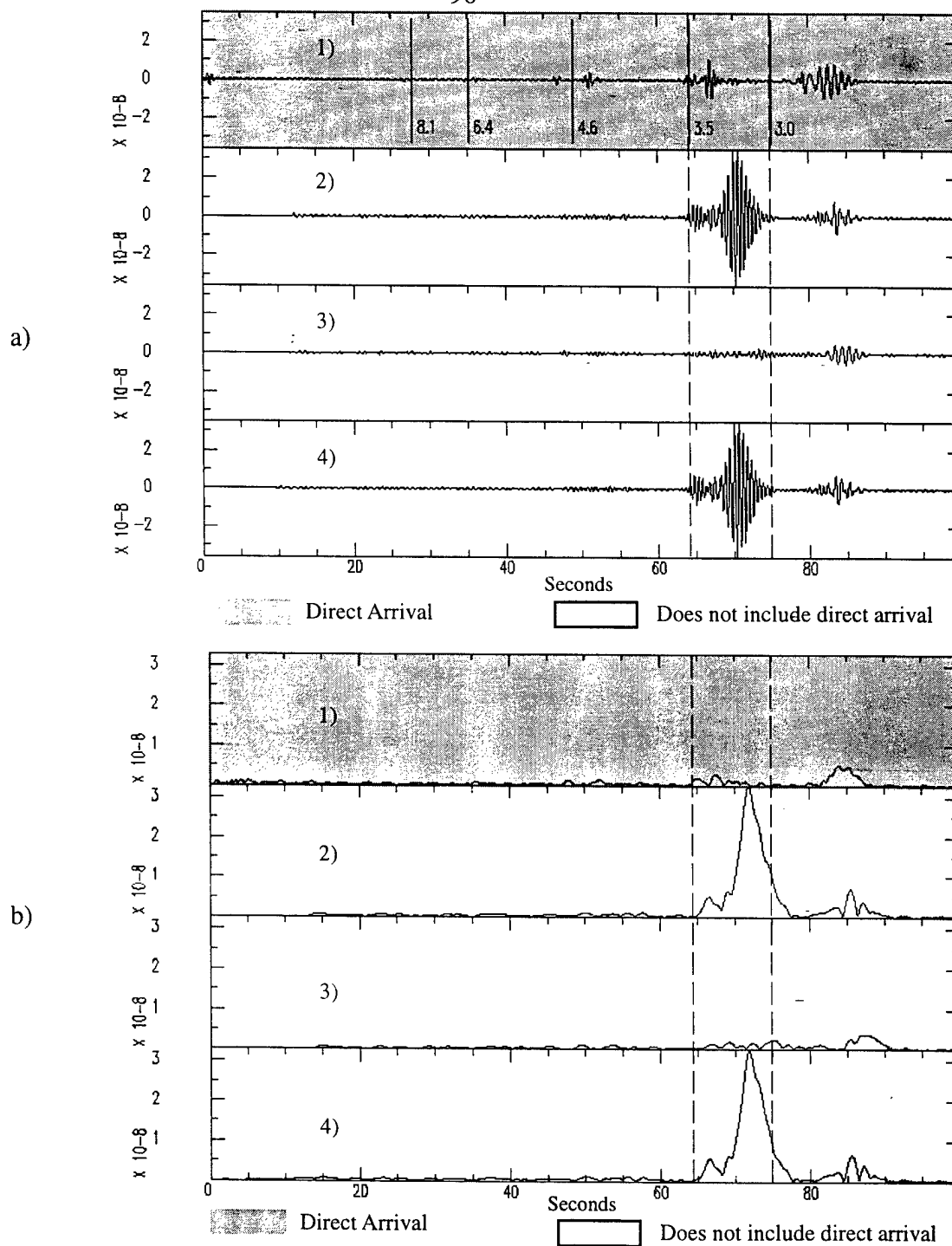
Figure 44: Radial component from explosion source. a) The 1) direct arrival, 2) direct arrival and all scattered components, 3) direct arrival and contribution from deep scattering, 4) direct arrival and contribution from shallow scattering. Note that the shallow scattering is significantly larger than the deep scattering. Shallow scattering effects dominate in the synthetic that is a sum of all contributions. b) A plot of the envelopes of the waveforms. Note that the envelope due to the shallow scatterers may add length and amplitude to the Lg coda.
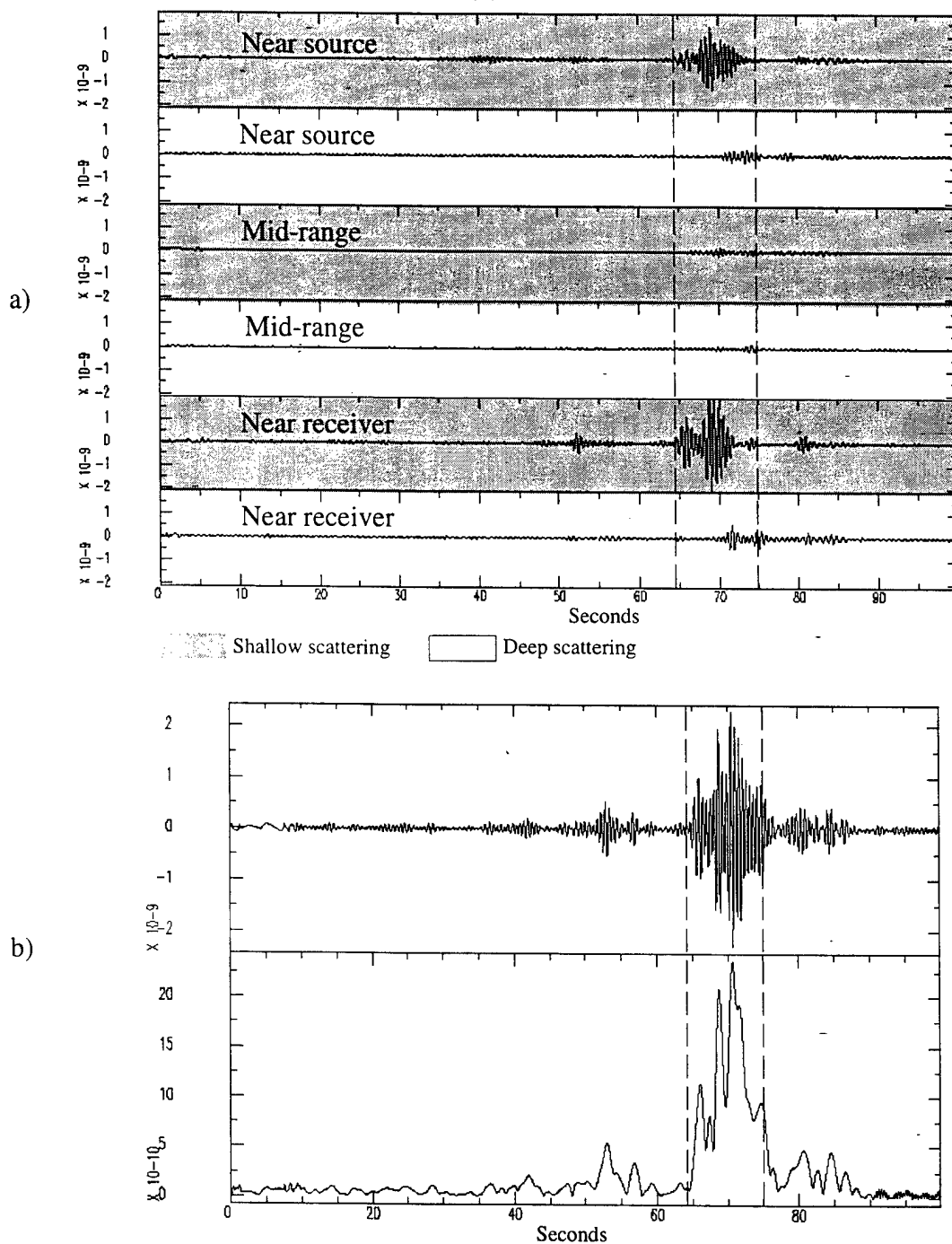
Figure 45: Transverse component of mode synthetics due to an explosion source. a) This illustrates range and depth effects on the scattered components (see figure 39 for location geometry). It is noted that shallow near source scattering and near receiver contributions dominate scattering effects and that mid-range scatterers are not seen much. b) Envelope of combined scattering contributions. Envelope shows emergence and decay typical of that observed in Lg.
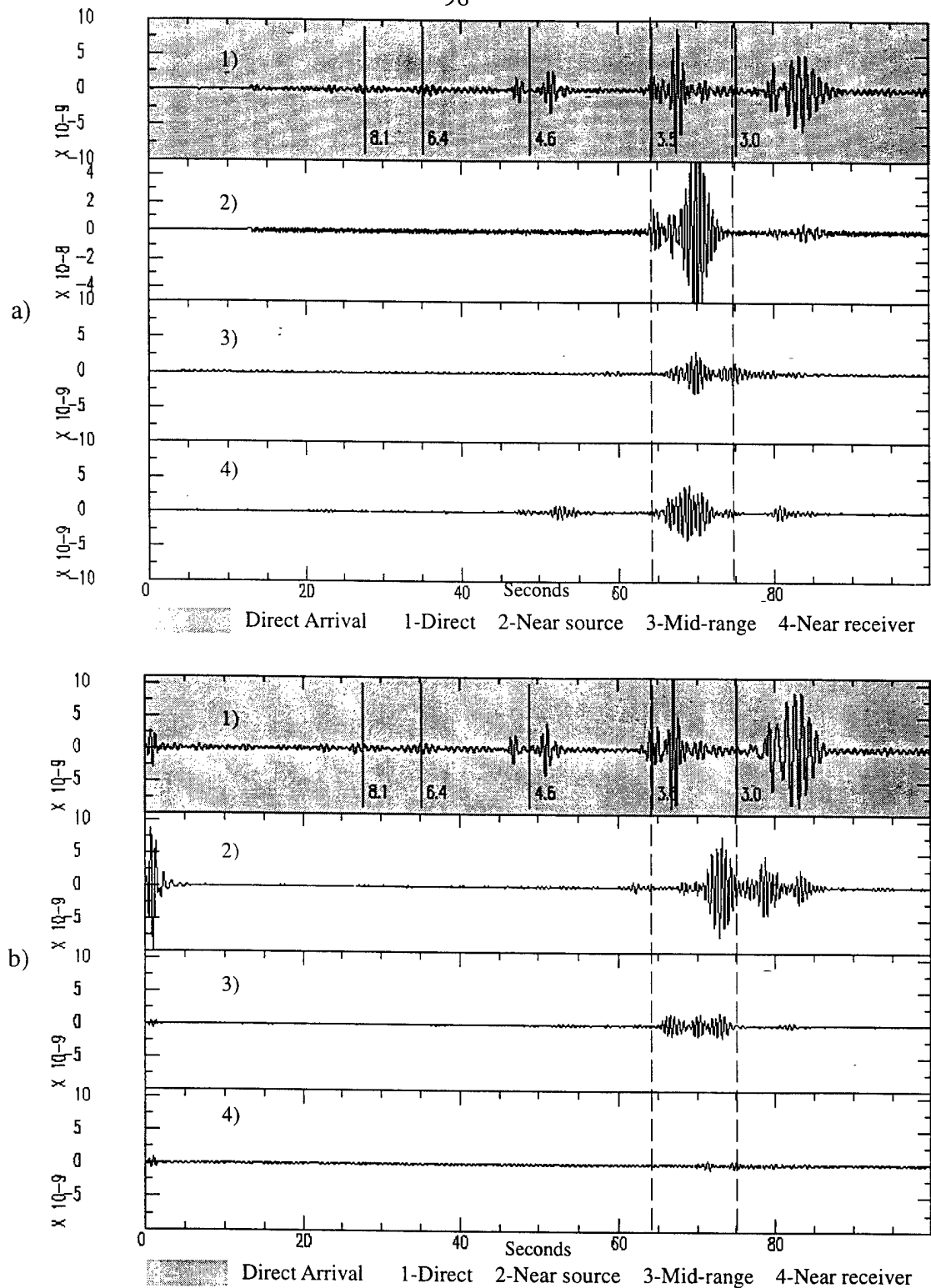
Figure 46: Vertical component of mode synthetics due to an explosion source. a) This illustrates range effects from shallow heterogeneities on the scattered components (see figure 39 for location geometry). b) Range effects due to deep heterogeneities. The shallow near source effects dominates by a factor of 10.
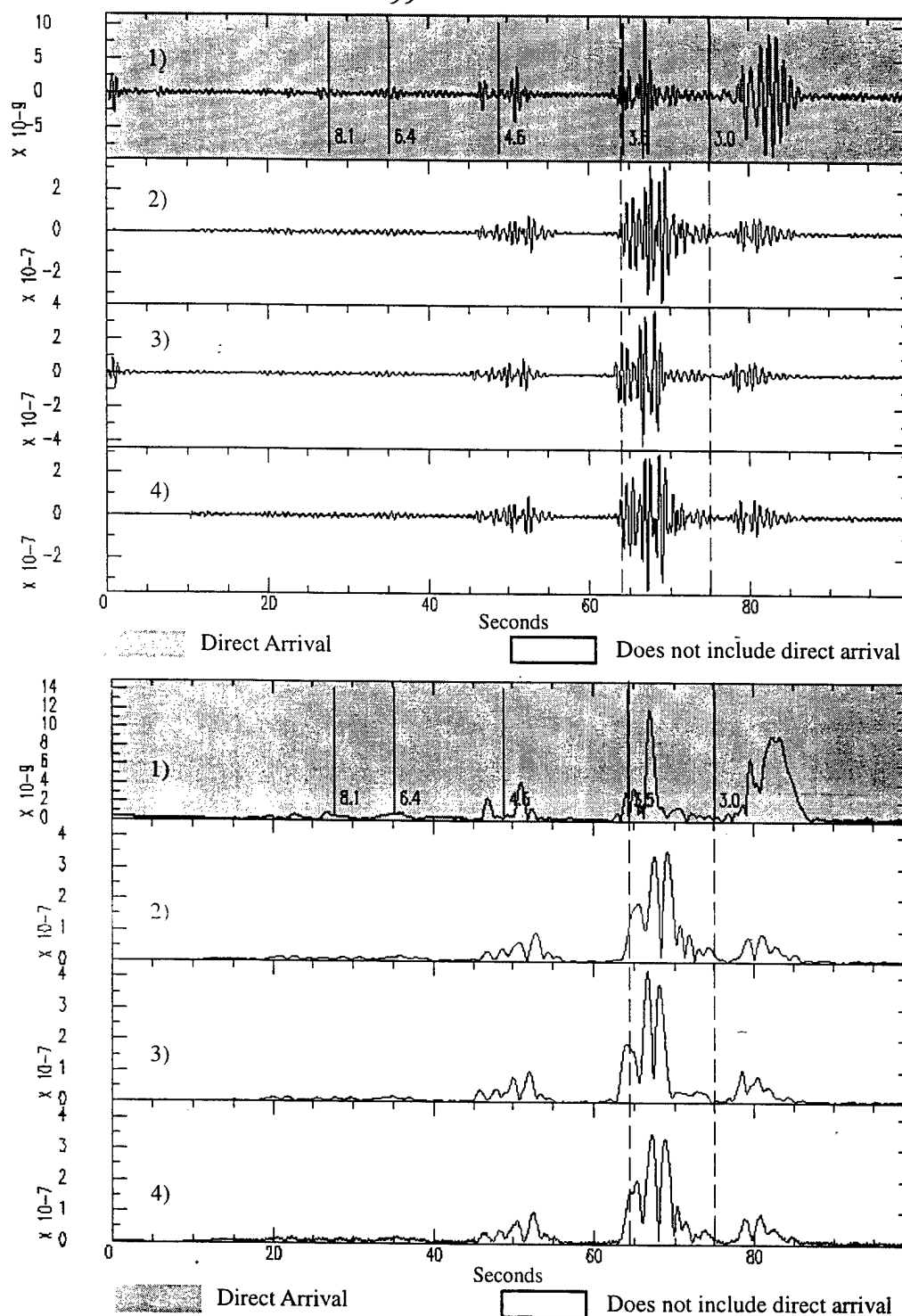
Figure 47: Vertical component synthetics from earthquake source. a) The 1) direct arrival, 2) direct arrival and all scattered components, 3) direct arrival and contribution from deep scattering, 4) direct arrival and contribution from shallow scattering. Note that the shallow scattering is of same order as the deep scattering, and most of the deep scattering is from near source effects. b) The envelopes of the synthetics are plotted to illustrate the lengthening of coda due to scattering from lateral heterogeneities. Shallow effects contribute most in lengthening the coda envelope.
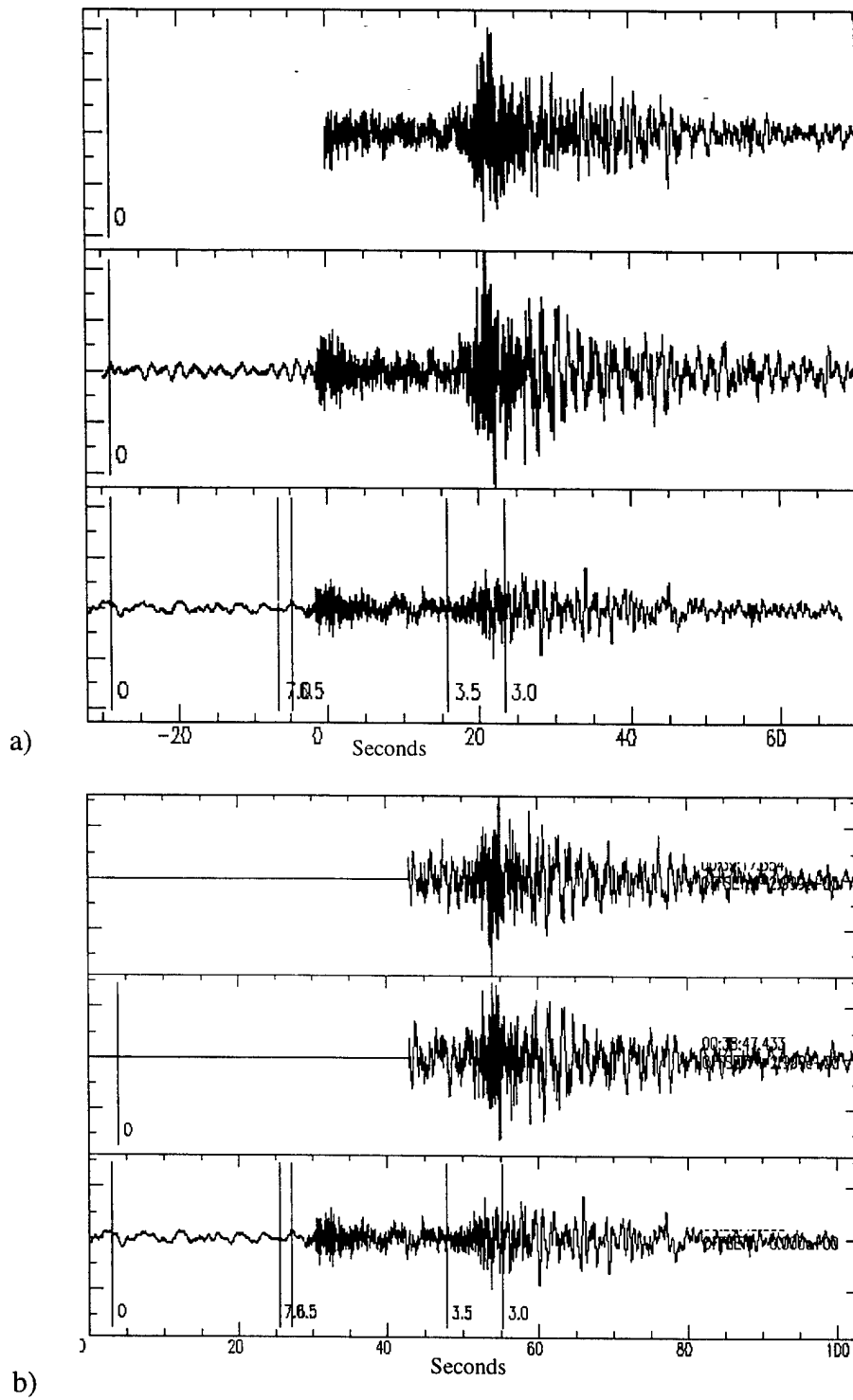
Figure 48: a) Raw data from of event on Sep 22, 1992 recorded at station KIV in the Caucasus network b) Horizontal components have been rotated to great circle path (radial and tranverse).
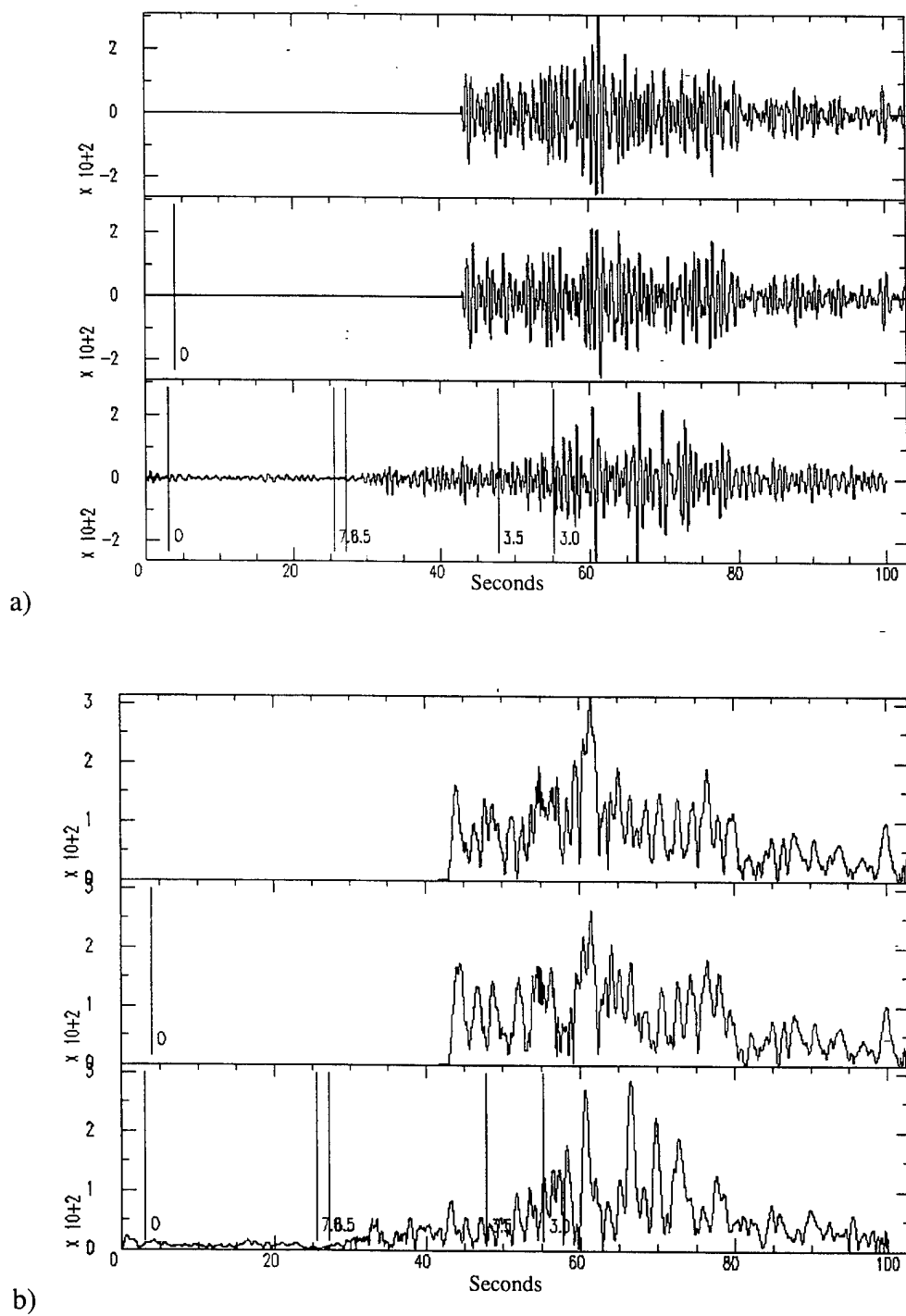
Figure 49: a) Rotated horizontal components and band passed 1-2 hz data from of event on Sep 22, 1992 recorded at station KIV in the Caucasus network. b) Envelope function taken of the rotated and filtered data.
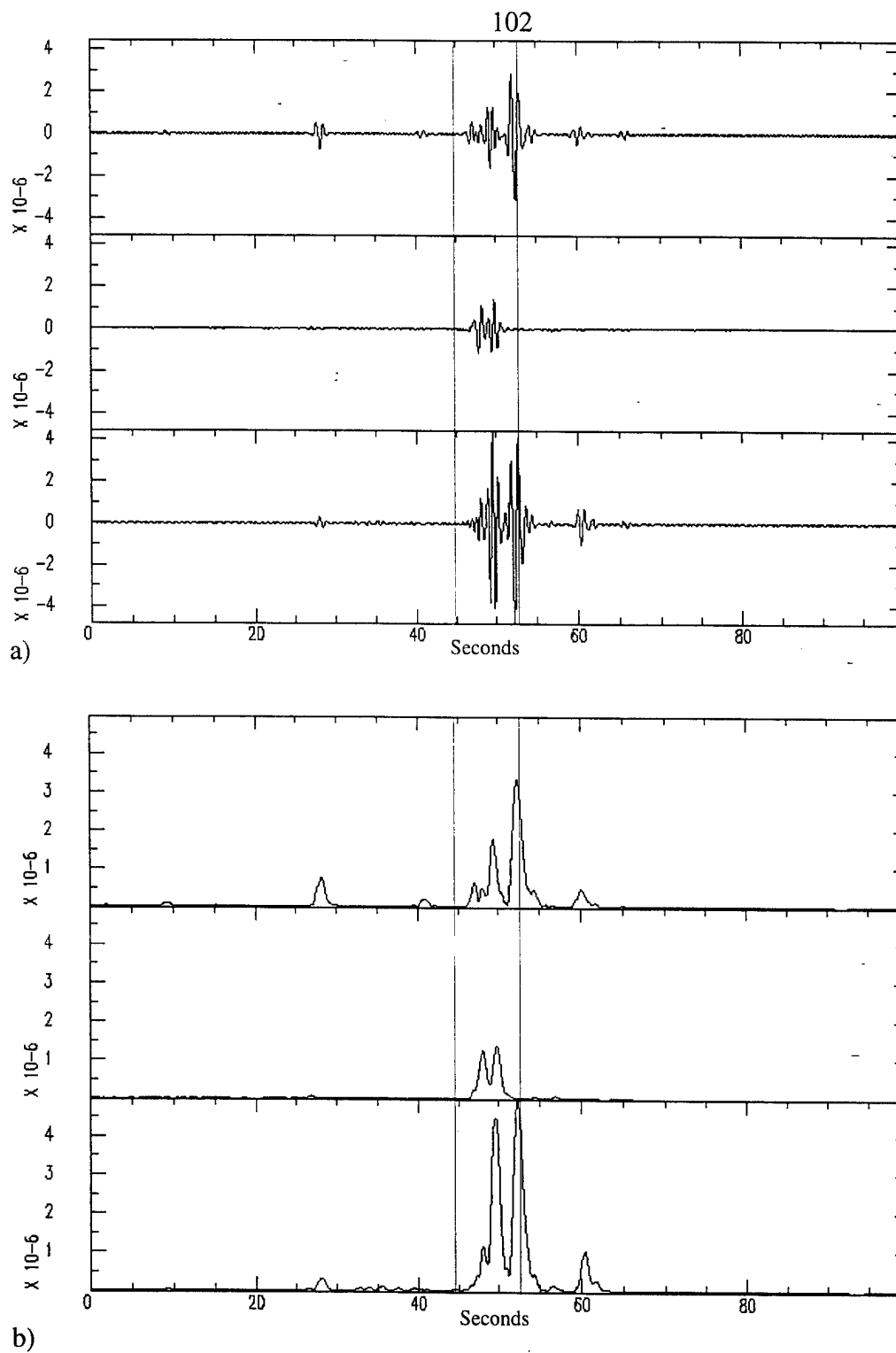
Figure 50: a) Synthetics for a direct arrival for the Caucasus event on September 22, 1992. Earthquake source at a depth of 5 km is used is used. b) Envelope function of the synthetics.
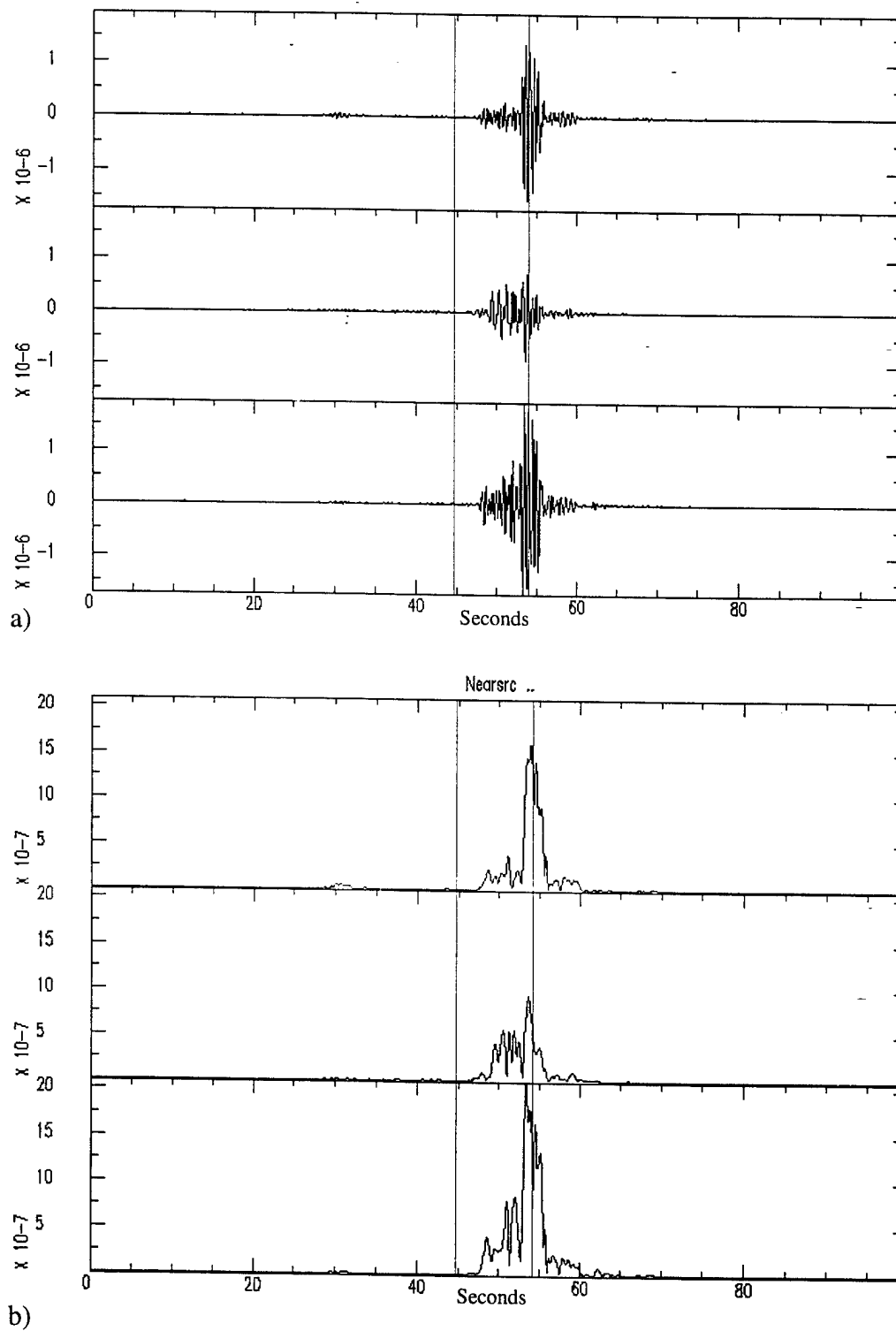
Figure 51: a) Mode syntheics due to a cluster of shallow scatterers near the source for Caucasus event on September 22,1992. b) Envelope function. Note that the peak in the late Lg arrival has been attenuated and more closely matches real data.
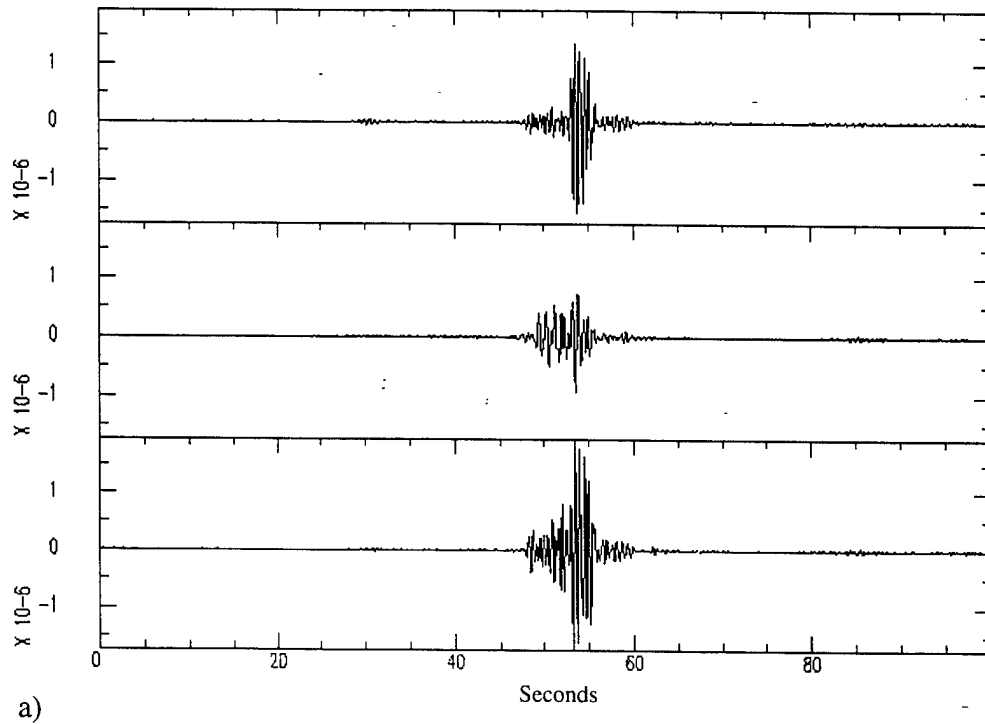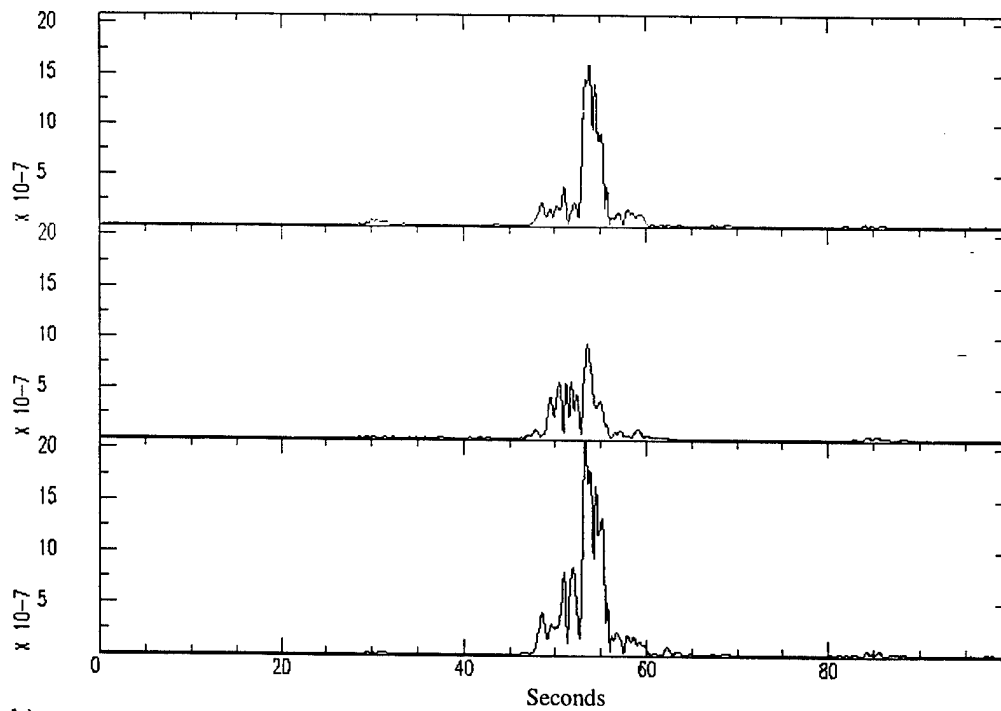
a)

b)

Figure 52: a) Mode syntheics due to cluster of shallow scatterers near the source and receiver for Caucasus event on September 22,1992. b) Envelope function. Note that the addition of more scattering (other than shallow source) does not noticebly alter the synthetics.
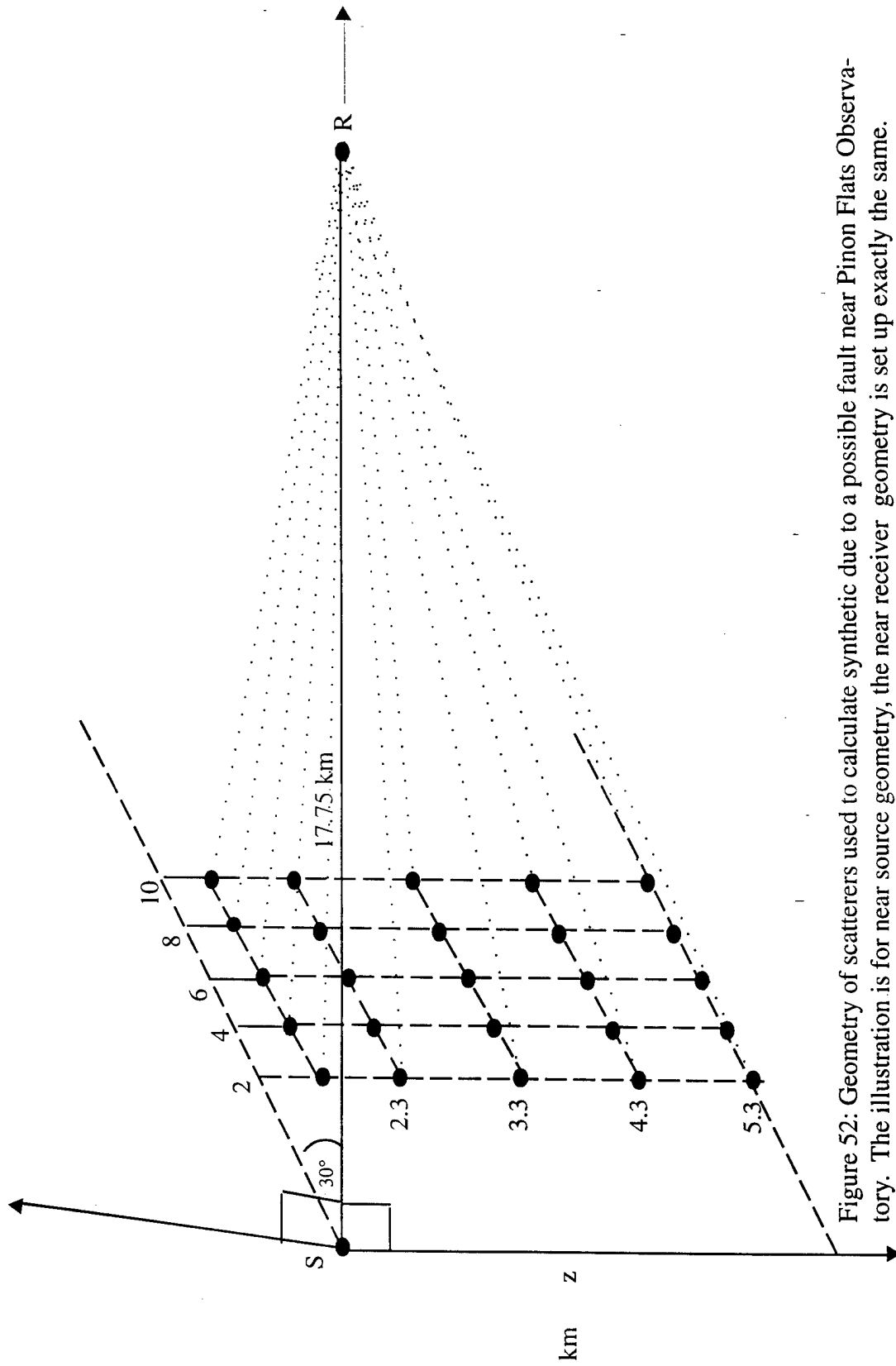
Figure 52: Geometry of scatterers used to calculate synthetic due to a possible fault near Pinon Flats Observatory. The illustration is for near source geometry, the near receiver geometry is set up exactly the same.
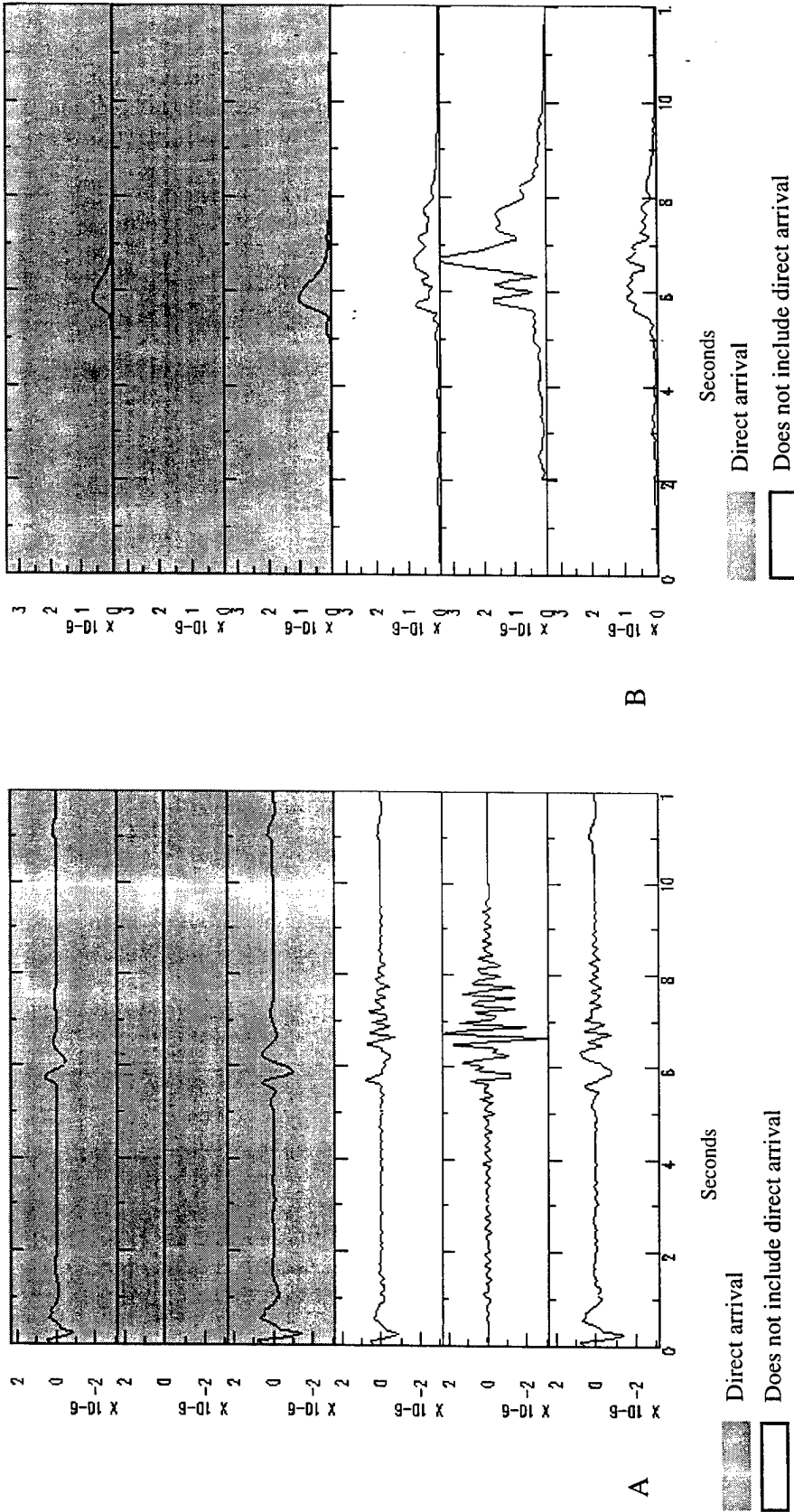
Figure 53: Synthetics computed for Pinon Flat Observatory to determine effect of near source fault structure on scattering. The volume is 0.2 km³ and variatons in lame's parameters is 3%. a) The direct wave is compared to the sum of the direct and scattered components. b) The envelope function is taken, illustrating the length and amplitude of coda that was generated. Note that large Lg is generated on the transverse component.

a) Pinon Flats Observatory high frequency seismic array layout.

b) Array used to calculate synthetics used in fk analysis.
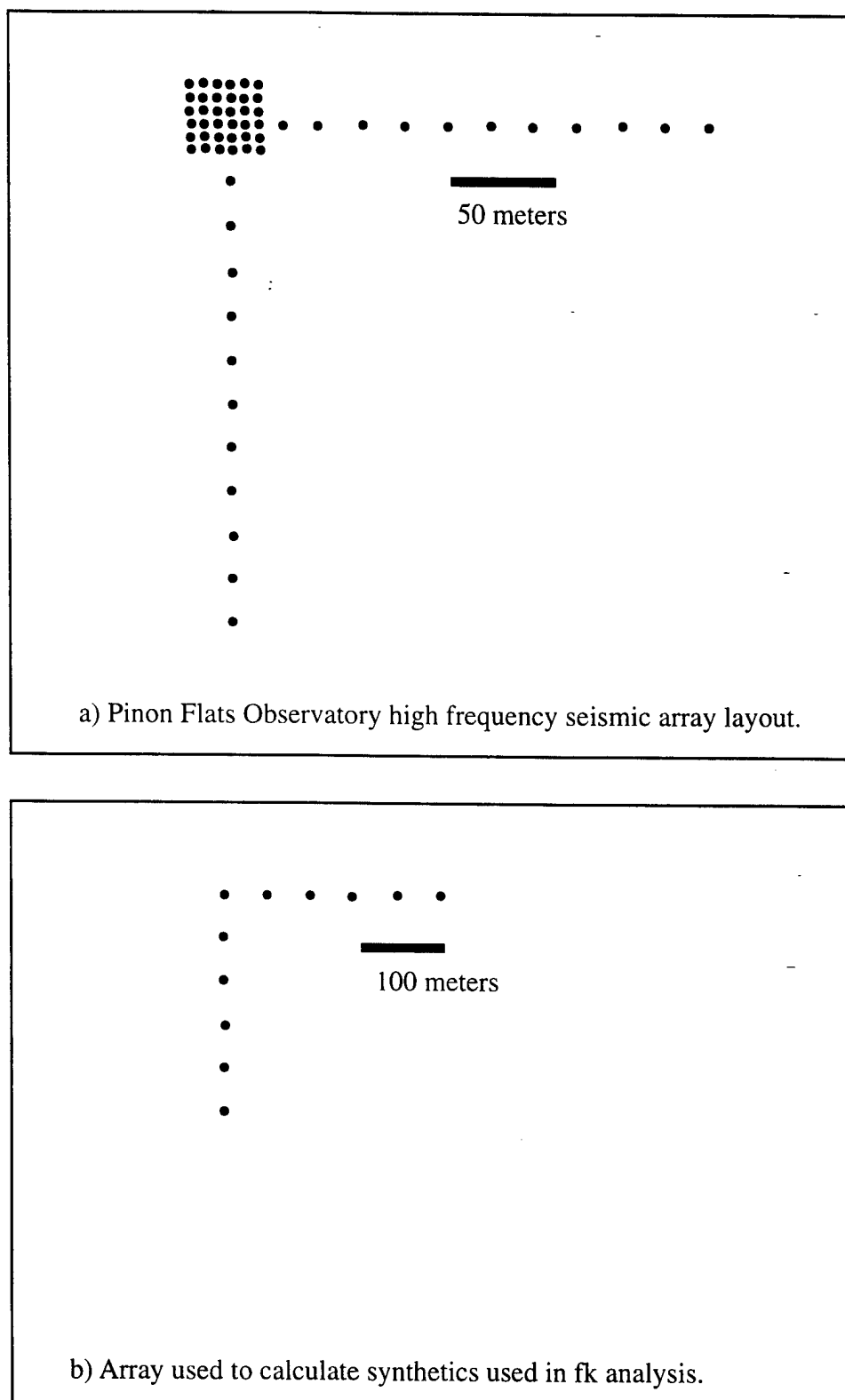
Figure 54: Array configurations used. a) Pinon Flats Observatory (PFO) broad-band array. b) Array used for in this study to compute synthetics for PFO.

Seconds
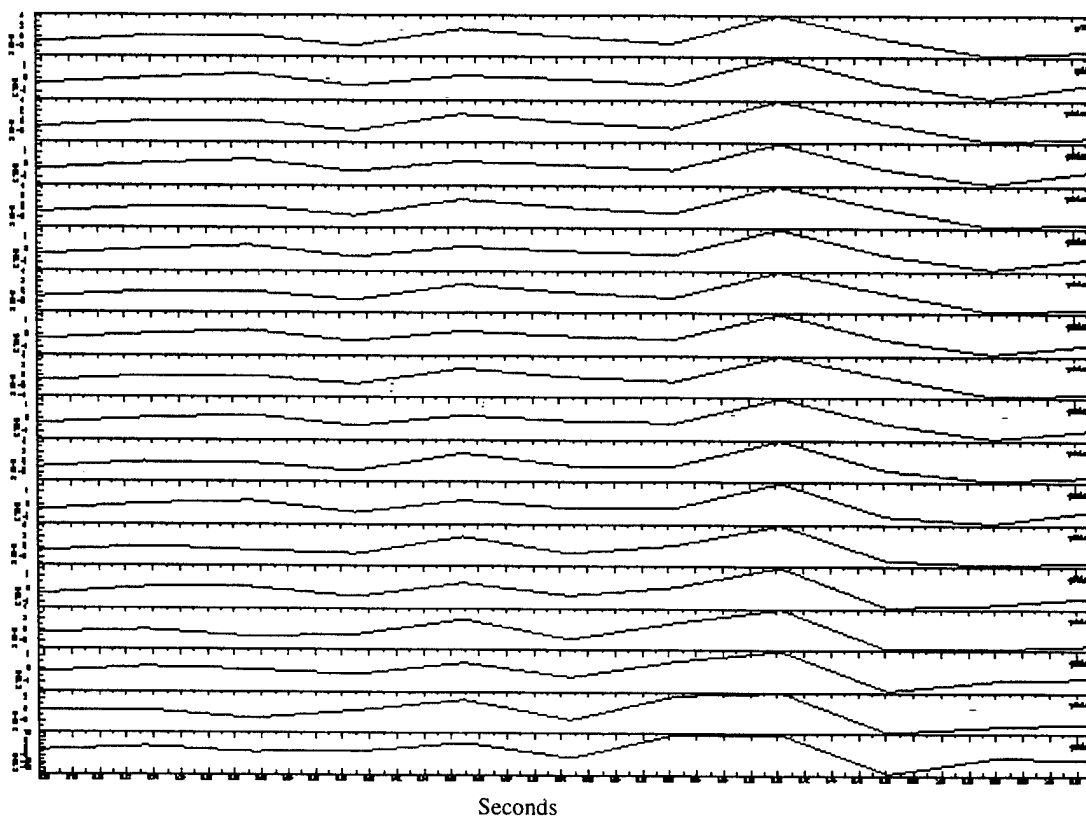
Broadband Wavenumber Spectrum

Maximum Radial Wavenumber:

Linear contour spacing

NORTH

EAST

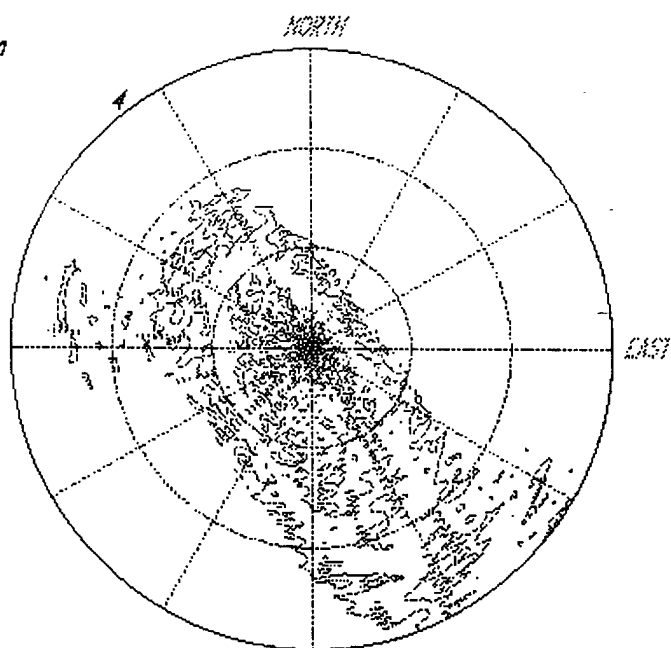Figure 55: a) Synthetics due to fault geometry, windowed around the Lg arrival for F-K analysis. b) F-K plot illustrating that energy is arriving off azimuth. (Source-receiver azimuth is 0°)

4 Conclusions and Recommendations

Ray modeling of Lg can be a useful reconnaissance tool for predicting the efficiency of Lg propagation in regions in which Moho and basin topography are known from deep seismic sounding and other geophysical observations or, at the minimum, constrained by known surficial geology. Both Moho topography and basin topography can be important in blocking all or a portion of the Lg coda, with basin topography primarily affecting shallow crustal sources. Predictions of Lg efficiency obtained from ray modeling are useful for design of array siting for maximum detection capability and for identifying problematic paths of propagation that will require customized regional discriminants.

The complexity of regional phases is strongly controlled by scattering by small scale structure close to the source and receiver, including the equalization of Lg energy on all components of motion, regardless of source type. It is not necessary to have detailed knowledge of small scale heterogeneity all along the paths of regional phases to be able to estimate such features as coda shape and duration, as long knowledge of heterogeneity statistics are known close to the source and receiver. Anisotropy of heterogeneity statistics can be important to include in regions having known trends of deformation.

Bibliography

Adamia, S., A. Chabukiani, M. Kakabadze, E., Koteshvili, M. Lordkipanidze, amd □D. Tabidze, Geological background of the Caucasus and adjacent area. In: S. Adamia and M. Kakabadze (Editors), Geological Events on Cretaceous-Paleogene Boundary, Int. Symp. Metsniereba, Tbilisi, pp. 18-51, 1991.

Aki, K., and B. Chouet, Origin of coda waves: source, attenuation, and scattering effects, *J. Geophys. Res.*, **80**, 3322-3342, 1975.

Aki, K., Scattering and attenuation of shear waves in the lithosphere, *J. Geophys. Res.*, **85**, 6496-6504, 1980.

Aki, K. and Richards, P. G., Quantitative Seismology, Freeman, San Fransisco,1981.

Bostock, M.G. and B.L.N. Kennett, The effect of 3-D structure on Lg propagation patterns, *Geophys. J. Intl.* **101**, 355-365, 1990.

Bratt, S. R. and T. C. Bache, Location estimation using regional array data, Science Applications International Corporatio Technical Report 87/1564, 55, AFGL-TR-00-0108, ADA 181161,1986.

Baumgardt, D. R., High frequency array studies of long range Lg propagation and the causes of Lg blockage and attenuation in the Eurasian continental craton, Final Report, PL-TR-91-2059(II), Phillips Laboratory, Hanscon AFB, MA, 1991.

Cerveny, V., and F. Hron, The ray series method and dynamic ray tracing systems for three-dimensional inhomogeneous media, *Bull. Seismol. Soc. Am.*, **70**, 47-77, 1980.

Cerveny, V., The application of ray tracing to the propagation of shear waves in complex media, in Seismic Exploration, edited by S.Treitel and K. Helbig, Geophysical Press, London, 1-124, 1985.

Chen, W. and P. Molnar, Focal depths of intracontinental and intraplate earthquake and their implications for the thermal and mechanical properties of the lithosphere, *J. Geophys. Res..*, **88**, 4183-4214, 1983.

Cormier, V. F., B. F. Mandal and D. Harvey, Incorporation of velocity gradients in the synthesis of complete seismograms by the locked mode method, *Bull. Seismol. Soc. Am.*, **81**, 897-930, 1991.

Fielding, E., B. L. Isacks, and M. Baragangi. A Network Accessible Geological and Geophysical Database for Eurasia, Proceedings of the 14th Annual PL/DARPA Seismic Research Symposium, September 1992, PL-TR-92-2210.

Frankel, A., A. McGarr, J. Bicknell, J. Mori, L. Seeber, and E. Cranswick, Attenuation of high-frequency shear waves in the crust: measurements from New York State, South Africa, and southern California, *J. Geophys. Res.*, **95**, 17441-17457, 1990.

Fuchs, K., and G. Muller, Computation of synthetic seismograms with the reflectivity
method and com☐parison with observations, *Geophys. J. R. Astr. Soc.*, **23**,☐417-
433,1971.

Gregersen S., Lg wave propagation and crustal structure differences near Denmark
and the North Sea, *Geophys. J. R. Soc.*, **79**, 217-234, 1984.

Gubernatis J. E., E. Domany, and J. A. Krumhansl, Formal aspects of the theory of the
scattering of ul☐tra☐sound by flaws in elastic materials, *J. Appl. Phys.*, **48**, 2804-
2811, 1977a.

Gubernatis J. E., Domany E., Krumhansl J. A. and Huberman, M., The Born
approximation in the theory of the scattering of elastic waves by flows, *J. Appl.
Phys.*, **48**, 2812-2819, 1977b

Gutenberg, B., Channel waves in the Earth's crust, *Geophysics*, **20**, 283-294, 1955.

Haddon, R. A. W., and J. R. Cleary, Evidence for scattering of seismic PKP waves near
the mantle-core boundary, *Phys. Earth and Planet.Int.*, **8**, 211-234, 1974.

Hamburger, M. W., W. A. Swanson II, and G. A. Popandopulo, Velocity structure and
seismicity of the Garm region, Central Asia, *Geophys J. Int.*, **115**, 497-511,
1993.

Harvey, D. J., Seismogram synthesis using normal mode superposition: the locked
mode approximation, *Geophys. J. Int.*, **66**, 37-69, 1981.

Iranian Long-Period Array Final Report, prepared for Albuquerque Seismological Center,
USGS, Contract No. 14-08-0001-14031, 8 April 1977, Texas Instruments Inc.

Joint Seismic Program Center, Kyrȝyz Network Information Product, Technical Reference
Manual: Triggered events from September 1,1991 to August 4, 1992, Version 1.0,
1993.

Joint Seismic Program Center, Caucasus Network Information Product: Triggered events
from January 1, 1992 to November 9, 1992, Technical Reference Manual, Version
1.0, 1994.

Kadinsky-Cade, K., M. Barazangi, J. Oliver, and B. Isacks, Lateral variations of high
frequency seismic wave propagation at regional distances across the Turkish and
Iranian Plateaus, *J. Geophys. Res.*, **86**, 9377-9369, 1981.

Kennett, B. L. N., Seismic Waves in laterally inhomogeneous media, *Geophys. J. R.
Astr. Soc.*, **27**, 301-325, 1972.

Kennett, B. L. N., Seismic Wave Propagation in Stratified Media, chapter 11, Cambridge
University Press, 1983.

Knopoff, L., F. Schwab, and E. Kausel, Interpretation of Lg, *Geophys. J. R. Astr. Soc.*,
33, 389-404, 1973.

Lukk, A. A. and V. I. Shevchenko, Character of the deformation of the earth's crust in the Garm region, Tadjikistan, from geological and seismic data, *Izv. Phy. Solid Earth*, **22**, 527-539, 1986.

Lukk, A. A. and V. I. Shevchenko, Seismic field patterns and rupture tectonics in the Garm region of Tadjikistan, *Izv. Phy. Solid Earth*, **26**, 1-12, 1990.

Mitchell, B. J., Anelastic structure and evolution of the continental crust and upper mantle from seismic surface wave attenuation, *Rev. Geophys.*, **33**, 441-462, 1995.

Molnar, P. and P. Tapponnier, Cenozoic Tectonics of Asia: Effects of a continental collision, *Science*, **189**, 419-426, 1975.

Molnar, P. and W. P. Chen, Focal depths and fault plane solutions of earthquakes under the Tibetaen Plateau, *J. Geophys. Res.*, **88**, 1180-1196, 1983.

Molnar, P., A review of geophysical constraints on the deep structure of the TibetanPlateau, The Himalaya and the Karokaum, and their tectonic implications, *Phil. Trans. R. Soc. Lond.*, **A326**, 33-88, 1988.

Oliver, J. and M. Ewing, Higher mode surface waves and their bearing on the structure of the Earth's mantle, *Bull. Seis. Soc. Am.*, **47**, 187-204, 1957.

Pulli, J., Attenuation of coda waves in New England, *Bull. Seism. Soc. Am.*, **74**, 1149-1166, 1984.

Ramos, E. G., Seismic expression of faults within and around the Peter the First Range, Master's Thesis, Indiana University, Bloomington, Indiana, 1992.

Randall, G. E., C. J. Ammon, and T. J. Owens, Moment-tensor estimation using regional seismograms from a Tibetan plateau portable network deployment, *Geophys. Res. Lett.*, **22**, 1665-1668, 1995.

Rogozhin, E. M., S. S. Aref'ev, B. M. Bogachkin, A. Sisternas, E. Phillip. Complex analysis of geological and seismological data and seismotectonic image of the source of Racha earthquake, *Fizika Zemly,*, **3**, 70-75, 1993.

Ruzaikin, A. I., I. L. Nersesov, V. I. Khalturin, and P. Molnar, Propagation of Lg and lateral variations in crustal structure in Asia, *J. Geophys. Res.*, **82**, 307-316, 1977.

Sato, H., Energy propagation including scattering effects, single isotropic scattering approximation, *J. Phys. Earth*, **25**, 27-41, 1977.

Scott, J. S., T. G. Masters, and F. L. Vernon, 3-D velocity structure of the San Jacinto fault zone near Anza, California-I, P waves, *Geophys. J. Int.*, **119**, 611-626, 1994.

Snieder, R, 3-D Linearized scattering of surface waves and a formalism for surface wave holography, *Geophys.J.R.Astr. Soc.*, **84**, 581-605, 1986.

Sweeney, J. J., Interpretation of crustal phase characteristics in Iran and the Surrounding Region determined from ILPA Data, *Seismological Research Letters*, **67**, No. 2, March/April 1996 Abstract.

Wagner, G. S. and C. A. Langston, A numerical investigation of scattering effects for teleseismic plane wave propagation in a heterogeneous layer over a half-space, *Geophys. J. Int.*, **110**, 486-500, 1992.

Wagner, G. S. Local wave propagation near the San Jacinto fault zone, southern California: Observations from a three-component seismic array, submitted *J. Geophys. Res.*, preprint, 1997.

Wallace, T., Body wave observations of tectonic release, in Explosion Seismology, Taylor, Patton, Richards, eds., *AGU Geophys. Mono.* , **65**, 161-170, 1992.

Wang, C and Herrmann, R. B., Synthesis of coda waves in layered medium, *PAGEOPH*, **128**, 7-42, 1988.

Wu, R. S., Seismic wave scattering and the small scale inhomogeneities in the lithosphere, PhD Thesis, Dept. of Earth, Atmos., and Planet.. Sci., Mass. Inst. of Tech., 1984.

Wu, R. S., and K. Aki, Scattering characteristics of elastic heterogeneity, *Geophysics*, **50**, 582-595, 1985.

Zhao, L. and D. V. Helmberger, Geophysical implication from relocation of Tibetan earthquakes - hot lithosphere, *Geophys. Res. Lett.*, **18**, 2205-2208, 1991.